Detection of Positrons from Breit-Wheeler Pair Formation

Dissertation

zur Erlangung des akademischen Grades

doctor rerum naturalium (Dr. rer. nat.)

seit 1558

vorgelegt dem Rat der Physikalisch-Astronomischen
Fakultät der Friedrich-Schiller-Universität Jena

von **Dominik Hollatz**, M. Sc.
geboren am 06.03.1991 in Berlin

Gutachter

1. Prof. Dr. Matt Zepf
   Institut für Optik und Quantenelektronik
   Friedrich-Schiller-Universität Jena

2. Prof. Dr. Jörg Schreiber
   Fakultät für Physik
   Ludwig-Maximilians-Universität München

3. Prof. Dr. Peter Norreys
   Department of Physics
   University of Oxford

Tag der Disputation: 09.12.2021

Zusammenfassung

Diese Arbeit beschäftigt sich mit der experimentellen Messung des Breit-Wheeler Prozesses, erstmalig beschrieben durch Gregory Breit und John A. Wheeler im Jahre 1934 [1], bei dem zwei Photonen kollidieren und ein Elektronen-Positronen Paar aus dem Quantenvakuum erzeugen. Die besondere Herausforderung hierbei ist der kleine Wirkungsquerschnitt von wenigen $10^{-29}\,\mathrm{m}^2$ oder 0.1 b und die gleichzeitige Notwendigkeit von Photonen mit vielen Megaelektronenvolt Energie. Solche Strahlen können von Teilchenbeschleunigern wie LCLS am SLAC oder European XFEL am DESY erzeugt werden. In der Vergangenheit wurden bereits Experimente zur Untersuchung von Photon-Photon Kollisionen an konventionellen Beschleunigern durchgeführt, wie beispielsweise E144 am SLAC 1997 [2], jedoch ist der von Breit und Wheeler beschriebene Zweiphotonenprozess bisher nicht beobachted worden. Während der letzten Jahrzehnte haben neuartige lasergetriebene plasmabasierte Teilchenbeschleuniger (LWFA) eine rasante Entwicklung durchgemacht [3, 4, 5, 6], was die Produktion der für den Breit-Wheeler Prozess notwendigen Photonenstrahlen an reinen Laseranlagen möglich macht [7, 8, 9].

Die vorliegende Arbeit beschäftigt sich mit den Herausforderungen solcher Experimente speziell an Hochintensitätslasern am Beispiel von Astra Gemini, einem viele 100 TW starken Zweistrahlsystem an der CLF in England. In einem Experiment wurden viele 100 MeV starke γ-photonen von LWFA Elektronenbremsstrahlung mit 1 bis 2 keV starken Röntgenphotonen aus Germanium M-L-Schalenübergangsstrahlung kollidiert um Paare durch den Breit-Wheeler Prozess zu erzeugen. Zur Messung dieser Paare wurde im Rahmen der vorliegenden Arbeit ein Detektionssystem bestehend aus einer magnetischen Strahlführung und strahlengeschirmten Einzelteilchendetektoren entwickelt und getestet. Die aufgenommen Messdaten erlauben eine Abschätzung der Anforderungen an zukünftige Experimente zur erstmaligen Messung des zweiphotonen Breit-Wheeler Prozesses.

Abstract

This work explores the experimental observation of the Breit-Wheeler process, first described by Gregory Breit and John A. Wheeler in 1934 [1], where two photons collide to form an electron positron pair from the quantum vacuum. The specific challenge thereby is the low cross section of a few $10^{-29}\,\mathrm{m}^2$ or 0.1 b combined with the requirement of photon energies in the range of mega electronvolt. Such beams can be provided by particle accelerators, for instance LCLS at SLAC or the European XFEL at DESY. Experiments exploring photon photon collisions with conventional accelerators were done in the past, for example E144 at SLAC in 1997 [2], however the two photon process described by Breit and Wheeler has not yet been observed. Over the last few decades, novel laser driven plasma based particle accelerators (LWFA) made significant progress [3, 4, 5, 6], allowing the production of the required photon beams to study the Breit-Wheeler process at pure laser facilities [7, 8, 9].

The work in hand explores the challenges related to such an experiment specifically at high power laser facilities using the example of Astra Gemini, a multi 100 TW dual beam system at the CLF in England. In an experiment, multi 100 MeV γ-rays from LWFA electron bremsstrahlung and 1-2 keV x-rays from Germanium M-L shell transition radiation are collided to produce pairs through the Breit-Wheeler process. A detection system to measure those pairs composed of a permanent magnet beam line and shielded single particle detectors is developed and tested within this thesis. The acquired data allows an estimate of the requirements for future experiments to measure the two-photon Breit-Wheeler process.

Contents

1. Introduction

A Historical Path towards Modern Physics

Physics as a science is historically based on observing nature and subsequently formulating mathematical models to describe the laws that our world is built upon. As a pioneer, Sir Isaac Newton published *Philosophiæ Naturalis Principia Mathematica* [10] in 1687 and described what is referred to as Newtonian or classical mechanics, after having an apple fallen onto his head, so the narrative. Setting the next milestone in 1861, James Clerk Maxwell published *On Physical Lines of Force* [11]. The core of his work can be summarised in a set of four partial differential equations, known as Maxwell's Equations, that form the foundation of *classical electrodynamics*. Together with Newtons theory, dynamic systems of electrically charged objects interacting via the electromagnetic force and thereby light could be described. However, only 26 years later, Hertz observed the photoelectric effect in 1887 [12, 13], where he discovered that ultraviolet light had an effect on the electric charge emitted from a conducting surface, what should be explainable with Maxwell's theory. The photoelectric effect was studied further during the next few years and lead to the discovery of the first subatomic particle by Thomson in 1897 [14], the *electron*.

Five years after that, also studying the photoelectric effect, Lenard observed in 1902 [15] that the energy of the emitted electrons correlated to the frequency of the incident light. This was contradictory to Maxwell's theory of electromagnetism that describes light as a continuous electromagnetic wave, which predicted a linear dependency of electron energy to light intensity, but not frequency. Only three years later in 1905, this inconsistency was explained by Albert Einstein in *Über einen die Erzeugung und Verwandlung des Lichtes betreffenden heuristischen Gesichtspunkt* [16] after studying Max Plancks *Ueber das Gesetz der Energieverteilung im Normalspectrum* [17]. He proposed that light is composed of particles, called quanta or photons, similar to electric charge being composed of electrons. Today, this work is seen as a key step towards a completely new field of physics named after the particle of light: Quantum Physics.

Electrons, Positrons and the Breit-Wheeler Process

Quantum physics was radically different from the classical disciplines in physics and evolved rapidly in the early 20th century. In 1928, Paul Dirac published *The Quantum Theory of the Electron* [18], where he introduced the Dirac equation and discussed the negative energy solution for the electron. The concept of negative energy was an issue because a free electron could emit photons and consequently fall to lower energy levels all the way to negative infinity. Refining his work in 1929 [19], he solved this issue by interpreting vacuum as completely filled with negative energy electrons, the so called Dirac sea, so that a positive energy electron would not be able to transition to negative energy states due to Pauli's exclusion principle [20]. Finally, with input from Robert Oppenheimer, Dirac published *Quantised singularities in the electromagnetic field* [21] in 1931 where he predicted the existence of a new particle, the anti-electron, today known as positron. It can be interpreted as a missing electron or a hole in the otherwise filled Dirac sea and if a positive energy electron comes sufficiently close to it, there is a chance that they recombine. Both electron and positron are annihilated in this process and the base state of vacuum, the flat Dirac sea, is restored with the energy and impulse being carried away by two photons. One year later in 1934, Gregory Breit and John A. Wheeler [1] explored the inverse of Dirac's electron positron annihilation, which is the collision of two photons to raise an electron from a negative to a positive state and thereby creating a real electron and a hole in the Dirac sea, which is interpreted as a real positron. This process is named after Breit and Wheeler. The existence of the positron as a real particle was proven by Anderson a year earlier in 1933 [22] via Bethe-Heitler [23] pair production, a process related to Breit-Wheeler pair production where a free high energy photon interacts with photons from the electric field around atomic nuclei to form an electron positron pair from quantum vacuum. This experiment was possible due to the large number of atomic nuclei in solid state matter in the order of $10^{22}\,\mathrm{cm}^{-3}$ and enabled the production of positrons within a few millimetres and subsequent annihilation with electrons. A similar experiment to observe the Breit-Wheeler process would require a photon density comparable to solid state matter, which was impossible to produce in the year 1934. Breit and Wheeler were aware of the staggering requirements for an experimental observation and they commented this in their publication with the following words: „It is also hopeless to try to observe the pair formation in laboratory experiments with two beams of x-rays or γ-rays meeting each other on account of the smallness of σ and the insufficiently large available densities of quanta.“ [1]

Technical Advance in Particle Accelerators

Along the rapid advancement in theoretical physics, a novel piece of technology induced a similar progress in experimental physics, the particle accelerator. Starting with the pioneering work of Cockroft and Walton in 1930 [24], this machine was able to accelerate particles with electric potential differences up to 300 kV. Driven by the ever-growing energy requirement to access novel reactions, accelerating fields quickly approached technological limitations set by field ionisation of conducting surfaces [25]. To further increase the energy of particles, accelerators became massive in size culminating in the LEP and LHC at CERN with a 27 km circumference, which enabled electron and positron energies of 104.5 GeV [26] (collision energy 209 GeV) and proton energies of 6.5 TeV [27] (collision energy 13 TeV).

Related to Breit-Wheeler pair formation, one accelerator facility stands out, the Stanford Linear Accelerator Center, today SLAC National Accelerator Laboratory. On the experimental campaign E144 in 1997, the 46.6 GeV electron beam was collided with a high intensity laser at $I = 1.3 \cdot 10^{18}\,\mathrm{W/cm^2}$. The electrons scattered and emitted γ-rays at several GeV of energy, which subsequently reacted with the laser field to form electron positron pairs via the non-linear Breit-Wheeler process. This was the first observation of inelastic light-by-light scattering [2]. The specification non-linear in combination with the Breit-Wheeler effect denotes a specialised case, where the reaction of two photons is not possible due to low photon energies. Instead, the process relies on a high photon density so that more than two photons can participate in the reaction. To distinguish between the variants, Breit and Wheelers inverse Dirac annihilation is sometimes referred to as two-photon or linear Breit-Wheeler process and the strong field case is called multi-photon or non-linear Breit-Wheeler process, but throughout this work the term Breit-Wheeler process will be used for Breit and Wheelers inverse Dirac annihilation if not otherwise specified.

On E144, the scattering laser had a photon energy of 2.35 eV, which would require a 111 GeV photon to enable pair production, whereas the maximum achievable photon energy on this experiment was 29.2 GeV. Data analysis exhibited that around 5 laser photons participated in each reaction on average. Although E144 demonstrated light-by-light scattering induced pair production from quantum vacuum, the Breit-Wheeler process is still to be observed.

Photon Collision at High Power Lasers

E144 was possible due to the progress in high power laser technology and future experiments would require such a system to some extent, so that the experimental investigation of the Breit-Wheeler process was linked to high power lasers, however, a particle accelerator was still required to provide the high photon energies. This changed with the rapid development of laser wake field accelerators (LWFA), especially with a breakthrough in 2004 [3, 4, 5], dubbed the dream beam, where highly relativistic electron beams with quasi mono energetic spectra up to 100 MeV were accelerated. Two years after that in 2006, the GeV barrier was surpassed [28] and by the present day, LWFA electron beam energies up to 8 GeV [6] are demonstrated. The availability of high electric fields and now also high particle energies at high power laser facilities led to the conception of a new class of experiments to study photon photon collision with all optical setups around 2010, especially the non-linear Breit-Wheeler process [7, 9] at Astra Gemini. The idea was to collide GeV class γ-ray photons from bremsstrahlung of the LWFA electron beam with a $10^{22}\,\mathrm{W/cm^2}$ strong optical laser to achieve measurable pair rates above one per shot.

For an observation of the linear Breit-Wheeler process, a second source of high energy photons is required. In 2014, O.J. Pike [8] proposed such an experiment where a γ-ray beam is produced by LWFA electron bremsstrahlung and subsequently send through a thermal x-ray bath at 100 to 400 eV produced inside a laser heated solid state target, called hohlraum. This setup would enable the two photon Breit-Wheeler process and generate pair rates between 10^2 and 10^4 per laser shot, however it requires the megajoule class laser [29] at NIF, which is usually reserved for different types of experiments, not to mention the absence of a GeV class LWFA source. Over the following years, the conception of a novel x-ray source based on Germanium M-L shell transition radiation between 1-2 keV allowed the generation of sufficiently hard and intense x-rays for the linear Breit-Wheeler process with lasers in the 10 J range, which made an experiment at Astra Gemini possible.

Structure of this Thesis

The work in hand presents an experimental campaign performed at Astra Gemini to measure the linear Breit-Wheeler process by colliding a high energy γ-ray beam with a high intensity x-ray field. A special challenge thereby is the detection of the produced pairs while suppressing background radiation to increase the signal-to-noise ratio. To approach this, a system of permanent magnets that guides pairs to shielded single particle detectors is developed. The magnet system is validated and the detectors are calibrated and tested for sensitivity. Data with full Breit-Wheeler setup is taken and the results are analysed. Based on that, requirements for future experiments are evaluated. The thesis is structured in multiple chapters as follows:

- **Chapter 2** presents theoretical considerations related to the experiment. This is done by introducing the Breit-Wheeler process as well as estimating the expected pair rate on this experiment. Further are statistical boundary conditions for a successful measurement explored and the implications of shot-to-shot fluctuations and the stochasticity of single particle signals are discussed.

- **Chapter 3** presents the experimental setup. This includes a description of the overall setup and diagnostics at Astra Gemini to provide the two photon sources for the Breit-Wheeler process. The pair detection system composed of a magnetic beam line and single particle detectors developed within this work is presented in greater detail with a focus on the evaluation and calibration of the detector signal.

- **Chapter 4** presents the results obtained on the campaign. This includes a characterisation of the radiation background as well as a validation of the overall setup including the detection system with an artificial pair source. Data from collision shots is compared to background shots in a statistical analysis and the results are discussed with respect to the achieved significance along with potential sources of errors.

- **Chapter 5** provides a conclusion of the whole experiment. This is done by summarising the setup performance and obtained results. The final section discusses improvements for future experiments.

2. Theory

This chapter will explore some theoretical aspects related to the experimental observation of the Breit-Wheeler effect and is composed of two major parts. In the first part, the Breit-Wheeler process is introduced with a qualitative explanation of quantum electrodynamics and discussions of several pair production mechanisms. This is followed by a quantitative description of the two-photon Breit-Wheeler cross section, the probability of pair formation and a calculation of the expected pair yield with the specific experimental setup presented on this thesis.

The second major part presents statistical aspects related to the experimental detection of the Breit-Wheeler process. Therefore, sources of statistical uncertainties are discussed and the calculation of error margins and confidence values is presented for shot-to-shot fluctuations, which is essential for high power laser experiments, and for Poisson distributed quantities, which describe single particle signals like the Breit-Wheeler pairs.

2.1. Pair Production from Quantum Vacuum

The process of electron positron pair formation as the result of a collision of two photons was described by Breit and Wheeler as the inverse of Dirac's electron positron annihilation [1] and is theoretically described with the methods of *quantum electrodynamics* (QED).

QED describes, broadly speaking, the interactions of charged particles via the electromagnetic force and was developed from around 1927 [30] onwards. Before that, quantum mechanical phenomena were described with Schrödinger's equation [31], which is nonrelativistic and not well suited to describe processes where particles are produced or annihilated, for example the emission or absorption of photons connected to transitions of electrons between different energy states in atomic shells. To describe processes with changing photon numbers or, broadly speaking, any quantum mechanical process where a finite number of photons participate, the description of the electromagnetic field was modified through a process called quantization. A key

step towards this was made by Planck many years before that in 1901 [17], where he proposed that the radiation field inside a perfectly absorbing cavity is composed of many harmonic oscillators. His revolutionary idea was that the energy of each oscillator can not be arbitrary values but must be a positive multiple of $\hbar\omega$, where ω is the angular frequency and $\hbar$ is the reduced Planck constant. Four years later in 1905 Einstein pursued this idea and proposed the composition of any electromagnetic wave as a collection of particles with energy $\hbar\omega$, called quanta, to explain the photoelectric effect [16]. This sparked a decades long discussion whether light is composed of particles or is better described as electromagnetic fields, which causes confusion among physics students even to this day. It was Dirac who proposed a combined description of both properties by treating electromagnetic waves as fields, which do only interact with charged particles via quantized excitations of this field [32]. Any interaction of the electromagnetic field with charged particles is therefore linked to a change of the number of photons in certain energy levels, which enables an elegant description of quantum mechanical processes involving single photons and changing photon numbers. This quantisation of the electromagnetic force is one key aspect of QED.

2.1.1. Dirac's Theory of the Electron

The second major issue with Schrödinger's equation is that it is not Lorentz invariant, which means it does not satisfy the laws of Einstein's special relativity. An attempt to construct a Lorentz invariant and therefore relativistic quantum theory was made by Klein in 1926 [33], today known as Klein-Gordon equation. However, this theory does only describe scalar fields associated with spinless particles whereas electrons have a spin of $\frac{1}{2}$. This was solved by Dirac in 1928 [18], who developed a relativistic quantum theory of the electron. His work is seen as one of the most significant achievements in physics of the 20th century [32] and is the second major ingredient for QED. The Dirac equation incorporates the spin-$\frac{1}{2}$ property of the electron naturally and provides 4 solutions with positive and negative energy as well as spin up and spin down. The negative energy solution for the electron and by extension the existence of negative energy levels at all was problematic for the description of various systems, for example the hydrogen atom, because there is no stable ground state. The electron would have a finite probability of transitioning to negative energy levels, a process that can go on indefinitely, releasing an endless amount of energy. Dirac approached this by proposing that all negative energy states as naturally filled with electrons [19], which prevents an electron from descending to negative levels due to Pauli's exclusion principle [20]. This

interpretation of vacuum is called the Dirac sea. The possible energy values for free electrons in the Dirac sea for both positive and negative regions are continuous and not discrete, but due to the finite rest mass m_e of the electron the absolute value must be greater or equal to its rest mass energy $|E| \geq m_e c^2$ so that the Dirac sea is only filled up to $-m_e c^2$. Likewise start positive energy levels at $+m_e c^2$. The composition of vacuum as a collection of negative energy states entails a finite probability for electrons to transition to positive energy states if the required energy difference of $\geq 2m_e c^2$ is provided to overcome the potential barrier. The electron would become a real observable particle, leaving a hole in the Dirac sea that appears as a missing electron with a charge opposite to the electron, interpreted as a real positron. Whenever such a hole or positron reaches the vicinity of an electron, there is a finite probability for the electron to transition into the negative energy state defined by the positron, releasing the energy difference in form of photons. This recombination process of electron and positron to restore the base state of vacuum is called Dirac annihilation. The inverse of this, the excitation of pure vacuum to create a real electron positron pair, is called Breit-Wheeler process. Dirac's theory of the vacuum and the existence of an antiparticle to the electron, as important as it is for modern quantum physics, was in fact not taken seriously until the experimental observation of the positron by Anderson in 1932 [22, 32, 34].

2.1.2. Sauter-Schwinger Pair Production

The description of vacuum as an endless amount of negative energy electrons has another important implication if Heisenberg's uncertainty principle [35] is taken into account. It states that the product of the measured position and momentum of a quantum object, for example excitations of the electromagnetic field, is always larger or equal to half of the reduced Planck constant. In other words, if sufficiently small spatial domains of the quantum vacuum are considered, the uncertainty of photon and electron momenta and by extension energy will surpass the pair creation threshold of $2m_e c^2$, causing spontaneous transitions of electrons from negative into positive energy levels. However, these *vacuum fluctuations* occur on spatial dimensions of the reduced Compton wavelength of the electron $\lambda\!\!\!^{-}_C = \frac{\hbar}{m_e c} \approx 3.9 \cdot 10^{-13}$ m and on time scales of the Compton time $\frac{\lambda\!\!\!^{-}_C}{c} \approx 1.3 \cdot 10^{-21}$ s and are composed of virtual particles. Since the formed electron and positron possess opposite charge, one could think of an electric field to separate them, turning the virtual pair into real measurable particles. Such an electric field would need to be sufficiently strong to provide the

rest mass energy of the pair of $m_e c^2$ per particle over the spatial dimension of the pair separation, which is the Compton wavelength $\lambda\!\!\!^{-}_C$. This has been investigated by Sauter in 1931 [36] and the explicit pair production rates where calculated by Schwinger in 1951 [37], which is why this critical electric field of QED is called the *Sauter-Schwinger field* $E_S = \frac{m_e c^2}{e\lambda\!\!\!^{-}_C} \approx 1.3 \cdot 10^{18}$ V/m. It corresponds to a laser intensity of $I_S \approx 2.3 \cdot 10^{29}$ W/cm^2 or a *normalised vector potential* of $a_0 \approx 3.3 \cdot 10^5$. Pair production via this Sauter-Schwinger mechanism is described in a static electric field E with the Schwinger formula, which scales with $\propto E^2 \exp\left(-\pi \frac{E_S}{E}\right)$ and is therefore strongly suppressed if $E < E_S$. The Sauter-Schwinger field is out of reach for up to date and near future experimental facilities in the laboratory frame of reference, which makes a direct measurement of Sauter-Schwinger pair production practically impossible. However, pair production from quantum vacuum is experimentally achievable via the Breit-Wheeler mechanism.

2.1.3. Linear Breit-Wheeler Pair Production

From Dirac's vacuum model with a $2m_e c^2$ energy barrier between allowed positive and negative electron states it is immediately clear that the requirement for pair production is a very large photon energy of $\geq$1022 keV. In the presence of another massive and electrically charged particle that contributes to the energy momentum conservation, for example an atomic nucleus, a single photon is able create a pair given that it carries the required amount of energy. This special case, which is similar to photoionisation of atoms or the excitation of valence band electrons into the conduction band of semiconductors, is called Bethe-Heitler pair production [38]. Similar to this but without a massive particle contributing to energy momentum conservation, at least two photons with energies E_1 and E_2 that satisfy $E_1 E_2 \geq (m_e c^2)^2$ are required. This free space, pure vacuum process is the mentioned Breit-Wheeler pair production. The angular and spectral distribution of the produced pair can be understood by describing the collision in the centre-of-momentum (COM) frame, where both photons have the same energy and collide head-on. In this frame, electron and positron are emitted in opposite directions with equal kinetic energy. The distribution on an experiment is obtained by transforming the pair back into the laboratory frame of reference, in which they follow the COM. In case one of the photons is significantly more energetic than all other photons, the pair is emitted into this direction, which can be used to design an experimental layout for pair detection.

The Breit-Wheeler process is distinguished into two major cases depending on

the number of participating photons. The original process described by Breit and Wheeler involving two colliding photons is called two-photon or linear Breit-Wheeler process whereas the case including more than two photons, typically one high energy photon colliding with many lower energy photons, is called multi-photon or non-linear Breit-Wheeler process. The specifications linear and non-linear in the two cases refer to the scaling of the reaction cross section with the colliding photon beam densities, which is linear in the two-photon case. In the multi-photon case, the reaction cross section is also linear with the high energy photon density but non-linear with the low energy photon density, which is characterised by the normalised vector potential $a_0 = \frac{eE_0}{\omega m_e c}$ of the electric field. ω is the angular frequency of the considered electric field. The cross section for the two-photon Breit-Wheeler process was calculated by Breit and Wheeler and is the relevant case for the experiment presented in this thesis. It is therefore discussed in greater detail in section 2.2.

2.1.4. Non-Linear Breit-Wheeler Pair Production

The non-linear Breit-Wheeler process is theoretically described in a very different way than Breit and Wheelers two-photon process, because it needs to include the strong electric field characterising the low energy but high density photons. More information on the theoretical description of this *strong-field QED* (SFQED) can be found in references [39, 40, 41]. This regime of pair production is further subdivided depending on the field strength. For $a_0 < 1$, which is the multi-photon case where N low energy photons react with one high energy photon, the pair production process scales with the N^{th} power of the laser intensity and can be partially described with perturbation theory. It is comparable to multi-photon ionisation of atoms in a strong electric field, which also scales with powers of the incident laser intensity. This is also the regime that was probed by the SLAC E-144 [2] experiment, which is the first experimental observation of Breit-Wheeler pair production.

If $a_0 \gg 1$, pair production occurs in the so-called non-perturbative or quasi-static regime [7], where the process is yet again subdivided into two regimes. Those are characterised by the *quantum non-linearity parameter* χ, which can be interpreted as the ratio of the electric field to the Sauter-Schwinger field in the frame of reference of a probe particle, for example an electron or a photon. The frame of reference is different whether the probe particle has a finite rest mass (χ_p) or not (χ_γ). For particles with a finite rest mass, the frame of reference is the particle rest frame and χ is defined as $\chi_p = \gamma_p \frac{E_{LAB}}{E_S} = \frac{E_{COM}}{E_S}$, where γ_p is the relativistic Lorentz factor of

the particle. For a high energy photon with frequency ω_γ colliding with a laser field, χ_γ is defined in the frame where both colliding photons have the same frequency as $\chi_\gamma = 2\frac{\omega_\gamma \hbar}{m_e c^2}\frac{E_{LAB}}{E_S}$ [41]. The two regimes of non-perturbative non-linear Breit-Wheeler pair production are now defined whether $\chi_\gamma \ll 1$ or $\chi_\gamma \gg 1$. For $\chi_\gamma \ll 1$, pair production is interpreted as a quantum tunnelling process of electrons through the vacuum barrier of $2m_e c^2$, which is significantly deformed by the strong electric field. This regime is characterised by an exponential suppression of the pair rate with $\propto \chi_\gamma \exp(-8/3\chi_\gamma)$ and shows strong similarities to high-field tunnelling ionisation of atoms, which also features an exponentially suppressed ionisation rate. The most extreme case of $\chi_\gamma \gg 1$ is characterised by a power law scaling with $\propto \chi_\gamma^{2/3}$ [42] and can be considered as the equivalent to over-the-barrier or barrier suppression ionisation. Experiments investigating non-perturbative SFQED by colliding a $a_0 \gg 1$ laser with GeV level electrons or photons where also done at Astra Gemini [7, 43, 44] but are not discussed in this thesis.

2.2. The Two-Photon Breit-Wheeler Process

The two-photon Breit-Wheeler pair production process, first described by Breit and Wheeler in 1934 [1], is the process that was probed with the experiment presented in this thesis. Breit and Wheeler considered two light waves acting on an electron in a negative energy state. They found that the wave function after the interaction contains a term that describes an electron in a positive energy state with a spin and momentum depending on its initial parameters as well as the momentum and polarisation of the incident light waves. After averaging over all possible initial electron properties, they found the probability of pair formation (electron in positive energy state) depending on the photon densities of both colliding beams and final properties of electron and positron. They further calculated the effective collision area σ for pair production in terms of n photons of energy E that propagate through a cloud of m photons with energy ϵ, however they gave only implicit formulas depending on the momenta and energies of electron and positron.

The explicit total cross section for two-photon Breit-Wheeler pair production in SI units can be found in many text books or publications, for example in references [45, 46]. It is conveniently written as

$$\sigma(\beta) = \frac{1}{2}\pi r_0^2(1-\beta^2)\left[(3-\beta^4)\ln\frac{1+\beta}{1-\beta} - 2\beta(2-\beta^2)\right] \tag{2.1}$$

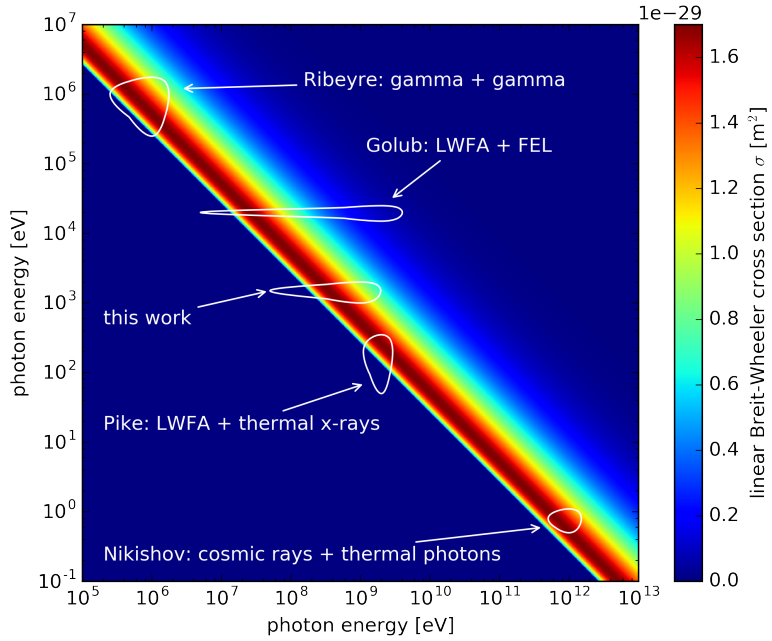

Figure 2.1.: Scaling of the BW cross section σ with the two photon energies in a head-on collision geometry. The maximum value of $\approx 1.65 \cdot 10^{-29}$ m^2 does not change with different combinations of photon energies. Some selected experimental proposals to probe the two-photon Breit-Wheeler process at different energy combinations are shown [47, 48, 8, 45] along with this work.

with the quantity β defined as

$$\beta(s) = \sqrt{1 - \frac{1}{s}} \tag{2.2}$$

and

$$s(E, \epsilon, \theta) = \frac{\epsilon E}{m_e^2 c^4} \cdot \frac{1}{2}(1 - \cos\theta). \tag{2.3}$$

Here ϵ and E are the energies of the colliding photons, θ is the collision angle and r_0 is the classical electron radius. The cross section does only depend on the product of the photon energies ϵE and does therefore not change with the specific combination of ϵ and E, which is shown on Fig. 2.1 along with a few exemplary photon energy combinations being probed with different setups. The maximum value of the reaction cross section is around $1.65 \cdot 10^{-29}$ m^2 or 165 mb. The Two-photon Breit-Wheeler pair production has the threshold requirement $s > 1$, which corresponds to the mentioned necessity to provide the rest mass energy of the pair in the COM frame. The specific

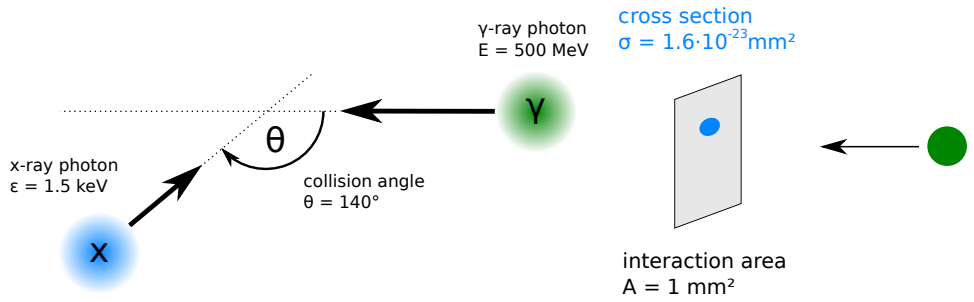

Figure 2.2.: Left: Illustration of the photon-photon collision geometry. Right: The cross section illustrated as the surface area of a target inside the collision area.

combination of photon energies determines the relative movement of the COM frame in the laboratory frame, which defines the direction in which the pair is emitted. This has implications on experimental designs, for example is a head-on collision not ideal for photon beams with equal energy because the pairs would be emitted in 2π as it is discussed by Ribeyre [47]. Asymmetric collision proposals were made for *free electron lasers* (FEL) at 10 keV that collide with 10 to 1000 MeV γ-rays [48] or thermal x-rays (100 to 400 eV) that collide with GeV class γ-photons [8]. A very unsymmetric collision that was discussed by Breit and Wheeler [1] and later by Nikishov [45] and Gould [46] is the collision and pair creation of cosmic rays with the radiation in intergalactic space, which is considered as an explanation for the absence of very high energy photons from cosmic sources far away from earth.

Typical photon energies obtained in the experiment presented in this work are high energy photons with $E = 500\,\mathrm{MeV}$ and low energy photons with $\epsilon = 1.5\,\mathrm{keV}$ colliding under an angle $\theta = 140°$, which corresponds to a cross section for the Breit-Wheeler process of $\sigma = 1.63 \cdot 10^{-29}\,\mathrm{m}^2$ as illustrated on Fig. 2.2(a) and 2.2(b).

2.2.1. Probability of Pair Formation

The probability of pair formation $p(E, \epsilon, \theta)$ per photon due to the Breit-Wheeler process with the cross section $\sigma(E, \epsilon, \theta)$ is obtained as the ratio of the cross section to the common area of both beams, which is the interaction area A of the collision as illustrated on Fig. 2.2(b).

$$p(E, \epsilon, \theta) = \frac{\sigma(E, \epsilon, \theta)}{A} \tag{2.4}$$

Pair production is a probabilistic process. When n photons in the first beam

participate in the reaction, the probability for pair creation can be written down as the inverse probability of missing on all n trials, which is approximated by the first order of the binomial series.

$$P(n, E, \epsilon, \theta) = 1 - [1 - p(E, \epsilon, \theta)]^n \approx n \cdot p(E, \epsilon, \theta) \tag{2.5}$$

This approximation is valid as long as $n \cdot p \ll 1$. In the case of two colliding beams with m photons in the second beam, the same scheme is applied again so that the probability of producing at least one pair is obtained as the inverse probability of missing on all m trials as well, which is approximated as

$$P(n, m, E, \epsilon, \theta) = 1 - [1 - n \cdot p(E, \epsilon, \theta)]^m \approx m \cdot n \cdot p(E, \epsilon, \theta). \tag{2.6}$$

For the Breit-Wheeler experiment presented in this work, the number of produced pairs is low compared to the number of incident photons in any of the beams, so that the pair creation processes of the individual photons can be assumed as being statistically independent and no saturation effects need to be taken into account. In this case, the number of produced pairs follows a binomial distribution and the expected pair yield for one collision is $\lambda = m \cdot n \cdot p$. Since the probability p is very low and the number of photons n and m is very large, the pair signal is described with a Poisson distribution, which is discussed in section 2.3.2. Realistic photon beams have a certain spectral, angular and spatial distribution, which needs to be taken into account to calculate the expected pair yield on the experiment. Due to the complexity of the collision geometry and the input beams, a numerical approach is chosen, which is presented on the next section.

2.2.2. Numerical Integration of the Collision Process

The collision process in the experiment is dynamic and has a non trivial geometry with complex spectral shapes of both photon fields, so a numerical approach is chosen to calculate the expected pair yield. The idea is to split the collision process into multiple time steps, which can be assumed as static and summed together at the end. The software used to implement the formalism is Python [49]. A 2D side view of the geometry at different time steps can be seen on Fig. 2.3(a). The photon density of the γ-ray beam is modelled as a 2D Gaussian distribution $\mathcal{N}_\gamma(r)$ with the centre line being 1 millimetre away from the x-ray source point as shown on Fig. 2.3(b). Within each time step, a loop iterates over the spatial extent of the γ-ray beam in radial direction, where the interaction region A for the radial segment from r to R is

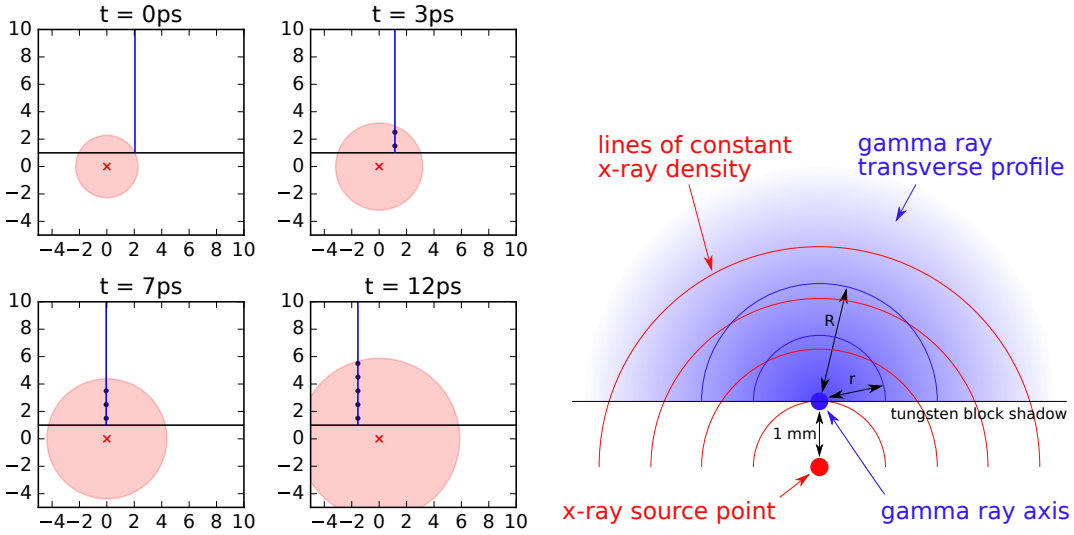

Figure 2.3.: Left: Four time steps of the collision process viewed from the side. Right: The transverse structure of both photon fields. The red circles represent the expanding x-ray cloud. The blue features symbolise the propagating γ-ray beam from right to left. When both fields overlap, pair creation is enabled, symbolised by blue dots.

$$A = \frac{\pi}{2}\left(R^2 - r^2\right). \tag{2.7}$$

The total number of γ-ray photons n contained in this radial segment is calculated with the density profile $\mathcal{N}_\gamma(r)$ at the centre of the segment at $\frac{R+r}{2}$.

$$n = A \cdot \mathcal{N}_\gamma\left(\frac{R+r}{2}\right) \tag{2.8}$$

The total number of x-ray photons m reacting with those γ-ray photons is obtained by calculating the interaction volume V and multiplying it with the x-ray density $N_x(r)$, which is modelled as a point source in three dimensions. Because both photon fields move, the interaction volume V must be obtained as the area A multiplied with the distance travelled by the γ-ray segment through the moving x-ray cloud, which is obtained with the relative velocity v of both photon fields, the length of a time step dt and the angle θ between them.

$$V = A \cdot v \cdot dt = A \cdot c \cdot (1 - \cos(\theta))\, dt \tag{2.9}$$

The angle θ is the angle between the velocity vectors of both photon fields and goes to π for a head on collision. The total number of x-ray photons traversing the γ-ray segment is therefore

$$n = V \cdot N_x(d) \tag{2.10}$$

with d being the distance from the point on the γ-ray segment to the x-ray source point. The total photon numbers n and m are now used to normalise the γ-ray and x-ray spectra, which were measured on the experiment, to obtain the accurate number of photons n_i and m_j in each energy bin, so that the expected pair yield λ for a γ-ray segment in a time step can be calculated by summing over the spectral shape of both beams.

$$\lambda_{\gamma-\text{ray segment}} = \sum_i \sum_j n_i m_j \frac{\sigma(E_i, \epsilon_j, \theta)}{A} \tag{2.11}$$

This process iterates over the full extent of the γ-ray beam, where the collision angle θ is updated accordingly to obtain the total pair yield on one time step. Finally, to obtain the pair yield for the full collision, an iteration over all time steps is performed. Since the x-ray field is dynamic, it is updated on each time step along with the collision angle depending on the position of the γ-ray beam relative to the x-ray source point. The formula for the overall pair yield from one collision can be symbolically written down as

$$\lambda = \underbrace{\sum_t \underbrace{\sum_r \underbrace{\sum_i \sum_j n_{jr} \cdot m_{jrt} \frac{\sigma(E_i, \epsilon_j, \theta_{rt})}{A_r}}_{\text{spectral shapes}}}_{\gamma-\text{ray extent}}}_{\text{time steps}} \tag{2.12}$$

and is calculated numerically.

2.3. Errors of Statistical Signals

Any experimentally measured quantity has an error margin and can thus not be determined exactly. The sources of those errors are diverse and have varying impacts for every experiment and measured quantity. Typical examples are measurement errors, systematic errors or intrinsic statistical uncertainties. Some of those can be controlled, like measurement errors, while others are fixed like intrinsic statistical uncertainties that can only be mitigated by taking more data.

On an experiment, the Breit-Wheeler process needs to be measured as an increased pair flux compared to background. This is done by separately measuring the background

level and evaluating the difference to Breit-Wheeler shots, where both measurements have error margins. The experimental challenge is to bring these errors down until they are smaller than the Breit-Wheeler pair rate. On experiments utilising LWFA electron beams, the most significant source of measurement errors is usually caused by random fluctuations of the LWFA electron beam properties like charge, spectral shape or pointing, which induces variations of the pair flux that are much larger than what is expected due to Breit-Wheeler pair production. Another source of uncertainty is the intrinsic stochasticity of the signal, which is composed of single particles instead of a continuous quantity. This is especially important for the Breit-Wheeler process due to the very low pair rates and represents a lower limit for the measurement error that cannot be mitigated except by taking more data. Those two major sources of uncertainty define if a measurement of the Breit-Wheeler process is experimentally feasible and are discussed in this section. First, the shot-to-shot fluctuation of the LWFA source is discussed in section 2.3.1 followed by a description of single particle statistics in section 2.3.2.

2.3.1. Shot-to-Shot Fluctuations

A single measurement of a randomly distributed quantity has an uncertainty that is based on the underlying distribution. For this consideration, the measured quantity is assumed to be normally distributed. The aim of a measurement may be the determination of the properties of this distribution like mean μ or standard deviation σ. A single measurement can then be interpreted as drawing a sample from this distribution. In a second step, the properties of this distribution are estimated based on the measurement. In case of a normally distributed random variable and a single measurement A, the most likely value of the mean μ is called the maximum likelihood estimate [50] $\hat{\mu}$, which is equal to the measured sample A. The uncertainty $\delta\hat{\mu}$ of this estimate is related by the standard deviation σ, however this may generally be an unknown property too since it is one of the properties that is measured. As a result, the estimate $\hat{\mu} = A$ of the mean μ has an infinite error margin in the case of only one measurement. To improve the significance of the estimate $\hat{\mu}$, multiple measurements A_i can be taken. If those are statistically independent, the maximum likelihood estimate $\hat{\mu}$ is given by the arithmetic mean of all samples:

$$\hat{\mu} = \frac{1}{N_{\text{samples}}} \sum_{i=1}^{N_{\text{samples}}} A_i \tag{2.13}$$

Here N_{samples} is the number of samples or measurements. The uncertainty $\delta\hat{\mu}$ of $\hat{\mu}$

is then given as

$$\delta\hat{\mu} = \frac{\sigma}{\sqrt{N_{\text{samples}}}}, \tag{2.14}$$

which is called the standard error of the mean, however the standard deviation σ is still unknown. It can be estimated with the corrected sample standard deviation $\hat{\sigma}$ of all samples A_i like

$$\hat{\sigma} = \sqrt{\frac{1}{N_{\text{samples}} - 1} \sum_{i=1}^{N_{\text{samples}}} (A_i - \hat{\mu})^2}. \tag{2.15}$$

Those formulas give the estimates $\hat{\mu}$ and $\hat{\sigma}$ for μ and σ with the uncertainty of $\hat{\mu}$ being characterised by the standard error of the mean $\delta\hat{\mu}$. In case of a Breit-Wheeler measurement, the pair rate μ_{BW} is defined as the difference between background μ_{BG} and collision μ_{COL} shots. The rate μ_{BW} is estimated by $\hat{\mu}_{BW}$ based on the estimates $\hat{\mu}_{COL}$ and $\hat{\mu}_{BG}$ like

$$\hat{\mu}_{BW} = \hat{\mu}_{COL} - \hat{\mu}_{BG}. \tag{2.16}$$

The uncertainty of $\hat{\mu}_{BW}$ is characterised by $\delta\hat{\mu}_{BW}$, which is obtained through propagation of uncertainty [51] from $\delta\hat{\mu}_{COL}$ and $\delta\hat{\mu}_{BG}$ as

$$\delta\hat{\mu}_{BW} = \sqrt{(\delta\hat{\mu}_{BG})^2 + (\delta\hat{\mu}_{COL})^2}. \tag{2.17}$$

The condition for a significant observation can therefore be written down as

$$\hat{\mu}_{BW} \geq x \cdot \delta\hat{\mu}_{BW}, \tag{2.18}$$

which means that the achieved uncertainty needs to be a factor x smaller than the measured signal. The factor x usually needs to be around 3 to 5 in order to declare a measurement being 'significant.' This condition can be rewritten to calculate the required number of samples or laser shots depending on the Breit-Wheeler signal-to-noise ratio $\nu = \frac{\mu_{BW}}{\mu_{BG}}$ and the relative LWFA shot-to-shot variations $\eta = \frac{\sigma_{BG}}{\mu_{BG}}$ as

$$N_{\text{samples}} \geq \frac{2x^2\eta^2}{\nu^2}. \tag{2.19}$$

Typical shot-to-shot variations of LWFA charge during long runs at Gemini are around $(200 \pm 50)\,\text{pC}$ [52] or $\eta = 25\%$, so to achieve a significance of 3 error margins and given a signal-to-noise ratio of $\nu = 0.1$, 113 background and collision shots are

required. If the signal-to-noise ratio is smaller, the required number of shots grows with the inverse square and for $\nu = 10^{-2}$ and $\nu = 10^{-3}$, $N_{\text{samples}} \approx 10^4$ and $N_{\text{samples}} \approx 10^6$ shots are required respectively.

In the end, the required number of laser shots determines if an experiment is possible. This can be improved by increasing the signal-to-noise ratio, for example by improving the shielding of background radiation while not affecting the produced pairs or by utilising tracking detectors to distinguish between background and Breit-Wheeler pairs. Another method is stabilising the LWFA process and thereby decreasing shot-to-shot variations, however the most effective way to control shot-to-shot variations is by measuring them on shot. If this can be done, the obtained yield can be corrected for those, reducing the effective shot-to-shot variations. In the theoretical limit of negligible shot-to-shot fluctuations ($\eta \to 0$), the uncertainty goes to zero and a single shot for background and collision would give a measurement with infinite significance, however this cannot be realised on an experiment because there are always errors that cannot be completely determined. Another independent source of uncertainty that is a limiting factor for a Breit-Wheeler process measurement is the intrinsic single particle nature of the signal. The statistical behaviour of such a point process can be described by Poisson statistics, which is presented in the following paragraph.

2.3.2. Poisson Statistics of Single Particle Signals

The number of pairs from the Breit-Wheeler process or from background can only be measured in multiples of single particles, which has implications on the accuracy of a measurement and is therefore described by the Poisson distribution $f(k, \lambda)$ [53].

$$f(k, \lambda) = \frac{\lambda^k e^{-\lambda}}{k!} \tag{2.20}$$

It describes the probability density of point processes and can be derived from the binomial distribution in the limit of infinite trials n with a vanishing probability p while keeping the mean rate $np = \lambda$ constant [54, 55]. For Breit-Wheeler pair formation this is the case, because many photons interact with each other and the chance per photon is very low. Similar to the process described in section 2.3.1, measuring the pair yield A on a single shot is drawing a sample from a Poisson distribution with a mean rate λ that is defined by Eq. 2.12, denoted as

$$A \sim \text{Pois}(\lambda). \tag{2.21}$$

The obtained value A is then used to estimate the rate λ. The maximum likelihood

estimate $\hat{\lambda}$ for λ is the measured value A.

$$\hat{\lambda} = A \tag{2.22}$$

However, this estimate has an uncertainty because A is just one random sample and generally not equal to the rate λ. This uncertainty is expressed in terms of a probability p, the confidence level, so that the true rate λ is within an interval $\delta\hat{\lambda}_p$, called confidence interval, around the estimate $\hat{\lambda}$. In return, $1-p$ is the false alarm probability that λ is not within $\delta\hat{\lambda}_p$. To determine the lower and upper limit of the confidence interval, the cumulative distribution function $P(\lambda, A)$ of the Poisson distribution may be used, which gives the total probability of observing A or less than A events with a rate λ [56].

$$P(\lambda, A) = \sum_{k=0}^{A} \frac{\lambda^k e^{-\lambda}}{k!} \tag{2.23}$$

The lower (upper) limit $\lambda_{p,1}$ ($\lambda_{p,2}$) is defined as the rate of a Poisson distribution so that the probability of observing A-1 (A) or less events is greater (less) than $\frac{1+p}{2}$ ($\frac{1-p}{2}$) [56].

$$P(\lambda_{p,1}, A-1) = \frac{1+p}{2} \tag{2.24}$$

$$P(\lambda_{p,2}, A) = \frac{1-p}{2} \tag{2.25}$$

Those equations need to be solved for the associated rates $\lambda_{p,1}$ and $\lambda_{p,2}$. Therefore the cumulative distribution function is rewritten by taking the derivative with respect to λ. This approach is further described by Garwood [56].

$$\frac{d}{d\lambda}P(\lambda, A) = \frac{d}{d\lambda}\left(\sum_{k=0}^{A}\frac{\lambda^k e^{-\lambda}}{k!}\right) = \frac{d}{d\lambda}\left[e^{-\lambda}\left(1+\frac{\lambda}{1!}+\frac{\lambda^2}{2!}+...+\frac{\lambda^A}{A!}\right)\right] \tag{2.26}$$

$$= e^{-\lambda}\left[\left(1+\frac{2\lambda}{2!}+...+\frac{A\lambda^{A-1}}{A!}\right)-\left(1+\frac{\lambda}{1!}+\frac{\lambda^2}{2!}+...+\frac{\lambda^A}{A!}\right)\right] \tag{2.27}$$

$$\frac{d}{d\lambda}P(\lambda, A) = -\frac{\lambda^A e^{-\lambda}}{A!} \tag{2.28}$$

Now the fundamental theorem of calculus may be applied:

$$\int_0^{\lambda}\left[\frac{d}{d\lambda'}P(\lambda', A)\right]d\lambda' = P(\lambda, A) - P(0, A) \tag{2.29}$$

Inserting Eq. 2.28 gives an alternative expression for the cumulative distribution function $P(\lambda, A)$ in the form of an integration over λ instead of summing over k:

$$P(\lambda, A) = 1 - \int_0^{\lambda} \frac{\lambda'^A e^{-\lambda'}}{A!} d\lambda' \tag{2.30}$$

Garwood [56] solved this equation for $\lambda_{p,1}$ and $\lambda_{p,2}$ by testing values for A by hand, which can only be integers, until the conditions 2.24 and 2.25 are satisfied, however the obtained Breit-Wheeler data may yield very high values for A and an iterative solution by hand is not necessary with modern computers. Therefore a numerical solution is chosen based on the relation of the cumulative distribution functions of the Poisson and Gamma distribution [57], which is

$$P(\lambda, A) = 1 - F(\lambda, A + 1, 1). \tag{2.31}$$

Here $F(k, \alpha, \beta)$ is the regularised gamma function with shape parameter $\alpha = A + 1$ and rate parameter $\beta = 1$. The conditions 2.24 for $\lambda_{p,1}$ and 2.25 for $\lambda_{p,2}$ are now

$$F(\lambda_{p,1}, A, 1) = 1 - \frac{1+p}{2} = \frac{1-p}{2} \tag{2.32}$$

and

$$F(\lambda_{p,2}, A + 1, 1) = 1 - \frac{1-p}{2} = \frac{1+p}{2}. \tag{2.33}$$

This step is only done to enable a numerical solution using the computer software python [49] and is only valid if A is an integer. The inverse of $F(k, \alpha, \beta)$, referred to as a percent point or quantile function, and can be obtained with the python package scipy [58].

$$\lambda_{p,1} = \textbf{scipy.stats.gamma.ppf((1-p)/2, A, loc=0, scale=1)} \tag{2.34}$$

$$\lambda_{p,2} = \textbf{scipy.stats.gamma.ppf((1+p)/2, A+1, loc=0, scale=1)} \tag{2.35}$$

For an example value of $A = 10$ events and a statistical significance of $p = 0.9$, the lower and upper limits are $\lambda_{0.9,1} \approx 5.43$ and $\lambda_{0.9,2} \approx 16.96$. The confidence interval of λ_p around the maximum likelihood estimate $\hat{\lambda} = 10$ for the confidence level $p = 0.9$ is therefore

$$5.43 < \lambda_p < 16.96 \tag{2.36}$$

or

$$\lambda_p = 10^{+6.96}_{-4.57}. \tag{2.37}$$

Accordingly, the probability to measure 9 (10) or less events with a rate of $\lambda_{0.9,1}$ ($\lambda_{0.9,2}$) is 95% (5%). This method determines the confidence interval of the rate that describes a Poisson distributed measured variable. A Breit-Wheeler measurement will be realised as two separate measurements of the rate on background and collision shots, each with their own confidence interval. The overlap of those intervals allows the formulation of a significance of the difference between those measurements and therefore for the Breit-Wheeler measurement as a whole, which is presented in the next paragraph.

Significance of a Difference

The Breit-Wheeler process is measured as a difference between background and collision shots. Besides the absolute difference $\lambda_{BW} = \lambda_{COL} - \lambda_{BG}$, the confidence in the difference is a very important value to characterise the measurement, which is also called the significance of an observation. This significance is expressed by the largest possible confidence level p at which the confidence intervals around the estimated rates λ_{COL} and λ_{BG} do not yet overlap. In other words, what is the highest confidence level at which the upper bound of λ_{BG} is just below the lower bound of λ_{COL}. This limit can be defined as

$$\lambda_{p,2,BG} = \lambda_{p,1,COL} \tag{2.38}$$

with $\lambda_{p,2,BG}$ being the upper boundary of the confidence interval of λ_{BG} at confidence level p and $\lambda_{p,1,COL}$ being the lower boundary of the confidence interval of λ_{COL} for the same confidence level p. This equation is solved numerically for p and with example values of $\lambda_{BG} = 10$ and $\lambda_{COL} = 20$, the statistical significance is $p \approx 0.76$. In physics and other sciences, an observation is often considered 'significant' if the confidence is larger than the $3\,\sigma$ equivalent of a normal distribution, which corresponds to a probability of $\approx 99.73\%$. This confidence in the difference needs to be reached for a measurement of the Breit-Wheeler process. Because it is limited by the intrinsic stochasticity of the pair signal, which is composed of single particles, it can only be

reached by taking sufficiently large amounts of data. This is calculated in the next paragraph.

Required Sample Size for a given Confidence

Section 2.3.1 deduced a limitation of the achievable measurement accuracy based on shot-to-shot fluctuations, which lead to the requirement of a certain amount of shots to reach a specific accuracy. The intrinsic stochasticity of a single particle signal limits the achievable accuracy in a similar way, but since the samples of this process are particles instead of shots, the limitation is formulated in terms of a minimum number of measured particles. A major difference is that the particle signal is assumed to follow a Poisson distribution, which links the standard deviation to the mean and thereby reduces the number of parameters by one. In a comparison of background and collision shots of a Breit-Wheeler measurement, both sample means are expressed relative to each other via the signal-to-noise ratio ν, so that the only remaining parameters are the confidence p and one quantity determining the absolute sample size either on background or collision shots, or the absolute difference, which is the number of particles produced through the Breit-Wheeler process. The limit set by the single particle nature of the signal is therefore well defined by the signal-to-noise ratio and the desired confidence level, nothing more. The expression is equal to equation 2.38 but is solved for λ_{BG}, λ_{COL} or λ_{BW}.

$$\lambda_{p,2,BG} = \lambda_{p,1,COL} \tag{2.39}$$

For the exemplary $3\,\sigma$ limit and a signal-to-noise ratio of $\nu = 0.1$, the solution is $\lambda_{BG} \approx 3798.4$, $\lambda_{COL} \approx 4178.3$ and $\lambda_{BW} \approx 379.8$. This means that ≥ 380 produced Breit-Wheeler pairs need to be measured, which based on the signal-to-nose ratio means ≥ 3799 background pairs or ≥ 4179 pairs on collision shots. In case the signal-to-noise ratio is lower, the required sample size grows approximately with the inverse square similar to the shot based consideration. The required number of produced pairs for $\nu = 10^{-2}$ and $\nu = 10^{-3}$ are $\lambda_{BW} \geq 3620$ and $\lambda_{BW} \geq 36.020$ respectively. This required number of Breit-Wheeler pairs λ_{BW} can be translated to a number of shots under the assumption of a mean pair rate per shot μ_{BW} and will combine with the limit set by shot-to-shot fluctuations in section 2.3.1, however even for high shot-to-shot fluctuations of $\eta = 0.25$ and high pair rates of $\mu_{BW} = 1$ per shot, the limit is defined by the total number of pairs. Considering a correction with charge measurements per shot that decrease effective shot-to-shot fluctuations to around $\eta = 0.01$ and realistic

pair rates of 10^{-3} per shot, the limitation for the required number of shots is vastly dominated by single particle statistics.

Normalisation

A Poisson distribution is characterised by the rate parameter λ, which gives the number of events per normalisation unit. For the Breit-Wheeler process, this normalisation unit is the entire incident photon field. As a result, a comparison between background and collision shots is only a valid measurement of the Breit-Wheeler process if the incident photon fields are identical. On an experiment, the determination of the exact normalisation is impossible and can only be done to a certain degree depending on the measurable quantities. Any uncertainty of those normalisation quantities will increase the error margin around the estimated rates λ_{COL} and λ_{BG} and will decrease the significance of the measurement. To account for these, the significance is obtained after normalising the calculated confidence intervals with the measured total LWFA charge. The reason for this approach is further discussed while presenting the data evaluation methodology in section 3.7.3 along with the way how measurement errors are folded into the calculation of the significance.

Approximation for Large Samples

The formulation of limits for a Poisson confidence interval and the subsequent tabular or numerical solution makes it not ideal for quick checks during an ongoing experiment, so an approximation for large samples shall be presented here. This is possible by using the central limit theorem [53], which states that the sum of independent random variables tends towards a normal distribution.

$$A \sim \sum_{i=1}^{n} \mathrm{Pois}(\lambda_\mathrm{i}) \xrightarrow{n\to\infty} \mathcal{N}(\mu, \sigma) \tag{2.40}$$

In case of a Poisson distributed random variable, the sum tends towards a special normal distribution that keeps the relation between its mean μ and standard deviation σ such that $\sigma = \sqrt{\mu}$.

$$\mathcal{N}(\mu, \sigma) = \mathcal{N}(\mu, \sqrt{\mu}) \tag{2.41}$$

The maximum likelihood estimate of the mean μ is the mean of the Poisson distribution $\lambda = \sum_{i=1}^{n} \lambda_i$, which can be estimated by $\lambda \approx \hat{\lambda} = A$, so A approximately follows a normal distribution $\mathcal{N}(\mu, \sqrt{\mu})$ with $\mu = A$.

$$A \sim \sum_{i=1}^{n} \mathrm{Pois}(\lambda_\mathrm{i}) \approx \mathcal{N}(A, \sqrt{A}) \tag{2.42}$$

The error margin around A can now easily be expressed in x multiples of the standard deviation, which is $\sigma = \sqrt{A}$.

$$A - x \cdot \sqrt{A} \leq A \leq A + x \cdot \sqrt{A} \tag{2.43}$$

A second set of samples representing the collision shots $B = A(1 + \nu)$ follows the same rule and the condition for a statistical significance of the difference between A and B of x standard deviations can now be written as

$$A + x \cdot \sqrt{A} \leq B - x \cdot \sqrt{B}. \tag{2.44}$$

This term can be solved analytically after inserting $B = A(1 + \nu)$ to either obtain an expression for $A(x, \nu)$ or $x(A, \nu)$.

$$A \geq \left[\frac{x}{\nu}\left(1 + \sqrt{1 + \nu}\right)\right]^2 \tag{2.45}$$

$$x \leq \frac{\nu\sqrt{A}}{1 + \sqrt{1 + \nu}} \tag{2.46}$$

For low signal-to-noise ratios ν, the required number of samples A to reach a certain statistical significance of x standard deviations can be further approximated with

$$A \geq \left[\frac{x}{\nu}\left(1 + \sqrt{1 + \nu}\right)\right]^2 \underset{\nu \lesssim 1}{\approx} \frac{x^2}{\nu^2}\left(4 + 2\nu\right) \underset{\nu \lesssim 0.01}{\approx} \frac{4x^2}{\nu^2}. \tag{2.47}$$

3. Experimental Methods

This chapter presents the experimental setup to measure the Breit-Wheeler process at Astra Gemini and is composed of two major parts. A schematic overview of all components except cameras and laser diagnostics is shown as a guideline on Fig. 3.1.

The first part covering sections 3.1 to 3.4 presents experimental components and methods used to enable the Breit-Wheeler process. It starts with a brief description of the laser system in section 3.1 followed by the generation of the two colliding photon beams. The production of the high energy γ-ray beam is described in section 3.2 (Gas cell, Plasma Mirror, Converter, W block, Collimator Gamma Profile and Gamma Spectrometer on Fig. 3.1) and the production of the high density x-ray field is presented in section 3.3 (Ge Target, Crystal Spectrometer and Pinhole Camera on Fig. 3.1). This first part of chapter 3 closes with a description of the alignment procedure to achieve spatial and temporal overlap of both photon fields at the Breit-Wheeler interaction point (Interaction Point on Fig. 3.1) in section 3.4 to enable the Breit-Wheeler process.

The second major part of chapter 3 covers sections 3.5, 3.6 and 3.7. It presents the components of the pair detection system that were developed within this PhD project (Single Particle diagnostics on Fig. 3.1) and starts with the spectral filter chicane for LWFA electrons in section 3.5 (not shown on Fig. 3.1). This is followed by a description of the analyser magnet system (AMS) in section 3.6 (Dipole Magnets in Single Particle Diagnostics part on Fig. 3.1), a magnetic beam line to guide the produced Breit-Wheeler pairs to the single particle detectors (SPD). The experiment used two distinct and independent types of single particle detectors, a CsI scintillator based and a semiconductor type (Timepix3) detector. This thesis will focus on the CsI scintillator based single particle detector because they are part of the PhD project, which are presented in section 3.7. The Timepix3 semiconductor type detectors are described in reference [59]. An explanation of the calibration and evaluation methods to quantify the positron yield on the CsI scintillator type single particle detector as well as a description of the statistical data analysis is also included in section 3.7.

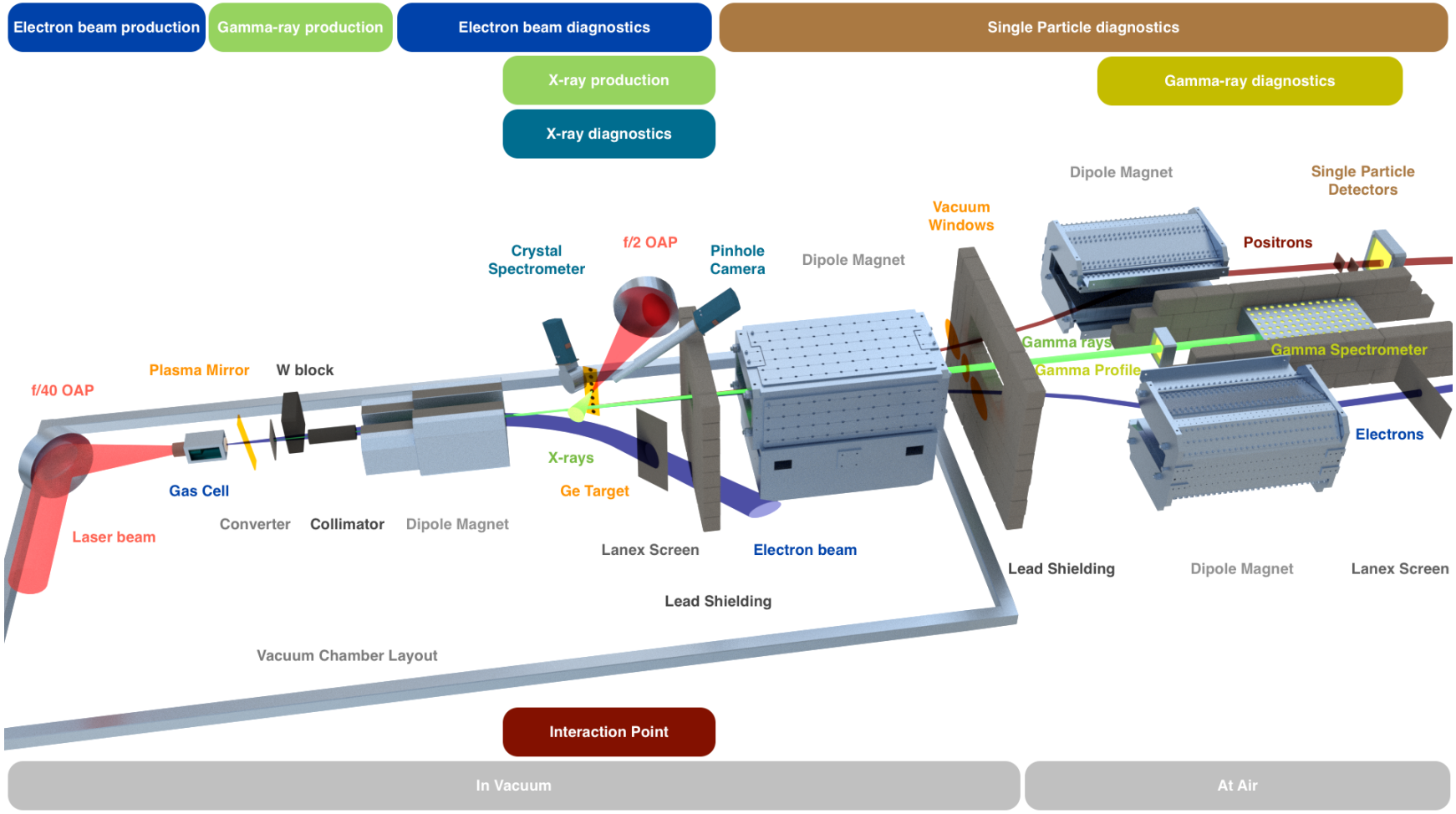

Figure 3.1.: The experimental setup. This image is provided with courtesy of Elias Gerstmayr.

3.1. The Gemini Laser System

The experiment presented in this work was performed at the high-power laser system Astra Gemini, operated by the Central Laser Facility at Rutherford Appelton Laboratories near Didcot in Oxfordshire, England. It is a state-of-the-art titanium-doped sapphire laser that operates at a central wavelength of 800 nm and features two independent laser beams with design parameters of 15 J pulse energy within 30 fs duration to achieve a peak power of 0.5 PW [60, 61]. The usual parameters that are achieved on routine experiments are around 10 J within 40 fs pulses on target that can be focused to intensities in excess of $10^{21}\,\mathrm{W/cm^{-2}}$ [43, 44, 52].

The system is composed of several components, starting with the front end. This is based on an oscillator that delivers laser pulses with a duration of 12 fs. These are stretched to 7 ps at the millijoule energy level and kHz repetition rate, of which 10 pulses per second are subsequently selected by a fast Pockels cell [62]. In a next step the pulses are stretched further to 1060 ps and amplified in three stages. The first of which amplifies the seed pulse to 4 mJ, smooths its intensity profile and expands it to 6 mm diameter [63]. The second amplifier boosts the energy to 120 mJ and expands the beam to 15 mm diameter with a flat-topped profile [64] followed by the third amplifier increasing the energy further to 1.2 J [65]. Up to this point the laser system is called *Astra* and every second pulse can be used for experiments in dedicated target areas. Every other pulse is sent to *Gemini*, the final amplifier stage first commissioned in 2008, hence the name *Astra Gemini*. At Gemini, the pulses are first split in two and then independently amplified up to 26 J [66]. The final stage is the compressor, one for each beam, which compresses the pulses to durations of 30 fs (typically 40 fs on experiments). After compression, 15 J of energy remain and the beams have a nominal power of 500 TW (typically 250 TW on target). Pulses can be fired at a rate of one every 20 seconds [67].

The design of two independent amplifiers and compressors allows a large variety of experiments, which is especially valuable for this Breit-Wheeler experiment as the energies, durations and relative timing need to be adjusted. The LWFA driver beam needs to be limited to 8 J due to the necessity of a turning optic between the focussing optic and the focal spot while the x-ray driver needs to have full power. The x-ray driver is stretched to 40 ps to optimise the x-ray yield while the LWFA driver is compressed to 40 fs. The production of γ-rays from LWFA electrons is presented in the next section, followed by the production of x-rays in the section after that.

3.2. High Energy γ-ray Beam

This section presents the process of converting Geminis south beam (LWFA driver beam) containing around $3 \cdot 10^{19}$ photons at 1.5 eV into a collimated γ-ray beam with populations around $7 \cdot 10^5$ photons above the pair detection threshold of 230 MeV. It includes the LWFA stage to accelerate electrons to several 100 MeV and the converter stage to generate high energy γ-rays through bremsstrahlung as well as the collimator and tungsten block to shape the γ-ray beam for the Breit-Wheeler interaction.

3.2.1. Laser Wake Field Acceleration

The very first step of the laser to γ-ray beam conversion process is the LWFA stage, which has one major component, the gas target. It is a hollow metal box that can be filled with a light gas, in this case helium with 2% of nitrogen, and features small entrance and exit apertures at the front and rear surface for the laser beam to propagate through. The gas is injected milliseconds before the laser shot arrives to provide a steady state gas density inside the cell, which is ionised by the laser pulse. On an LWFA setup, the laser intensity is chosen in such a way that it is sufficiently intense to drive a plasma wake, which develops very strong electric fields that can accelerate electrons to several hundred mega electronvolt over a few millimetres. Such targets are generally referred to as gas cells and are developed by many research groups with various designs and concepts, each optimised for different electron beam properties. The particular cell used on this experiment, shown on Fig. 3.2, has a comparably simple yet effective design featuring a single stage with a homogeneous density profile. By using a doped gas with 2% of nitrogen, electrons can be injected into the plasma wake through ionisation of various nitrogen shells in a process called ionisation injection to be subsequently accelerated. The design of such LWFA targets and understanding the dynamic behaviour of the acceleration process is a very active field of research. The interested reader is referred to the PhD theses of S. Kuschel [68] and, specifically for Gemini, of K. Poder [52]. On this experiment, the laser pulse wave front is optimised with an adaptive optic and focussed with an F/40 spherical mirror. The adaptive optic had a sufficiently large range of motion to correct for spherical aberrations of the focal spot, which had a size of 44 µm × 53 µm (FWHM). The estimated energy contained inside the spot was 5.5 ± 0.6 J, which correlates to a normalised vector potential of $a_0 = 1.1 \pm 0.2$. The electron density of the laser ionised plasma inside the gas cell was $(2.6 \pm 0.4) \cdot 10^{18}\text{cm}^{-3}$ and the acceleration length was 17.5 mm.

After the acceleration process, the remaining laser light exits the cell together

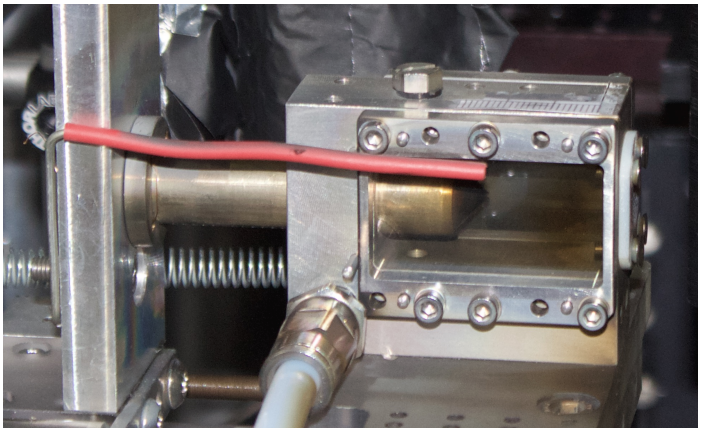

Figure 3.2.: A photograph of the gas cell used to accelerate electrons via LWFA to several 100 MeV. The bronze cylinder is the entrance cone and has a fixed position in space. The rest of the cell moves relative to that to adjust the acceleration length.

with the electron beam, where the intensity is still high enough to cause damage to components further down the beam line, so a specialised device to dump the beam is needed. On Gemini, this device is a 125 µm Kapton tape, which is located a few centimetres downstream of the gas cell. When it is hit by the laser, the upper layer of the surface is ionised and acts like a plasma mirror, reflecting the majority of the beam into a safe corner of the vacuum chamber whereas the electron beam is barely affected and propagates through the Kapton. To avoid degradation over time, the tape is spooled on a pair of wheels and is renewed after every laser shot.

To measure the energy of the accelerated electrons, a permanent magnet of 30 cm length and a magnetic field induction of 1 T was inserted into the beam line to disperse the electrons, which were subsequently recorded on a Lanex scintillation screen coupled to an Andor NEO CCD. The energy of the electrons can be calculated from the deviation caused by the magnetic field. The width of the beam perpendicular to the magnet dispersion axis is used to measure the divergence and the intensity of the scintillation light corresponds to the number of electrons and therefore the charge density of the beam. A calibrated example image of this electron spectrometer is shown on Fig. 3.3. Typical electron beam parameters obtained on this experiment were energies of 500 MeV, divergences of 2.2 mrad (FWHM) and charges between 20 pC and 50 pC.

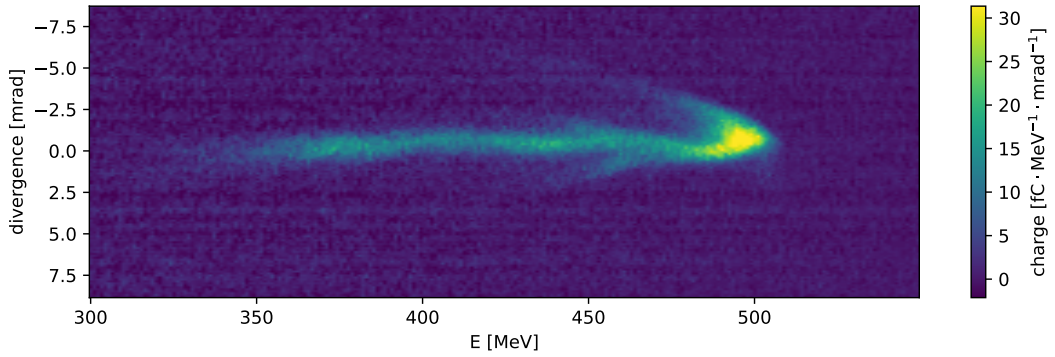

Figure 3.3.: An typical image of the electron spectrometer. Obtained beam properties on this experiment were energies of 500 MeV, 20 to 50 pC total charge (above 350 MeV) and around 1 mrad (gauss std) divergence.

3.2.2. Electron to Photon Conversion

The second stage in the beam conversion chain is the converter stage, which is composed of the converter targets, the collimator and the tungsten block shown on Fig. 3.4. The converter target is a few millimetres thick plate of high-Z material, typically Bismuth or Tungsten, which is penetrated by the electron beam. During this process, the electrons are decelerated by the electric fields around the atomic cores and loose kinetic energy, which is emitted as photons. This process is called Bremsstrahlung and produces radiation with a distinct spectral shape shown on Fig. 3.5, which is characterised by the end point energy defined by the electron energy. The photons are emitted under an angle relative to the initial electron trajectory, which depends on their energy. As a result, more energetic photons have a lower divergence and are closer to the axis, which is exploited by the collimator, a 10 cm long hollow cylinder with 2 mm inner and 20 mm outer diameter made of solid tantalum. The purpose of the collimator is to block low energy, high divergence γ-rays that do not contribute to the Breit-Wheeler process in order to lower background radiation on the detectors to increase the signal-to-noise ratio.

The detection of this type of high energy radiation was done with two crystal scintillators. One of which is a stack of 20 by 20 thallium doped caesium iodide (CsI(Tl)) crystals that are aligned parallel to the beam propagation direction. Each crystal has an individual layer of reflective coating to avoid optical cross talk between neighbours. When high energy photons hit the crystals, scintillation light is emitted and detected by an Andor iXon camera. The amount of scintillation light corresponds to the deposited energy and by extension to the beam intensity. This diagnostic

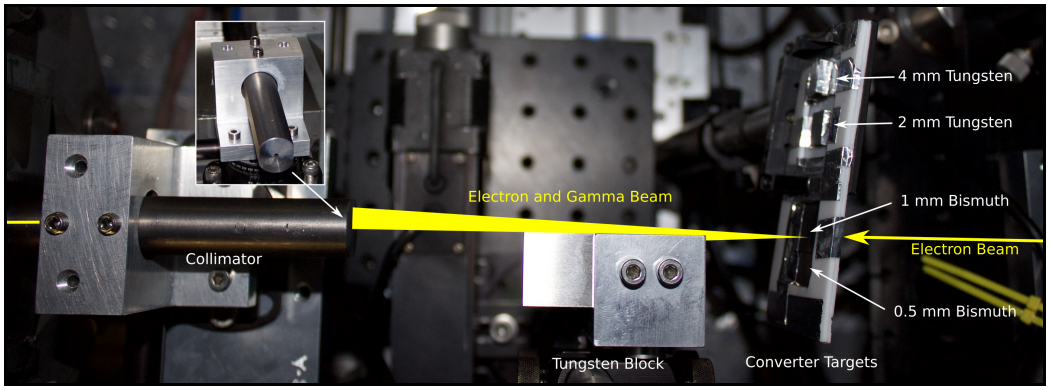

Figure 3.4.: A Photograph showing the converter stage from above. The electron beam hits a converter target on the right to produce a high energy γ-ray beam, which is obscured by the tungsten block and collimated by the collimator to form the D-shape.

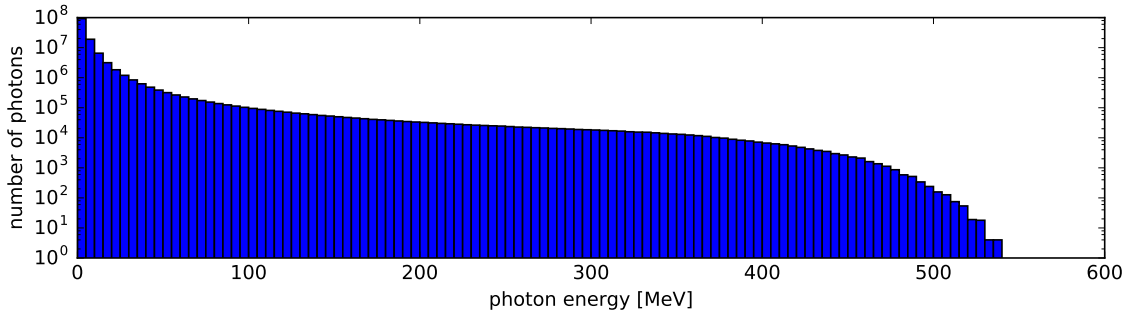

Figure 3.5.: The calculated γ-ray spectrum produced by the electron beam from Fig. 3.3 in a 1 mm Bismuth converter target.

was used to measure the spatial profile, divergence and pointing of the γ-ray beam as well as an approximate intensity, which was used to normalise the yield on the single particle detectors and is described in section 3.7. It was also used to align the collimator and tungsten block relative to the γ-ray beam by observing the shadow, which is exemplarily shown for three configurations on Fig. 3.6.

Another important property of the γ-ray beam is the spectral shape, which is difficult to measure. A simple but inaccurate approach is measuring the penetration depth into a scintillator. This works because higher energy γ-rays will deposit the majority of their energy further into the crystal [69]. To realise this, a stack of CsI(Tl) crystals arranged perpendicular to the beam propagation direction was placed behind the γ-ray profile stack, so that the scintillation light is emitted from the side rather than the back. The crystals are shielded from one another to avoid optical cross talk and are enclosed in an aluminium frame with circular windows, which make the individual

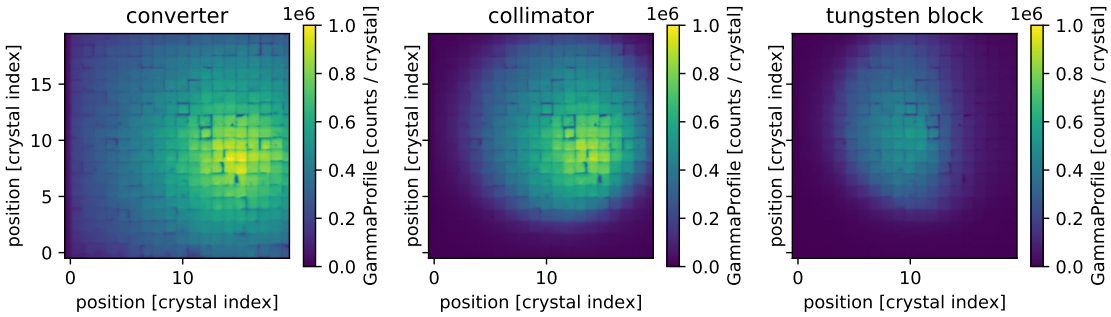

Figure 3.6.: Example images of the γ-ray profile diagnostic to show the alignment procedure of collimator and tungsten block relative the γ-ray beam. Left: Only the converter target is inserted. Centre: The collimator was added and the circular aperture is visible. Right: The tungsten block was added to block half of the γ-ray beam to create the D-shape.

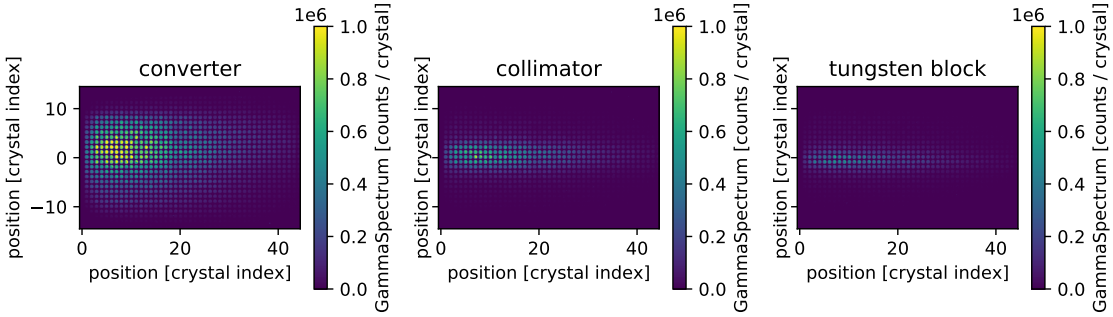

Figure 3.7.: Images of the γ-ray spectrum diagnostic. The beam enters from the left. Left: Only the converter target is inserted. Centre: The collimator was added. Right: The tungsten block was added.

crystals appear round in shape. Three example shots with converter, collimator and tungsten block inserted similar to the profile diagnostic are shown on Fig. 3.7. The reconstruction of the spectral distribution of the γ-ray beam from this diagnostic was evaluated by Elias Gerstmayr in his PhD thesis [70], however the results had a large uncertainty so that the calculation of the bremsstrahlung spectrum from the measured electron beams is used as a measure of the γ-ray spectral shape within this thesis.

After the converter stage, the overall beam consists of the produced high energy γ-rays and the remaining LWFA electrons as well as electron positron pairs produced via the Bethe-Heitler process inside the converter. These pairs have similar properties compared to Breit-Wheeler pairs, so they would be detected as false positives. Additionally, the primary LWFA electron beam would go all the way to the electron side of the sensitive single particle detectors, making Breit-Wheeler electron detection impossible. In order to provide a clean photon beam for the Breit-Wheeler reaction it

is mandatory to remove the electrons and positrons from the γ-ray beam before they enter the Breit-Wheeler interaction region. This is done with the electron spectrometer magnet located downstream of the converter stage, which deflects electrons and positrons away from the axis to provide a clean γ-ray beam.

3.3. High Intensity x-ray Field

The second ingredient to enable two-photon Breit-Wheeler pair creation together with the several 100 MeV γ-ray beam is a high intensity photon field with energies around a few kilo electronvolt, so well above the 1.5 eV of the Gemini laser. Therefore the laser light needs to be converted into hard x-rays, which was realised with a solid state germanium target. The idea is to heat and ionise a small sample of germanium to use the atomic transition radiation from M-L shells in the range of 1 to 2 keV. This process can be driven very effectively, reaching energy conversion efficiencies of several percent by optimising laser intensity, irradiation time and target properties. For that, Geminis north beam was tuned to optimise germanium heating by stretching the pulses to 40 ps FWHM duration and focussing to a large spot of 210 µm × 90 µm achieving $2 \cdot 10^{15}\,\mathrm{W/cm^2}$. The layer of germanium had a thickness of around 100 nm, which is too thin to support itself on macroscopic scales, so a 25 µm Kapton tape was used as a carrier substrate. To minimise the absorption of the produced x-ray radiation by the Kapton substrate, each germanium sample was placed inside an etched region of 5 µm thickness. A schematic of the Germanium target tape is shown on Fig. 3.8. Many of those targets were placed on the Kapton tape, which was spooled on wheels to renew the germanium sample on every shot. The prototype deployed on this campaign had no active feedback for alignment, so it needed to be manually adjusted on every shot, which defined the operational repetition rate for Breit-Wheeler shots. Since the solid state target is ionised for many 10 ps before the γ-beam passes just 1 mm away and is subsequently destroyed on each shot, there is a finite probability that debris might reach the γ-ray beam and create pairs via Bethe-Heitler pair production. Those pairs would only be measurable on dual beam shots and are therefore candidates for false positive events in a Breit-Wheeler measurement. Although the target was designed to contain the plasma on ps time scales, this effect was measured with deliberately offset timing shots and is discussed further in chapters 4 and 5. The development of this novel x-ray target, which made the two-photon Breit-Wheeler experiment possible at Astra Gemini, was done by collaborators from Imperial College London, University of Oxford and AWE.

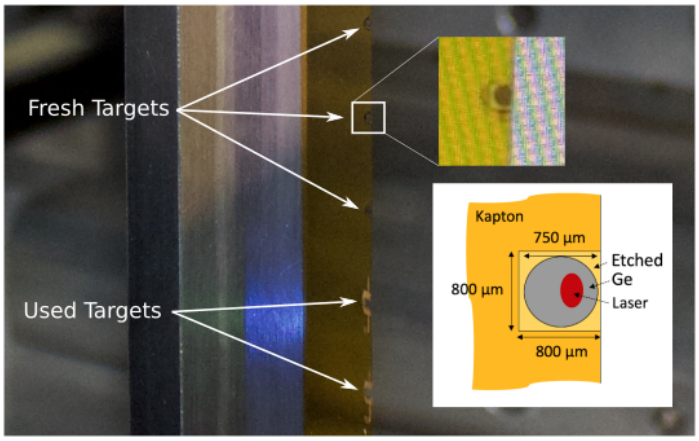

Figure 3.8.: A photograph showing the Kapton tape (orange) with the germanium targets (dark spots) on it. The schematic on the bottom right is provided with courtesy of Imperial College London, University of Oxford and AWE.

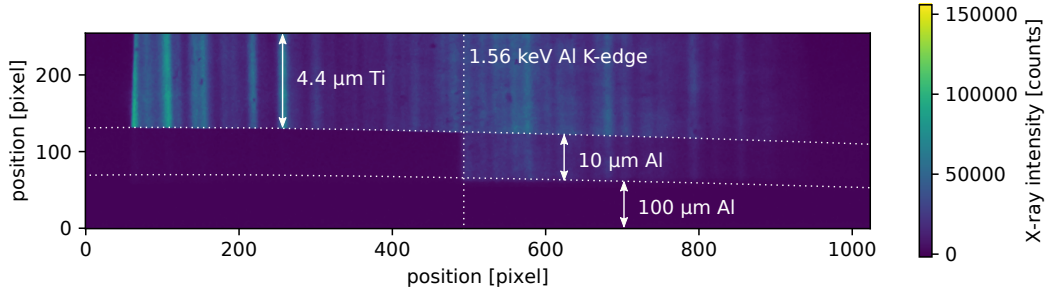

Figure 3.9.: An example image of the x-ray spectrometer. The vertical lines indicate germanium M-L shell transition lines and the horizontal intensity steps are (from top to bottom) 4.4 µm Titanium, 10 µm Aluminium and ≈ 100 µm Aluminium filters. The vertical Aluminium K-edge around 1.56 keV at pixel 500 is used as a spectral reference.

The x-ray field was characterised by two diagnostics, a crystal spectrometer and a pinhole camera. The latter is used to determine the size and alignment of the x-ray source, which was found to be 400 µm × 200 µm large. The spectral shape was obtained by reflecting the x-rays on a thallium acid phthalate (TlAP) crystal, which causes constructive interference of x-rays of a specific wavelength at specific angles according to Bragg's law of diffraction. With this method, the spectral shape was determined and the intensity was deduced from the signal on the calibrated Andor DX-420-BN CCD in combination with various filters shown on Fig. 4.2. The majority of the x-ray diagnostic analysis was done by Cary Colgan from Imperial College London, who permitted the use of his data within this thesis.

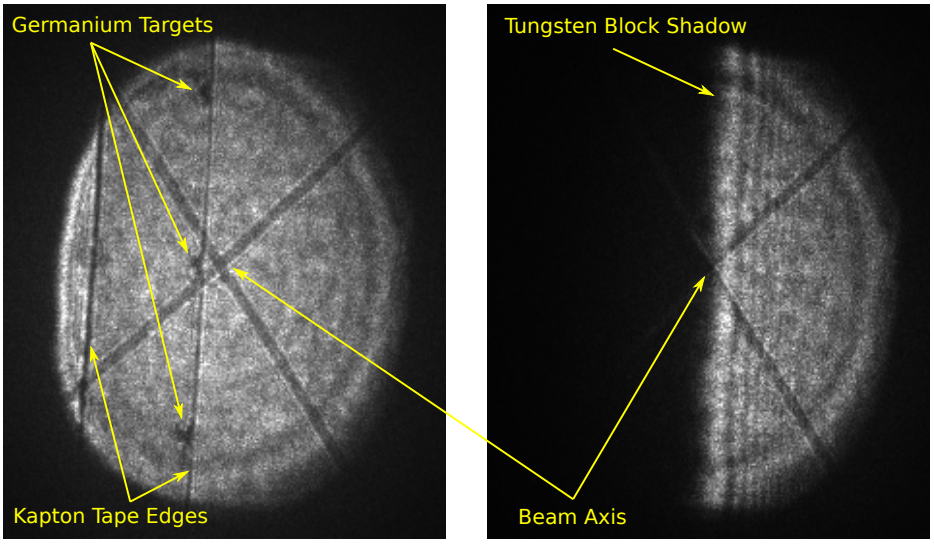

Figure 3.10.: Images of the spatial alignment camera showing Geminis south beam with a cross hair indicating its centre. Left: The full beam profile is visible with a shadow cast by the Kapton tape and the Germanium targets on it. The target in the centre is 1 mm off axis. Right: The shadow cast by the Tungsten block is visible to shield the target from γ-rays.

3.4. Spatial and Temporal Overlap

To enable the Breit-Wheeler process, the two photon fields must be overlapped in space and time which is done at the Breit-Wheeler interaction point. The spatial overlap was achieved with an alignment beam and a cross hair to mark the centre, which was also used to align the tungsten block to shield the Kapton tape from the γ-ray beam. An example view of this diagnostic is shown on Fig. 3.10. The timing between the two beams at Gemini is controlled by a dedicated delay line, where a pair of mirrors can be driven to change the optical path of one of the beams to adjust the relative timing. This was measured at the Breit-Wheeler interaction point using a photodiode with a signal rise time of several 10 ps, which is not precise enough to ensure a good overlap of the beam peaks considering the 40 fs long LWFA driver. To overcome this, the relative timing between both beams was measured for various delay line positions ahead and beyond optimum overlap. The position for peak overlap was then determined with a linear interpolation to the centre. The timing jitter between both beams was measured on previous experiments with optical interferometry and found to be less than 10 fs [71]. The spatial overlap jitter, which is determined by the LWFA electron beam pointing in the range of milliradians is negligible at the interaction point due to the millimetre scale of the x-ray cloud and γ-ray beam aperture.

3.5. Spectral Filter Chicane for LWFA Electrons

The x-ray photon energy from the germanium target is limited. Therefore γ-ray photons needs to have a minimum energy around 230 MeV to enable the Breit-Wheeler process. These high energy photons are produced by Bremsstrahlung from the LWFA beam and therefore have the typical spectral shape shown on Fig. 3.5. As a result, electrons with kinetic energies below 230 MeV do not contribute to γ-rays capable of Breit-Wheeler pair creation, however, they do contribute to the radiation background on detectors, which lowers the signal-to-noise ratio. In order to reduce the noise, only electrons above 230 MeV should be used for Bremsstrahlung. This is achieved with a magnetic chicane to spectrally filter the LWFA electron beam, which was designed within this work and is presented here.

3.5.1. Operation Principle

The spectral electron filter is composed of four dipole magnets and one aperture in the middle to block electrons as shown on Fig. 3.11. The first dipole B_1 disperses the electron beam, which is collimated by a second dipole B_2. Then a 10 mm air gap with two tungsten apertures follows to block electrons below and above a certain deviation. Combined with the energy dependent deviation of electrons, this method allows a spectral filtering. The aperture gap is followed by a second pair of dipoles B_3 and B_4 to redirect the dispersed electrons back to their original path.

Incident LWFA electron beams usually have a divergence around 1 mrad, which causes mono energetic sub beams to be only partially blocked or transmitted depending on the angle of individual electrons as illustrated on Fig. 3.12. This smooths the spectral cut of the transmitted electron beam, which can be quantified as a varying transmission efficiency for mono energetic sub beams. The spectral width of this cut further depends on the absolute energy. For example does the transmission efficiency of a 1 mrad divergence electron beam go from 0 to 100% between 800 MeV to 1400 MeV, corresponding to a width of 600 MeV, if the cut off is set to 1100 MeV. At lower energies, for example at 335 MeV, the cut ranges from 320 MeV to 350 MeV, corresponding to 30 MeV width. Higher energy settings generally have a smoother cut. This effect can be counteracted by increasing the deviation and thereby dispersion through either stronger or longer magnetic fields. For the campaign at Gemini, the overall length of the spectral electron filter was constrained to 21 cm with 5 cm per dipole and 1 cm for the central aperture. With the smallest possible dipole gap of 3.3 mm, a magnetic field strength of 1 T was achieved.

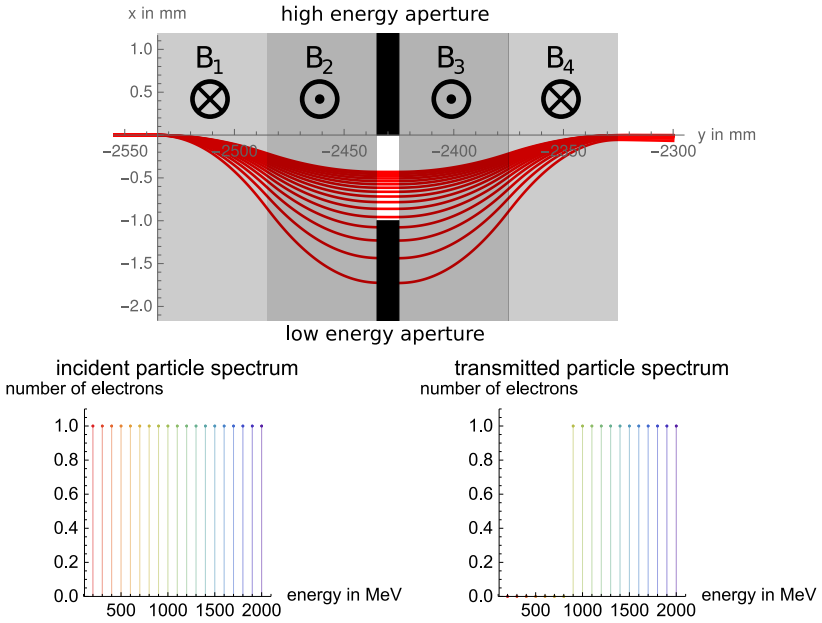

Figure 3.11.: Operation principle of the spectral electron filter. Two alternating magnetic fields disperse and collimate the electron beam, which is partially blocked by a variable aperture. A mirrored magnetic field guides the filtered electron beam back to the original trajectory.

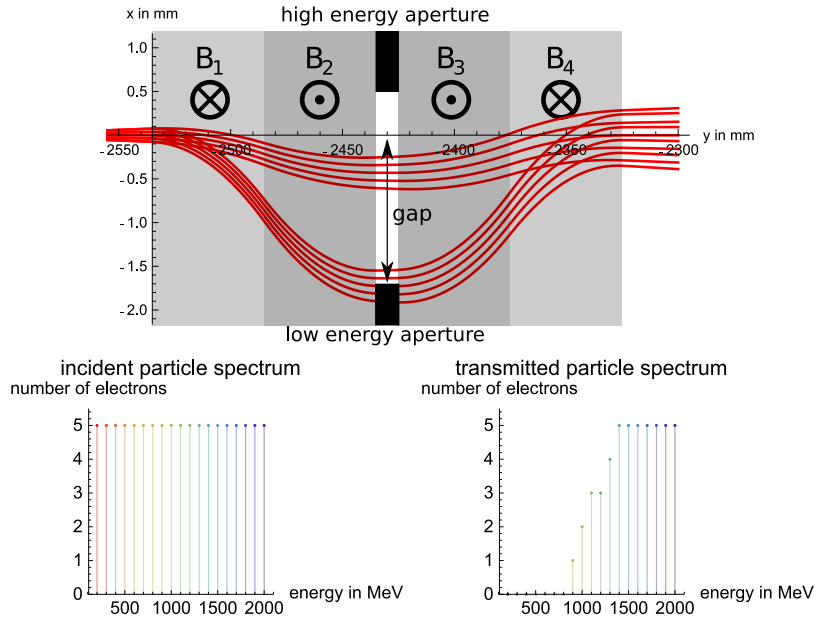

Figure 3.12.: LWFA beams have a typical divergence around 1 mrad, which causes the spectral cut to be smoothed, in this example between 800 and 1400 MeV.

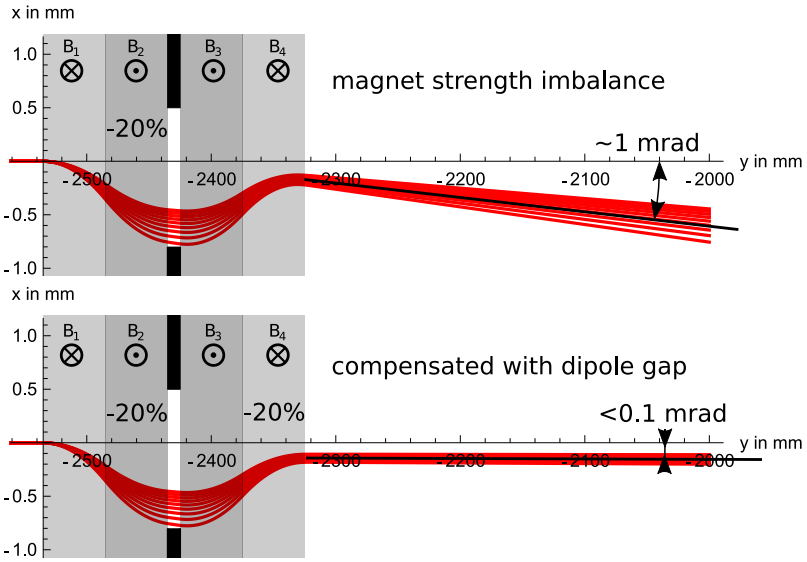

Figure 3.13.: Two scenarios showing a beam pointing offset induced by changes in the magnetic field strength and a compensated solution by adjusting the gaps of the remaining dipoles.

If the spectral electron filter is used for electron beam pointing sensitive applications, manufacturing errors of the magnets or other components need to be considered, because they change the angle under which the transmitted LWFA beam leaves the chicane. An example is shown on Fig. 3.14, where the dipole B_2 has a 20% lower field strength. This causes the beam to pick up too much downwards deviation and the pointing angle at exit is changed from 0 to 1 mrad. Additionally, this angle is energy depended and causes the beam to disperse. The Breit-Wheeler setup is generally sensitive to pointing variations in the milliradian range due to the limited apertures of beam line components and detectors after the interaction region, so the chicane must compensate for such variations. This was achieved by designing all four dipoles to be independent with a variable gap to allow field strength corrections. The example case on Fig. 3.14 with a 20% weaker B_2 can be compensated with a larger gap in B_4 until the field is decreased accordingly. The beam still has an overall offset in beam height, which can be balanced out by adjusting B_1 and B_3 by 20% as well. As a result, control over the dipole gaps does not only allow compensation of manufacturing impurities, it also provides active control over beam height and pointing offset in magnet dispersion direction.

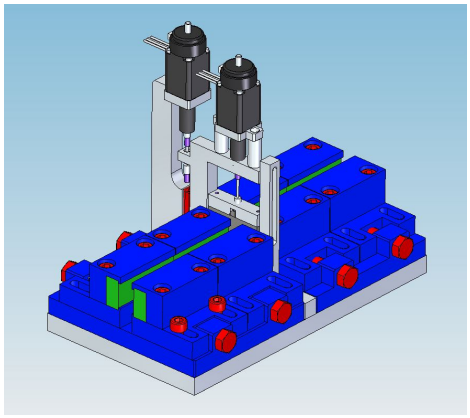

Figure 3.14.: A 3D CAD drawing of the spectral electron filter with magnets (green), magnetic steel (blue) and non magnetic screws (red). This figure is provided with courtesy of Mark Harman from STFC.

Mechanical Design

The mechanical realisation of the spectral electron filter is shown on Fig. 3.13. All four dipoles were manufactured identical with the NdFeB blocks being monolithic and of grade N52, which corresponds to around 1.45 T remanent magnetisation. Due to the required high vacuum compatibility and field homogeneity, the yoke was shaped to function as a clamp for the NdFeB blocks, avoiding glue and screw holes. Each pole is mounted to a base plate with two screws guided in elongated holes to allow movement in the horizontal direction. Control over the gap width is granted by a pair of threaded rods per dipole to adjust each magnet independently. The aperture is composed of two 9 mm thick pieces of tungsten, leaving 0.5 mm on each side as wiggle room. The upper aperture is motorised to be driven against the lower to adjust the slit width. A second motor drives the whole aperture assembly to adjust the slit position.

3.5.2. Measured Performance

The performance of the spectral electron filter was measured with the setup shown on Fig. 3.15. To allow tracking of the electron beam properties after the Breit-Wheeler interaction point, two scintillation screens were inserted into the beam line, one in front of the separator magnet (which is part of the analyser system and explained in the next section) and a second one behind to measure pointing, divergence and spectral shape. For this measurement, the primary electron spectrometer magnet that deviates electrons and positrons from the interaction region in Breit-Wheeler configuration needs to be moved from axis to allow the LWFA beam to pass. Due to

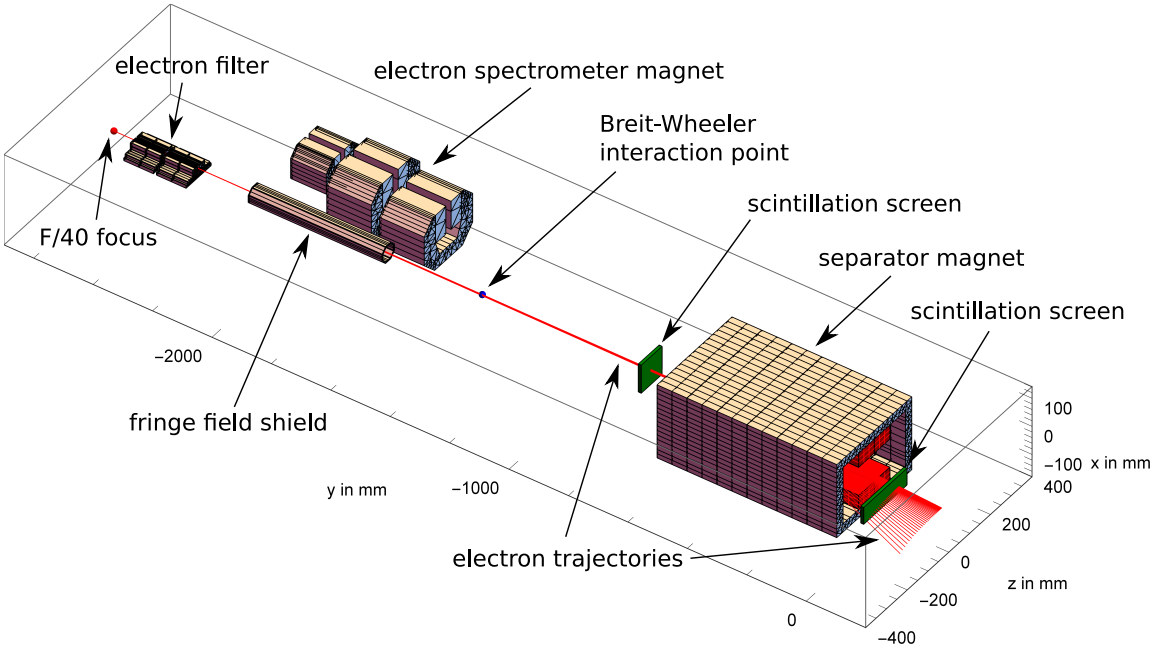

Figure 3.15.: Overview of the components used to measure the spectral electron filter performance. The primary electron spectrometer magnet is moved away from beam axis and a steel tube is used to shield the residual field. The beam properties are measured with two scintillation screens in front of and behind the separator magnet.

spatial constrains, it could only be moved by a certain distance, at which the residual fringe fields on axis were still too strong for a good measurement, so they needed to be shielded. This was done with a hollow ferromagnetic tube around beam axis, which is discussed in more detail in the next section that presents the analyser magnet system.

First measurements with the electron filter showed the expected energy dependent cut in the spectrum, presented on Fig. 3.16. The cut is under an angle relative to the energy axis due to the electron beam divergence. If the electron filter would be mounted upside down, the cut would be mirrored with respect to the energy axis. The whole assembly was simulated with Radia [72, 73] and the electron trajectories were calculated to estimate the width of the spectral cut. The results were in good agreement with the measurements as shown on Fig. 3.16 (right). In this configuration, the filter aperture was 2.6 mm below beam axis. A scan with increasing aperture opening is shown on Fig. 3.17. Each image is averaged over 5 to 10 shots, so the angular distribution includes pointing fluctuations. The spectral shapes are shown on Fig. 3.17 (right), where the charge was normalised with respect to the unfiltered beam to show that no charge is lost in the high energy tail. The beam profiles on Fig. 3.17 are bend towards negative divergences for low energies. This effect can have multiple

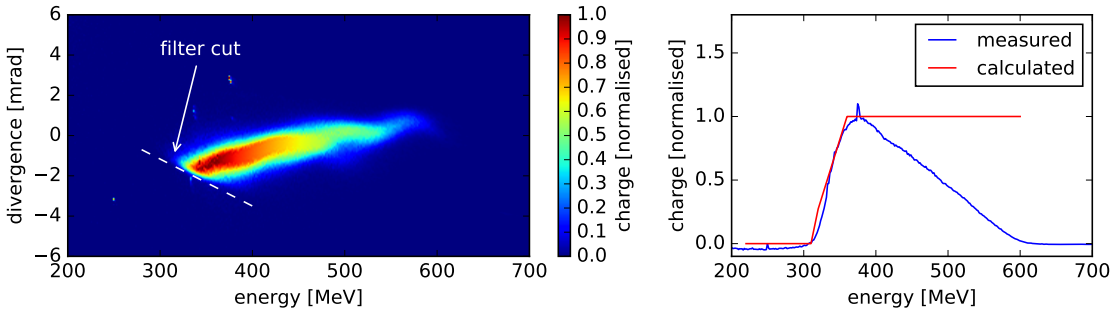

Figure 3.16.: Left: An example LWFA spectrum with the electron filter inserted to block charge below 350 MeV. The cut is angled due to electron divergence, which also causes the transmission profile to be smoothed from 320 MeV to 350 MeV. Right: The measured width of the spectral cut (integrated along divergence axis) is compared with Radia calculations and shows good agreement.

reasons, one of which being a lower magnetic field strength in one of the segments due to manufacturing impurities or incorrectly adjusted gaps in the individual dipoles of the filter chicane. Another reason could be an inaccurate alignment, where the electron beam would have a changing distance to the poles within the chicane, inducing locally different field strengths and thereby causing an energy dependent pointing offset. As pointed out in section 3.5.1, the system was built to correct for that but the required changes were not made for this measurement due to schedule constrains.

Effectiveness regarding Breit-Wheeler Detection

The primary intent of the spectral electron filter chicane is a reduction of background radiation on the detectors to increase the signal-to-noise ratio. This was not directly measured on this campaign and can only be estimated based on the filtered electron spectrum. The desired filter configuration for Breit-Wheeler shots is to block electrons below 230 MeV. Because both the primary electron spectrometer as well as the separator magnet used as secondary spectrometer were not sensitive to electrons below 200 MeV, the reduction in charge could not be measured. A very approximate estimate based on spectral shapes of LWFA beams below 200 MeV at the JETI200 laser in Jena, a reduction of overall charge by a factor of 5 to 10 is expected. Due to the lower energy of those electrons, less radiation is produced per charge, which leads to a background reduction estimate by a factor 2 to 5. At Gemini, the additional distance between electron source and Breit-Wheeler interaction point due to the filter chicane decreases the pair yield, which counteracts the background reduction effect. A precise

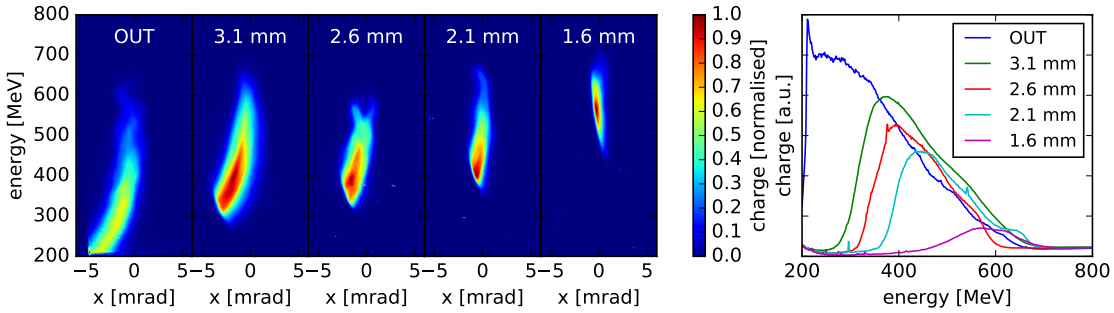

Figure 3.17.: Measured spectra with 4 filter aperture openings as well as without the chicane in the beam path. The gap is defined as depicted on Fig. 3.12. The graph on the right shows the spectra normalised to the beam charge in the OUT configuration to show that no charge is lost in the high energy tail.

quantification of the net effect of the spectral electron filter chicane on a Breit-Wheeler measurement therefore requires additional measurements and can not be determined from the available data taken on this campaign.

3.6. Analyser Magnet System

The detection of produced Breit-Wheeler pairs on this experiment is challenging due to the low cross-section and resulting pair creation probability in the order of 10^{-23} per incident photon. By using the novel x-ray target, around 10^{15} photons at keV energies participate in the reaction. Those photons can easily be distinguished from multi 100 MeV pairs, so they do not affect the signal-to-noise ratio significantly. The remaining 8 orders of magnitude need to be overcome with the second photon field, γ-ray photons above the threshold of 230 MeV. Such high energy photons produce a signature on scintillation detectors similar to Breit-Wheeler pairs and would cause a signal-to-noise ratio around 10^{-8} in a direct measurement. As discussed in section 2.3.2, signal-to-noise ratios around 10^{-1} need to be achieved to make a significant observation within the limitations of the setup at Gemini. To bridge the gap of 7 orders of magnitude, a system of permanent magnets was developed within this thesis specifically for this type of experiments at Astra Gemini. The operation principle to increase the signal-to-noise ratio focusses on two major steps. First, separate the Breit-Wheeler pairs from the γ-ray beam and second, focus them on shielded single particle detectors. A schematic of the overall layout is shown on Fig. 3.18.

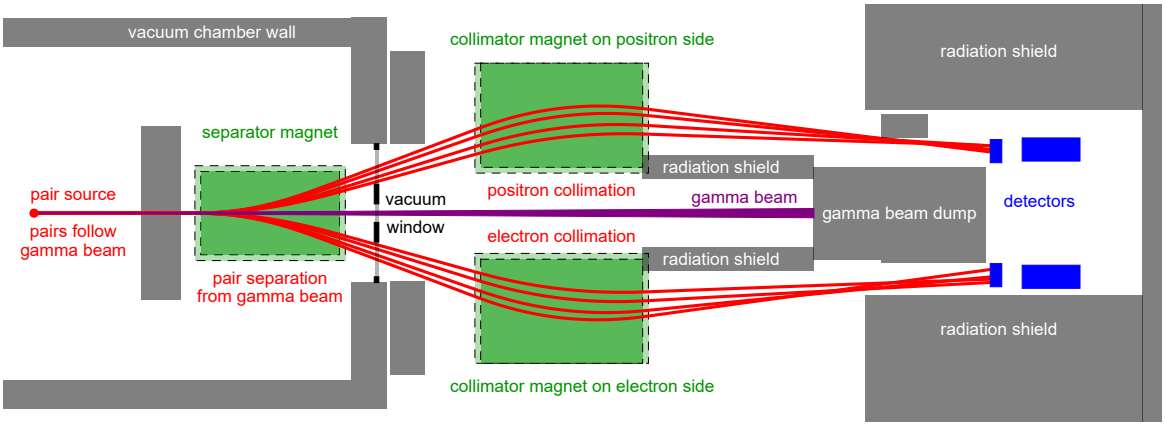

Figure 3.18.: The layout of the detection system. A first dipole magnet (green), called separator, separates the pairs (red) from the intense γ-ray beam (purple). A secondary pair of magnets (green), called collimators, focusses the pairs on single particle detectors (blue) that are shielded from the γ-beam.

Optimised Solution

The task of separating pairs from the γ-ray and focussing them on detectors has no clear solution. Numerous system variations with different advantages and drawbacks can be designed. One of such variants is a configuration that functions as a pair spectrometer by keeping the correlation of position to energy on detectors and is shown on Fig. 3.19. The shape of the NdFeB blocks (green) is optimised to form the required magnetic field distribution. As a result, the magnets require more engineering effort to manufacture compared to regular square blocks and are more expensive as well. A highly optimised solution like this is further typically more sensitive to setup variations. For those reasons, a compromise between performance, flexibility and manufacturing constrains was found specifically for Gemini.

3.6.1. Solution for Gemini

The Gemini solution for separator and collimator magnets utilised square blocks of NdFeB with grade N52 providing a remanent magnetisation around 1.45 T. A model of both magnets is shown on Fig. 3.20. The separator magnet has a 3 cm thick symmetric rectangular steel yoke that is magnetised up to 2.1 T. It is closed on both sides to provide similar deviations for electrons and positrons and has a gap of 10 cm to prevent the γ-ray beam from hitting the poles and creating Bethe-Heitler pairs. The NdFeB blocks are 15 cm wide and the overall length is 60 cm, over which the mean field strength is 0.6 T. The collimator magnets have a U-shaped steel yoke of

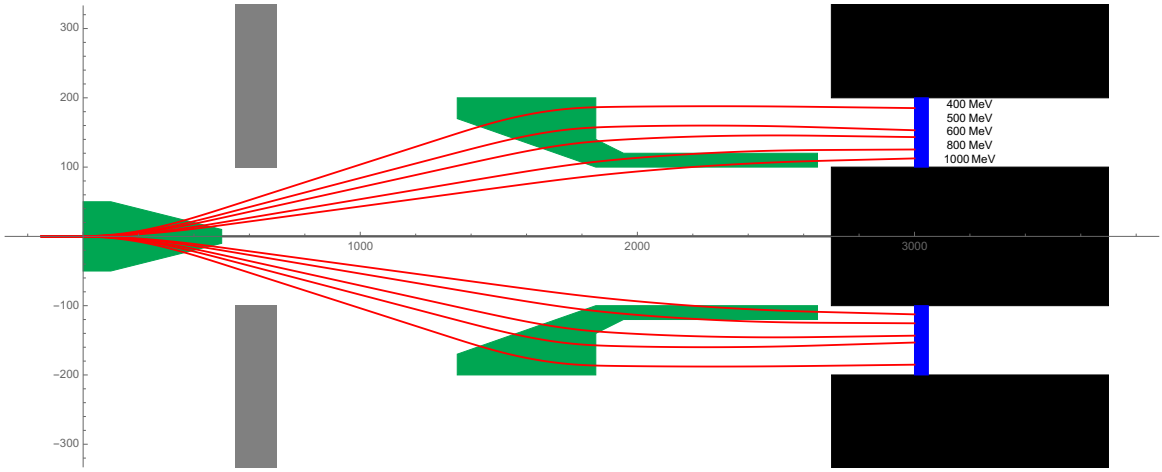

Figure 3.19.: A proposed optimised solution of the magnetic beam line to highlight the potential of this concept. Pair trajectories (red) with energies from 400 to 1000 MeV are collimated by the magnets (green) to correlate energy to impact location on the detectors (blue), allowing a spectroscopic analysis of the Breit-Wheeler pairs. The compromise for Gemini does not provide spectral resolution.

varying thickness up to a 10 cm at the base to save weight. They are open towards the beam axis to allow free passage of the γ-ray beam in the centre. Due to manufacturing constrains, the poles are composed of two 15 cm wide NdFeB segments with a 1 cm steel spacer in between instead of a single 30 cm wide piece. To even out the magnetic field distortion caused by the spacer, the poles are covered with 5 mm thick removable steel plates that were inserted for this experiment. Fig. 3.21 shows the plates as well as the smoothing effect on the field distribution compared to the monolithic solution. The collimator magnets have a gap of 9 cm with and 10 cm without plates, are 70 cm long and provide a mean field strength around 0.5 T. Both magnet types are composed of subsegments to make them modular and adjustable. The Gemini solution features 6 segments of 10 cm length for the separator and 14 segments of 5 cm length for each of the collimator magnets.

Positioning and Alignment

Each analyser magnet needs to be positioned with millimetre precision to ensure that Breit-Wheeler pairs hit the single particle detectors. This was done by placing them on large aluminium plates that rested on plastic plates to reduce friction on the support table. Combined with medium tension on load ropes from a crane, each magnet could be moved by slightly knocking on the aluminium plate, which glided on the plastic plate. This technique allowed millimetre precise positioning of the half tone magnets

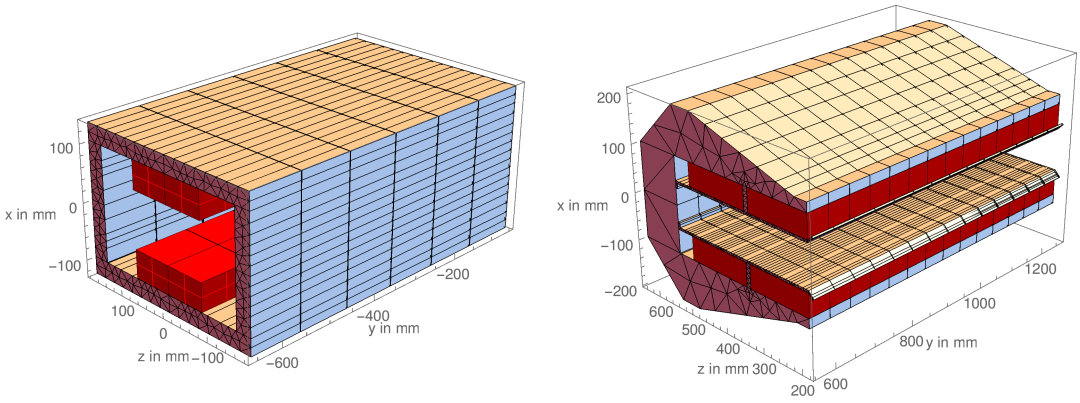

Figure 3.20.: The Gemini solution for separator (left) and collimator (right) magnets. The NdFeB blocks (red) are integrated into a steel yoke. The collimator magnets have plates on the poles to smooth the field distortion caused by the spacer.

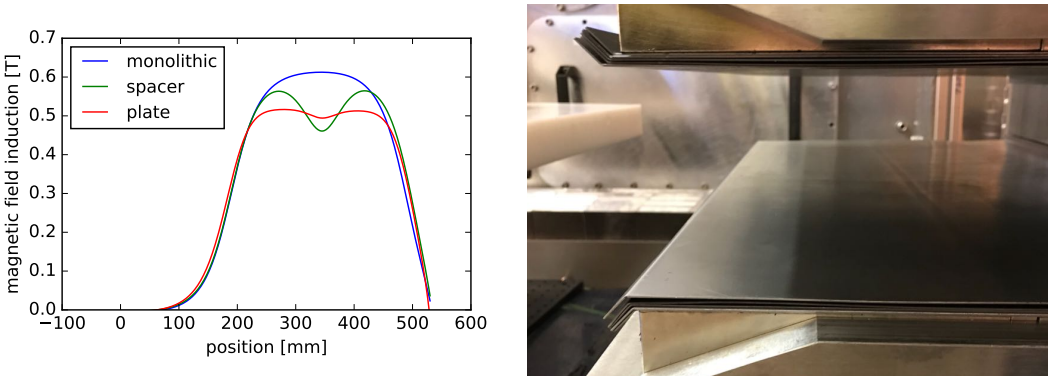

Figure 3.21.: Left: The collimator's lateral field distribution with (red, used on this experiment) and without (green) removable steel plates. The monolithic (blue) configuration additionally requires removal of the steel spacers. Right: Solution for Gemini with 5 plates at 1 mm thickness per pole.

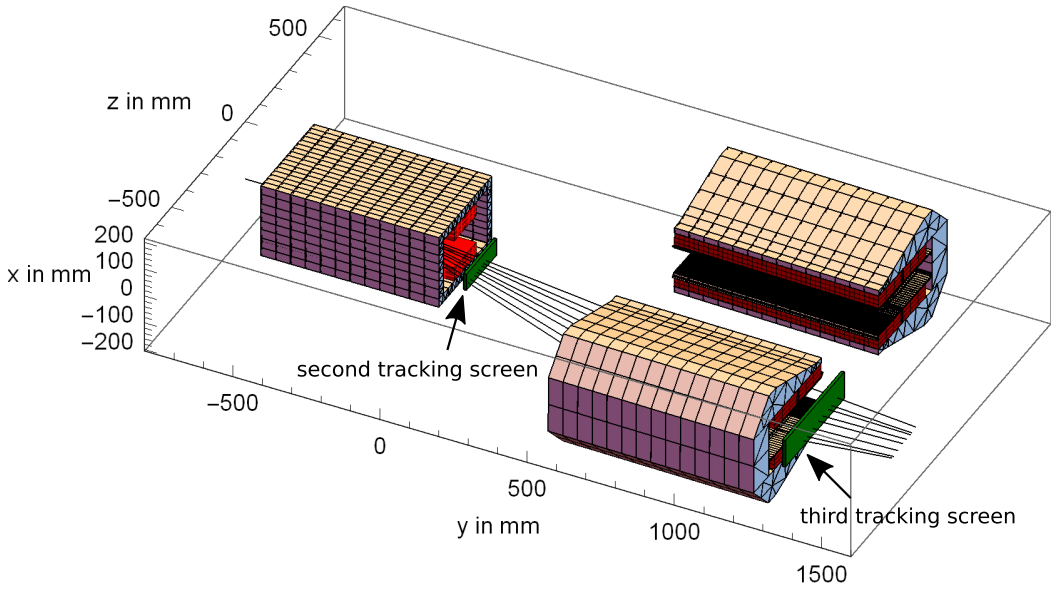

Figure 3.22.: Separator and collimator magnets with the second and third tracking screen to validate electron trajectories.

by hand. Each magnet rests on 5 adjustable posts to fine tune the height and to level them.

3.6.2. Beam Path Validation

The analyser magnet system is deployed for the first time on this experiment and needs to be validated, which was done by tracking of the LWFA beam through both analyser magnets to the single particle detector on the electron side. The spectral electron filter was used to select specific energies and allowed precise probing of individual trajectories. A third scintillation screen was inserted behind the collimator magnet to probe electron trajectories at three different points along the beam line shown on Fig. 3.22. The remaining setup is similar to the filter chicane measurement shown on Fig. 3.15 including the fringe field shield for the primary spectrometer magnet. This shield is essential because the fringe fields would deviate the electrons over the propagation distance of more than 5 metres by more than 5 cm, causing them to hit the collimator magnet poles before reaching the third tracking screen or single particle detectors. Due to its importance, the fringe field shield will be presented in this section before presenting the beam path validation of the analyser magnets.

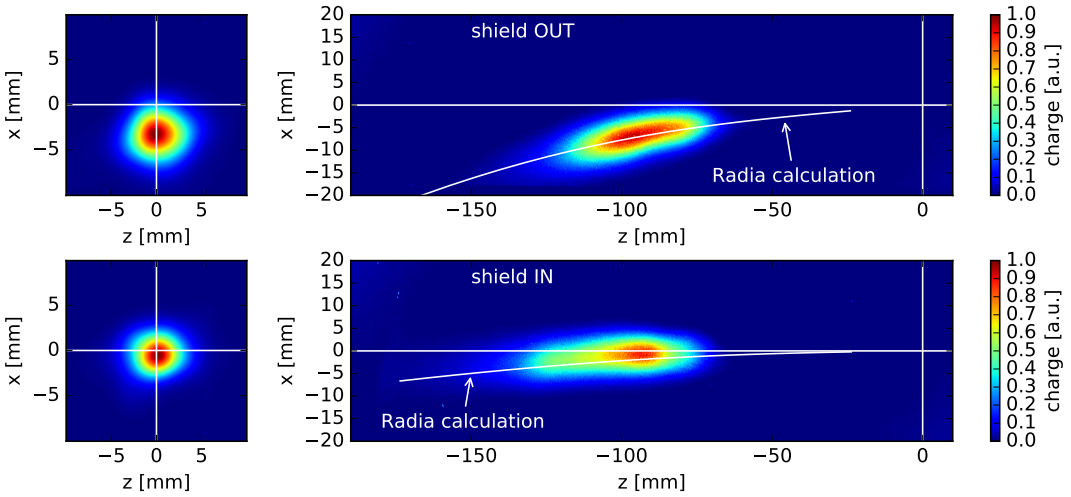

Figure 3.23.: The LWFA beam on the first (left) and second (right) tracking screen, each without (top) and with (bottom) the magnetic shield. The white line indicates the position of electrons with zero divergence calculated with Radia to compare simulations with measurements.

Fringe Field Shielding

In order to track LWFA electrons through the analyser magnet system, the fringe fields of the primary electron spectrometer magnet need to be shielded. This is done by inserting a ferromagnetic tube into the beam line around the electron axis next to the spectrometer magnet, which was shown on Fig. 3.15. The effect on the electron beam was measured with and without the shielding on the first and second tracking screen, where the first screen functions as pointing and divergence diagnostic and the second screen as spectrometer. The results are shown on Fig. 3.23. All images are averaged over 30 data shots, charge normalised and plotted in the spatial domain because the position of the electron trajectories are of interest for this tracking measurement rather than divergence or energy measurements.

The spatial distribution of LWFA electrons on the second screen without the shielding on Fig. 3.23 shows the downwards deviation caused by the primary spectrometer magnet. A similar effect can be seen on the first profile screen, where the centre of the distribution is around 3 millimetres below the measured beam axis. When the magnetic shield, a 5 millimetre thick tube of ferromagnetic steel, is inserted, the deviation relative to beam axis is much less, however, a residual downwards curvature along the dispersion direction is still measurable. This has two reasons, the first of which being the fringe fields of the separator magnet that is used as an electron spectrometer in this configuration. When the electrons are deviated inside the separator

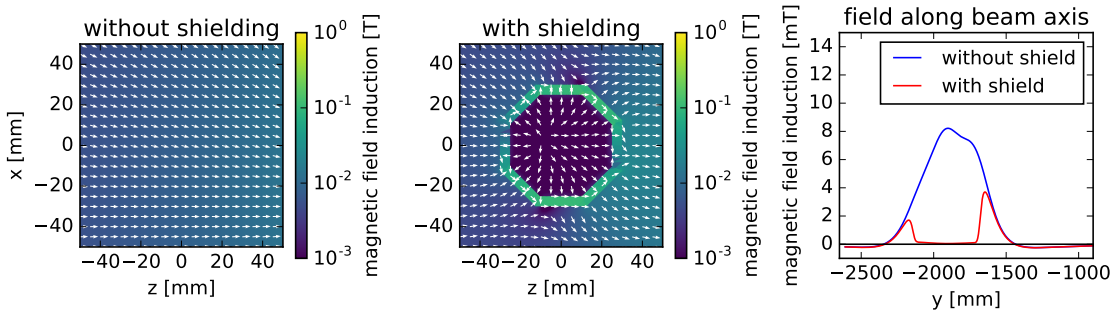

Figure 3.24.: The magnetic field induction with and without shielding around the beam axis next to the spectrometer magnet. The shielding tube was modelled with an octagonal cross section in Radia and guides the field lines around the beam axis, where the field strength is reduced from almost 10 mT to below 0.1 mT.

magnet, they reach the fringe field region next to the NdFeB blocks. This happens due to the combination of overall length, field strength and NdFeB block sizes of the separator magnet, which lets electrons at lower energies around 200 to 400 MeV propagate next to the primary field lines. There the fringe fields have a significant z component, which causes a downwards deviation. This effect is more pronounced for lower energies down to 200 MeV. Electrons beyond that are deviated far enough to impact the steel yoke and do not exit the separator magnet. The second reason for the residual downwards motion is due to the limited extent of the shielding tube, which was not sufficient to shield the full spectrometer magnet. Fig. 3.24 (right) shows the magnetic field induction along the beam axis next to the spectrometer magnet with and without the shielding, where the insufficient extent is visible in form of peaks in front of and behind the shielded region. The left and centre images on Fig. 3.24 show the transverse structure of the fringe field as well as the effect of the shielding tube, which is modelled in Radia with an octagonal cross section. The ferromagnetic steel is magnetised and guides the field lines around the beam axis, reducing the strength in the centre from several millitesla to well below one millitesla and thereby to levels that are negligible for this measurement. The calculated deviations of electrons at zero divergence with and without the shielding are drawn as overlays into the measured data on Fig. 3.23 to show the agreement between simulations and experiment.

LWFA Beam Tracking

The fringe field shield and electron filter chicane both proved to work properly, which enables the tracking of LWFA electrons through the analyser magnet system. The

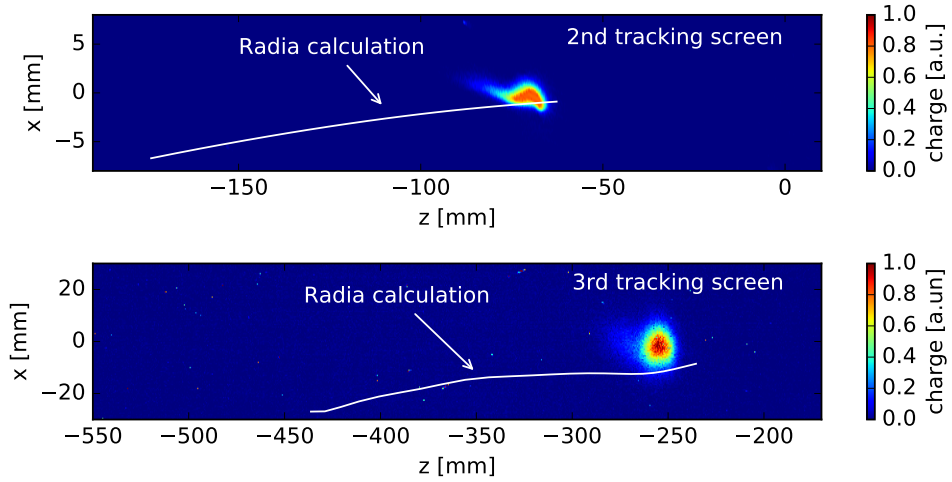

Figure 3.25.: The signal distribution on the 2nd and 3rd tracking screen. This shot was filtered with the spectral electron filter to create a low bandwidth feature that is easily identifiable on both screens. The white line indicates the Radia calculation for comparison. The selected electron energy on this example is 500 MeV.

major aim of this is to show that the numerical modelling of the magnets in Radia is sufficiently accurate to trust the simulated trajectories and impact locations of Breit-Wheeler pairs on the single particle detectors. This was done by comparing simulated and measured electron trajectories and especially the impact points on the third tracking screen behind the collimator magnet. With the filter chicane, quasi mono energetic sub beams can be selected. An example shot is shown on Fig. 3.25 together with calculated trajectories to check for overlap. By iterating over the spectral range with the filter chicane, this overlap can be measured for different electron energies.

A comparison of the simulated and measured positions on Fig. 3.25 shows a clear difference, for which there are two main reasons. These are the limited accuracy of position measurements of all components in the laboratory and the limited numerical precision of the simulation. The electron propagation needs to be calculated for the spectral electron filter, the primary spectrometer magnet including shielding, the separator and the two collimator magnets. All components need to be placed in Radia at their measured positions, which is subject to errors. Further, not all magnetic properties of the devices are known and calculating the field vectors close to magnetised surfaces with high precision is a computationally demanding task, especially because Radia solves magnetic objects with an interaction matrix that saves computation time but needs lots of memory per kernel. This sets an upper limit for the numerically

achievable precision by the utilised machine with 256 GB of memory. A particular challenging part is the magnetic plate on the collimator poles together with the metal spacer, which might be the driving factor for the observed discrepancy as the trajectories are close to this specific region. Additionally, the plates are realised as a stack of five 1 mm thick shims with the top one being bend by the field lines. This induces an additional field disturbance and was not modelled in Radia but might be one cause for the difference between the observed and calculated trajectories.

Overall, the prediction of electron impact points on the 3rd tracking screen deviates from the measurement by around 5 mm. On the single particle detectors the difference is expected to be 10 mm due to the longer drift space. This deviation between the calculated and measured trajectories of electrons through permanent magnets is relatively high, however for the Breit-Wheeler measurement it is sufficient to ensure that a large fraction of the Breit-Wheeler pairs hits the 75 mm by 100 mm large detectors.

Positron Trajectories

The positron side could not be tracked with scintillation screens like the electron side due to the lack of a sufficiently intense positron beam, however the electron tracking showed an accuracy of the Radia calculations of around 10 mm, which is assumed for the positron side as well. Additionally, a PTFE target was inserted into the beam close to the Breit-Wheeler interaction point to create a strong positron signal, which can easily be measured with the positron side single particle detector. To ensure that the measured signal on the SPD originates from PTFE positrons and not from scattered radiation, a part of the SPD surface is blocked for positrons. If the PTFE target increases signal in the domain open for positrons but not in the blocked region, one can be sure that positrons reach the single particle detectors, which was the case. If the amount of positrons produced by the PTFE target and the transmission efficiency of the analyser magnet system is known, this measurement can also be used as a single particle detector calibration. This was done and is described in the next section.

3.7. Single Particle Detectors

The single particle detectors need to detect the pairs produced through the Breit-Wheeler process. Estimates of the pair yield in advance of the experiment indicated that a single digit number of pairs per shot is expected. In order to detect this low signal, a system that can register single particles with a high confidence was

Figure 3.26.: A photograph of the 15 by 20 CsI(Tl) crystal matrix used in the SPD. The individual crystals are unique and have reflective titanium dioxide coatings of varying thickness to avoid optical crosstalk, which makes them appear to have different levels of opacity.

needed. This was achieved by combining an array of caesium iodide crystals with a very sensitive CCD. The CsI crystals are doped with thallium to increase the particle energy to scintillation light conversion efficiency. Paired with a 4Picos camera from Stanford Computer Optics, which achieves single photon sensitivity, the system is able to detect single positrons and is called the single particle detector (SPD).

The assembly is composed of a 15 by 20 crystal matrix shown on Fig. 3.26, each with a coating of titanium dioxide to avoid optical cross talk between neighbours. The surface pointing towards the camera is polished. An aluminium frame with open front and rear apertures holds the stack in place without obscuring incident pairs or blocking emitted scintillation light. The CsI array and 4Picos camera are mounted on a base plate and placed inside a cavity in the shielding of Geminis target area rear wall shown on Fig. 3.18, called the letterbox. This provides a low radiation background environment. To increase the shielding further, the letterbox was filled up with lead bricks and covered with light tight blankets.

The 4Picos camera achieves single photon sensitivity through a multi-channel-plate (MCP) that amplifies photo electrons with a high voltage. The optimal settings were 1600 V to 1700 V MCP gain, which corresponds to a photo electron multiplication factor of up to 10^6. During the amplification process, electrons trigger avalanches that are broadened by space charge effects and hit a scintillator that is coupled to a CCD. As a result, single photons appear as a broad distribution over 5 to 10 pixels on the camera, which is shown on Fig. 3.27. When a high energy particle hits the crystals, which will be called an event, energy is deposited in the lattice and partially emitted as scintillation light. Compared to the average background, which is a few

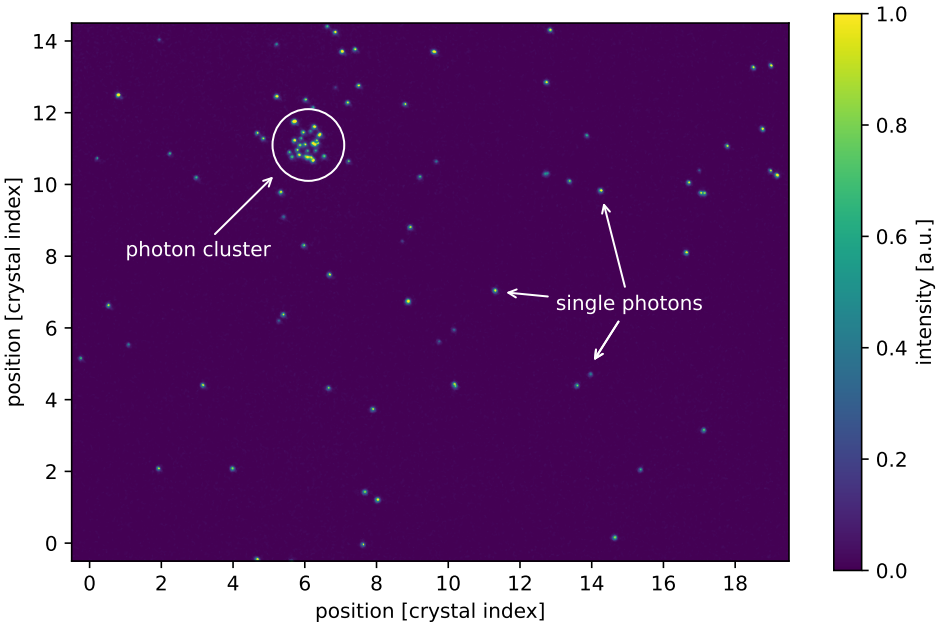

Figure 3.27.: A typical SPD image. The small dots are single photons intensified and broadened by the MCP. High energy particles appear as localised photon clusters.

photons distributed equally over the full image, a particle cascade will manifest as a localised cluster of photons. Such an event can be seen on Fig. 3.27. This allows single particle detection and works with high confidence as long as multiple particles do not spatially overlap and the background is sufficiently low. A single Breit-Wheeler class (few 100 MeV) positron event is typically composed of around 10 to 40 detected scintillation photons with this setup. The scattering process inside the crystals can be modelled and together with an imaging system calibration, the event energy can be determined from the number of scintillation photons associated with this event. However, this approach has an uncertainty due the stochastic nature of the process that is larger than the overall acceptance bandwidth of the analyser magnet system. Instead, two alternative and independent approaches to quantify the positron yield were chosen. The first method is based on a direct calibration of the SPD response to incident high energy positrons with a PTFE target in a calorimetric approach, which is presented in the following section 3.7.1. The second method identifies individual events on the SPD by searching for photon clusters, which is presented in section 3.7.2.

3.7.1. Detector Calibration and Positron Yield Calculation

The single particle detector measures single particles, specifically multi 100 MeV electrons and positrons from Breit-Wheeler pair formation. They hit the crystals and deposit energy, which is subsequently emitted as scintillation light. This is collected by a lens, intensified by the MCP and recorded on a CCD. The kinetic energy of incident particles correlates to the signal magnitude, but for the setup constrained spectral range from 220 MeV to 380 MeV, this difference is small compared to stochastic fluctuations of the deposited energy, so it is assumed to be constant for all pairs. This limits the detection capability to the absolute number of events rather than a pair spectrum. If the detector response to a certain number of positrons or energy is known, the pair yield can be calculated. This calibration was done with a 1 mm thick PTFE target in the beam. The idea of this calibration is to create an know positron signal on the SPD that can be directly correlated to the detector response. The PTFE target was inserted into the beam line close to the Breit-Wheeler interaction point, where it is hit by the γ-ray beam to produce electron positron pairs via the Bethe-Heitler process. The resulting pair population has a different spectral and angular distribution compared to pairs from the Breit-Wheeler process, but they propagate down the beam line through the analyser magnet system, around the shielding arrangement and on the detectors, so they undergo the same filter process as Breit-Wheeler pairs do. As a result, Bethe-Heitler pairs from the PTFE target that hit the detector have similar properties to Breit-Wheeler pairs, so the PTFE target essentially simulates a very strong Breit-Wheeler signal on the detectors. An advantage of this calibration method is that it can be done on the full Breit-Wheeler setup and does not require a separate setup, like a calibration with a known radioactive source for example. This approach increases the applicability to the obtained data and avoids additional sources of errors. In order to quantify the number of produced pairs from the PTFE target, the entire reaction chain from LWFA electrons over γ-ray bremsstrahlung, Bethe-Heitler pair production and propagation through the analyser system was simulated, which is described in the next paragraphs after normalising the 4Picos MCP gain.

MCP Gain Normalisation

The recorded SPD signal depends exponentially on the MCP gain voltage of the 4Picos camera. To make a calibration valid for multiple MCP settings, the camera response needs to be normalised. This was done by placing a known radioactive source in front of the crystals to deposit a defined amount of energy, which was then correlated to the

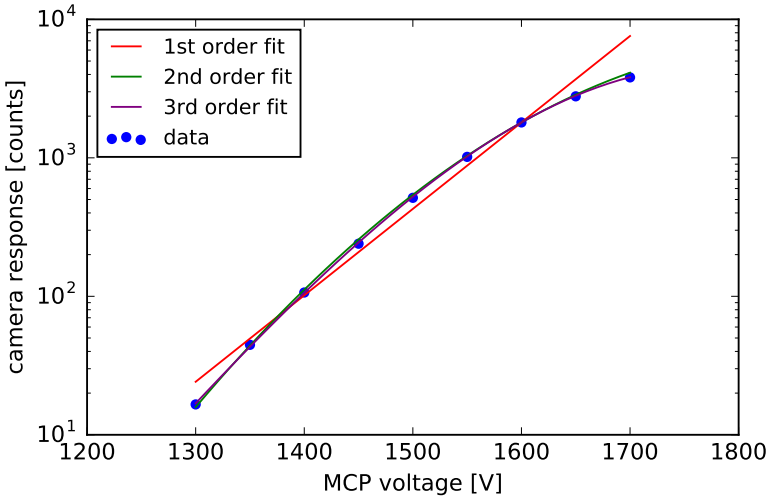

Figure 3.28.: The SPD response to a constant ^{22}Na source at different MCP voltages. To normalise the signal, a correction factor is applied with up to 3$^{\text{rd}}$ order polynomials in the exponent.

MCP gain dependent CCD response. The measured data is shown on Fig. 3.28. The source used for this normalisation was Sodium-22 (^{22}Na) with an activity of 1.6 MBq. The signal is exponential with the applied MCP gain voltage U and will be normalised to 1600 V by multiplication with a gain correction factor $A(U)$.

$$A(U) = 10^{f(1600-U)} \tag{3.1}$$

The exponent $f(1600 - U)$ was not further specified by the manufacturer, so polynomials up to 3$^{\text{rd}}$ order were tested. The fitted models are shown on Fig. 3.28. As a compromise between accuracy and complexity, the 2$^{\text{nd}}$ order solution was chosen, which has a relative deviation from the measured data around ±5% from 1300 V to 1700 V.

$$A(U) = 10^{a\cdot(1600V-U)^2+b\cdot(1600V-U)} \tag{3.2}$$

The fit parameters were calculated as $a = \frac{1}{122774}$ and $b = \frac{1}{226}$ by fitting the model to the recorded data as shown on Fig. 3.28.

PTFE Target Simulation

The first step to calculate the expected positron yield on detector from the PTFE target is to simulate the positron distribution that is generated by the PTFE target.

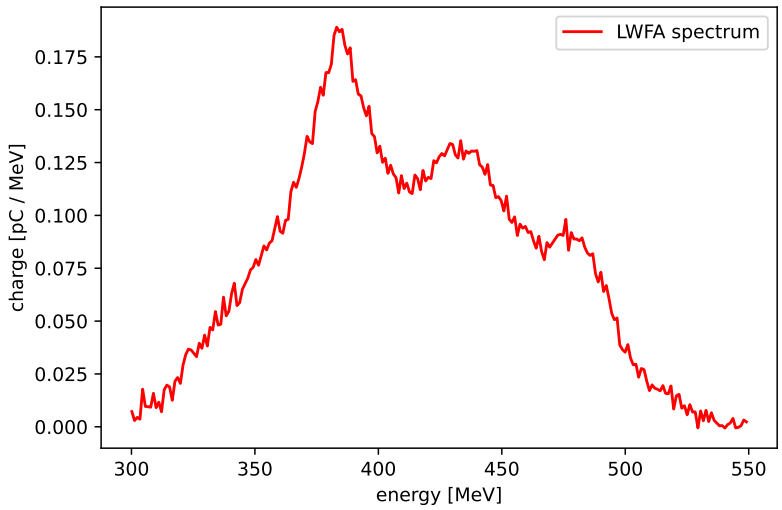

Figure 3.29.: The measured average electron beam spectrum during the PTFE calibration run containing 9.2 pC. This beam is used as input for the Geant4 simulation to calculate the positron signal on the single particle detectors.

This was done with Geant4 [74, 75, 76, 77], a software toolkit for the simulation of the passage of particles through matter. Those simulations were done with significant help of Felipe Salgado from Helmholtz-Institute Jena, but the evaluation of the obtained results was done by the author. The simulation input was the measured LWFA electron beam from the calibration shots, shown on Fig. 3.29. It had a divergence of 2.8 mrad FWHM and was propagated through the converter, collimator and magnet to obtain the γ-ray beam that would usually interact with the x-rays to produce Breit-Wheeler pairs. Instead of the x-ray field, the γ-ray beam hit the PTFE target, which was placed around 10 cm behind the Breit-Wheeler interaction point where pairs through the Bethe-Heitler process were produced. The generated positron population is shown on Fig. 3.30. These pairs propagate further through the analyser magnet system to the single particle detectors, however not all pairs are transmitted due to the limited transport efficiency of the system. To obtain the number of positrons that reach the detector, the particle trajectories through the analyser magnet system need to be calculated, which determines the transport efficiency. This is described in the following paragraph.

Analyser Magnet Tracking and the Radia Filter

The second step to calculate the positron yield on detector produced by the PTFE target is to evaluate which fraction of the produced positrons makes it all the way

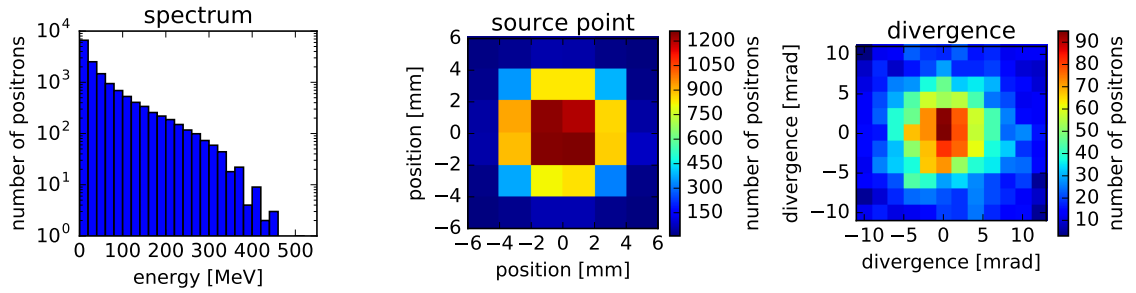

Figure 3.30.: The simulated positron population produced by the γ-ray beam inside the PTFE target. The γ-beam was generated by the measured LWFA beam shown on Fig. 3.29. The population contains $1.48 \cdot 10^4$ positrons in total.

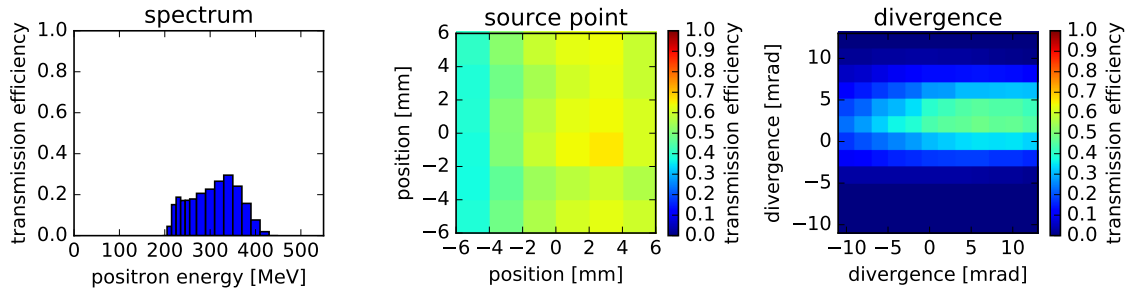

Figure 3.31.: Projections of the Radia phase space filter to the energy axis, source point and divergence planes. This filter is applied to the population on Fig. 3.30 to obtain Fig. 3.32.

through the analyser magnet system around the shielding to the detector as shown on Fig. 3.18. This calculation was done with Radia by performing a systematic positron phase space parameter scan for all energy, divergence and source point values that a positron can have. These trajectories are then evaluated based on the measured position of the lead shielding to sort out all trajectories that would have been blocked. This set of phase space coordinates can be used as a filter for any positron population to calculate the transmitted fraction and will be referred to as the Radia filter within this thesis. Because it is a 5 dimensional filter, it can only be visualised as projections to the individual planes, which was done on Fig. 3.31. This plot shows projections to the energy axis, source point and divergence planes. The efficiency is the fraction of trajectories that reach the detector based on the full range of considered initial positron properties. The Radia filter was applied to the simulated PTFE positron population shown on Fig. 3.30 to obtain the transmitted population, which is shown on Fig. 3.32.

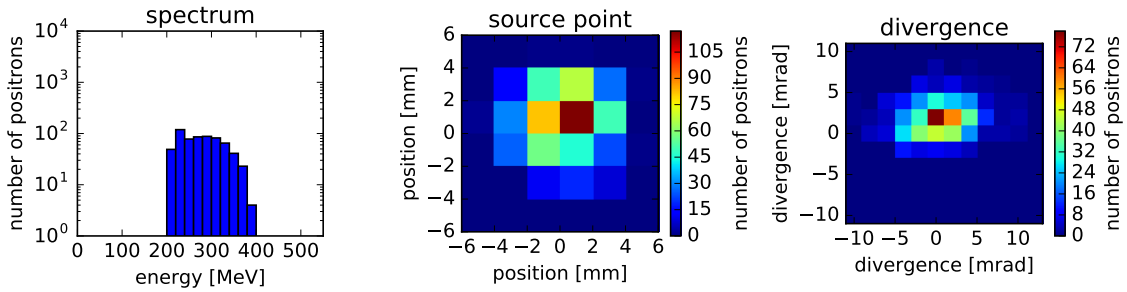

Figure 3.32.: The fraction of simulated PTFE positrons produced by the LWFA beam on Fig. 3.29 inside the PTFE target that were transmitted to the SPD. In total, 216 positrons reached the detector.

The source point distribution of the transmitted positrons on Fig. 3.32 is comparable but not equal to the source point distribution without the Radia filter on Fig. 3.30. The reason for this is that the Radia filter efficiency on Fig. 3.31 does only slightly change with varying source points because there are no apertures in the beam path that are in the range of the source size. However, there is a systematic increase in acceptance for source points towards the right on Fig. 3.31, which is important when considering pointing variations of the LWFA beam and therefore Breit-Wheeler pair source points.

The divergence distribution on Fig. 3.31 shows a clear favour for low values in the vertical direction with the most efficient value being 2 mrad. This can also be seen in the change of the divergence distribution from Fig. 3.30 to Fig. 3.32 where only very few positrons are transmitted above 5 mrad and below -2 mrad. This strong dependence on the divergence in vertical direction is caused by apertures along the beam line. The lower limit originates from lead shielding in front of the letter box and the upper limit is caused by the spatial extent of the SPD itself. The acceptance in the horizontal direction is much higher with a slight preference for right pointing, which agrees with the source point distribution.

The dominant influence on the transmission efficiency comes from the positron energy. As seen on Fig. 3.31, no positrons below 210 MeV and above 420 MeV reach the detector. The cause for the low energy limit is the separator magnet itself. Due to its combination of length, width and field strength, electrons and positrons on axis below 220 MeV collide with the yoke and do not leave the magnet. If incident particles have different source points or initial divergence, this limit can be shifted by up to 10 MeV, which is the reason why a few positrons at 210 MeV are transmitted and a rightwards pointing and divergence are generally more accepted by the system. The high energy

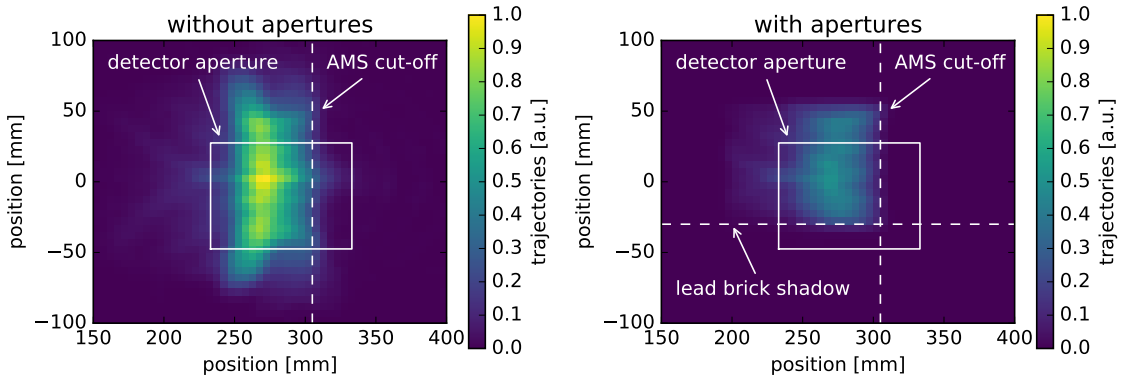

Figure 3.33.: Simulated positron impact point distribution on the SPD plane without (left) and with (right) apertures along the beam path.

limit is due to the extent of the vacuum exit window frame seen on Fig. 3.1, which does not reach closer than 122 mm to the beam axis and thus blocks positrons above 380 MeV. This energy cut off depends on source point and divergence too, allowing very few positrons with extreme pointing angles up to 420 MeV to pass.

Besides the information whether a positron hit the SPD, the Radia filter also provides the impact position for a given phase space coordinate on the detector plane. This is useful to determine the optimal position of the detector to maximise particle collection efficiency since the SPD is smaller than the area over which transmitted pairs are distributed after they propagate through the analyser magnet system. The distribution of trajectory end points with and without apertures along the beam line is shown on Fig. 3.33, where the detector aperture is highlighted by the white box. The dashed line indicates the analyser magnet system (AMS) cut-off, which is a virtual line that positrons can not pass no matter which energy, divergence and source point they have. This is a feature of the AMS due to the overall geometry of the system. This cut-off is intrinsic to this setup and is used as a spatial reference to overlap the measured with the simulated positron distribution. A major difference between the distributions with and without apertures on Fig. 3.33 is the overall lower yield, which is due to the spectral transmission efficiency caused by the vacuum exit window. Another important difference is a second cut-off line caused by lead bricks that shield the lower region of the SPD from incident positrons, which is used to determine the ratio of positron radiation to diffuse low energy background radiation.

Similar to the transformation of the PTFE positron population from Fig. 3.30 to Fig. 3.32 can the Radia filter be used to project the PTFE positrons onto the SPD plane. This projection is shown on Fig. 3.34 together with the measured signal on

PTFE data shots to show the overlap between simulation and measurement. The two distinct cut-off lines caused by the analyser magnet system and lead shielding are visible on both the simulated and measured distribution. The simulated distribution contains 216 positrons within the detector aperture. Since the generation of positrons in the PTFE target is a probabilistic process, the simulated value of 216 positrons has a statistical error. This error was quantified by performing three identical Geant4 simulations of the PTFE target, which yielded 216, 196 and 188 positrons on the detector. The mean value of those is 200, the standard deviation is 12 and the standard error of the mean is 7. All simulations were performed with the LWFA spectrum from Fig. 3.29 with a total charge of 9.2 pC.

Since the number of positrons from both the Bethe-Heitler as well as the Breit-Wheeler process depends on LWFA beam charge, spectral shape, pointing and divergence, the positron yield needs to be normalised to make different data sets comparable. This normalisation is done relative to the spectral shape shown on Fig. 3.29 with no pointing offset and a divergence of 2.8 mrad FWHM, which was the average shot during the calibration run. If these LWFA beam characteristics are unchanged, the positron yield is linear to the LWFA beam charge and can be normalised. This normalisation to *reference charge* is denoted as pC_r and implies the spectral shape on Fig. 3.29, zero pointing and a divergence of 2.8 mrad FWHM. Further does this method only cover positrons that are transmitted through the AMS with the associated properties specified on Fig. 3.32, which is denoted with the subscript *ams* to the unit positrons like $\mathrm{positrons}_{\mathrm{ams}}$. This clarifies that a quantity derived from the detector signal expressed in $\mathrm{positrons}_{\mathrm{ams}}$ refers to high energy Breit-Wheeler class positrons and not to positrons in general. There are also low energy positrons along with more low energy radiation measured on the detector, but those are excluded.

The positron yield from the PTFE target was produced with 9.2 pC_r through the AMS and is therefore $(21.7 \pm 0.8) \frac{\mathrm{positrons}_{\mathrm{ams}}}{\mathrm{pC}_r}$.

Measured PTFE Yield and Reference Charge Normalisation

From simulations presented in the previous section, the expected number of positrons on SPD with a 1 mm PTFE target in the beam is known to be $(21.7 \pm 0.8) \frac{\mathrm{positrons}_{\mathrm{ams}}}{\mathrm{pC}_r}$. These impact the detector in a confined spatial sector limited by the AMS cut-off on the right and the lead brick shadow on the bottom. The analysis of the positron yield is therefore only done with signal obtained within this *open* region specified on Fig. 3.35. The *shielded* region, also shown on Fig. 3.35, represents the remaining area and is used to evaluate the background radiation other than AMS positrons.

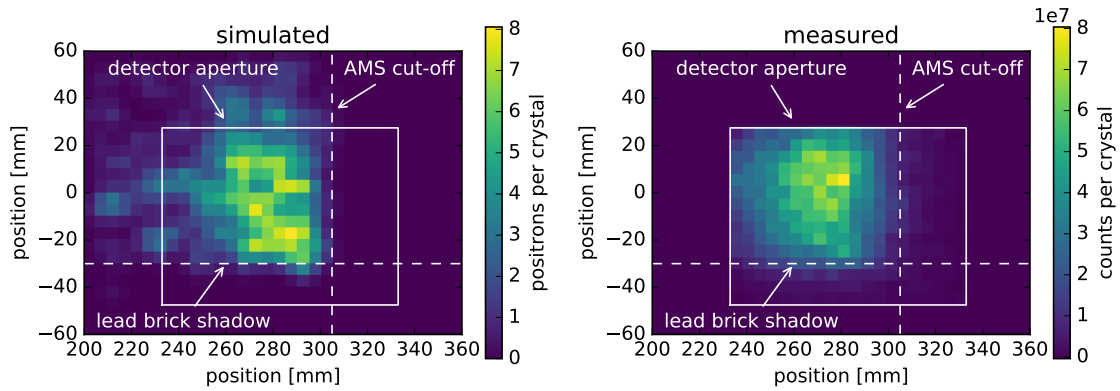

Figure 3.34.: Left: Simulated PTFE positron distribution on the SPD projected with the Radia filter. Right: The measured signal distribution on PTFE data shots. The pixel size is equal to the individual scintillator crystals. The measured yield is correlated to the simulated positron number as an SPD calibration.

To get an accurate SPD calibration, the associated amount of signal originating from the PTFE positrons needs to be isolated, which was done by correcting the 4Picos images for camera induced artefacts such as dead and hot pixels, a linear CCD offset and the MCP gain. The field of view is limited to the crystal area and a projective transform removed linear transformations induced by the imaging system. Non-linear transformations like pincushion distortions are negligible. The 7 PTFE shots (GSN 198879 to 198886 except 198882) where integrated over the open region to get an average yield of $(8.44 \pm 0.69) \cdot 10^8\,\mathrm{counts}_n$. The unit counts subscripted with n refers to normalised counts after image processing rather than raw CCD counts. The error is the standard error of the mean and originates to a large degree from shot-to-shot fluctuations of LWFA beam properties and by extent the γ-ray beam. To compensate for these as well as to identify a potential systematic offset in γ-ray beam intensity during this run, the measured SPD signal needs to be normalised to reference LWFA charge the same way as the simulations were. The issue here is that the LWFA beam is scattered by the converter target to produce the γ-ray beam. This scattering process changes the electron beam properties to a degree that makes reconstruction of the incident LWFA beam impossible, so whenever a γ-ray beam is produced, the LWFA beam can not be measured on the same shot and vice versa. The approach to determine the LWFA beam charge with the converter inserted is to measure the total yield on the γ-ray profile diagnostic. As an approximation, the measured total γ-ray yield is assumed to be linear to the LWFA beam charge. This approximation is only valid for small variations of the LWFA beam spectral shape because higher

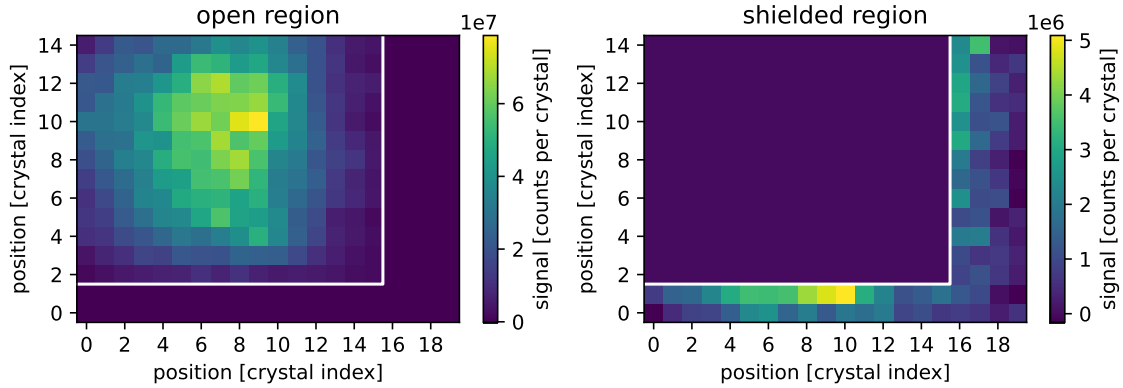

Figure 3.35.: The measured average PTFE signal on the SPD per shot. Left: The region open for positrons through the AMS. Right: The cut out shielded region that only measures diffuse background radiation.

energy electrons produce more γ-photons at higher energies. In general, the spectral shape of an electron beam can not be determined by measuring the bremsstrahlung γ-yield without knowing the total charge, however LWFA beams specifically show a correlation of total charge to maximum energy if they are produced with identical acceleration boundary conditions and with ionisation injection. During the acceleration process, electrons gain energy and more charge is injected over time. As long as this process can be maintained by the driving laser, electrons reach higher energies and more charge is injected. As a result, for constant acceleration parameters, high peak energy LWFA electron beams tend to have higher total charges. Based on this effect, a good approximation of LWFA beam charge and spectral shape by the measured γ-ray yield can be assumed by limiting the data to high γ-yield shots and discarding low yield shots. The threshold for 'high' γ-yield shots is thereby determined based on the measured data shown on Fig. 3.36 and has a value of $2 \cdot 10^7$ integrated counts on the γ-beam profile diagnostic. Below this value, a non-linear correlation between SPD and γ-profile yields can be observed, which is due to said tendency to lower electron energies on shots with low charge. Shots below this threshold are excluded from data evaluation.

The calibration of the γ-profile diagnostic was done by measuring LWFA beam and γ-yield in sequence and assuming a constant average performance for this set of shots. On all shots above the specified threshold, the average γ-profile yield was $(6.47 \pm 0.61) \cdot 10^7$ counts with 9% error margin. The error is the standard error of the mean. The average LWFA charge measured on shots without converter target was $(19.3 \pm 1.1)\,\mathrm{pC}_r$. This gives a γ-profile calibration of $(3.4 \pm 0.3) \cdot 10^6 \,\frac{\mathrm{counts}}{\mathrm{pC}_r}$.

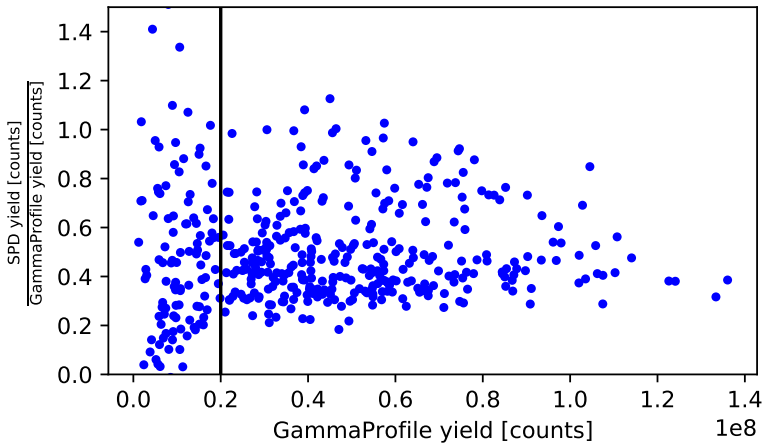

Figure 3.36.: The ratio of SPD to γ-profile yield plotted against the γ-profile yield. Some shots below the threshold of $2 \cdot 10^7$ counts show a linear dependency between normalised SPD yield and γ-profile yield.

With a calibration of the γ-profile diagnostic, the SPD yield can be normalised to reference LWFA charge on a single shot basis. The average value with the PTFE target is obtained as $(4.77 \pm 0.17) \cdot 10^7 \, \frac{\text{counts}_n}{\text{pC}_r}$. The relative error is brought down by this γ-profile normalisation from 8% to 1.4%, indicating the high degree of correlation between SPD yield and reference LWFA charge.

Corrections for Background Radiation

Up to this point, the SPD yield is corrected for imaging system induced errors and normalised to reference LWFA charge. In order to isolate the positron signal, background signal caused by scattered radiation needs to be subtracted. The magnitude of this background radiation is measured without any positron target in the beam line over 5 shots, which were GSN 198866 to 198870. After applying all image processing and reference charge normalisation techniques as described above, the average background signal in the open SPD region is found to be $(1.09 \pm 0.04) \cdot 10^6 \, \frac{\text{counts}_n}{\text{pC}_r}$. Subtracting this from the yield obtained with the PTFE target gives the background radiation corrected PTFE yield of $(4.66 \pm 0.17) \cdot 10^7 \, \frac{\text{counts}_n}{\text{pC}_r}$. From simulations it is known that the PTFE target induces $(21.7 \pm 0.8) \, \frac{\text{positrons}_{\text{ams}}}{\text{pC}_r}$, so the SPD calibration is obtained as $(2.15 \pm 0.03) \cdot 10^6 \, \frac{\text{counts}_n}{\text{positron}_{\text{ams}}}$. The two calibration values for SPD and γ-profile are summarised in Table 3.1 and are used to quantify the number of AMS positrons and the amount of reference LWFA charge on a single shot basis.

Table 3.1.: SPD and γ-profile calibration values.

physical property	diagnostic	calibration
reference LWFA charge	γ-profile	$(3.4 \pm 0.3) \cdot 10^6 \ \frac{\text{counts}}{\text{pC}_\text{r}}$
AMS positron yield	SPD	$(2.15 \pm 0.03) \cdot 10^6 \ \frac{\text{counts}_\text{n}}{\text{positron}_\text{ams}}$

3.7.2. Photon Cluster Identification

This section describes the second of two methods to determine the number of positrons on an SPD image by searching for clusters of scintillation photons. The reason why this method is used additionally to the calorimetric method presented in the previous section is the low yield of typical shots in Breit-Wheeler configuration, where the image integral is defined by single photons. An example shot is shown on Fig. 3.37 (a), which is a typical SPD image at an MCP gain of 1600 V so that photons are amplified to broad distributions. This image features a distinct photon cluster that is shown in a zoomed view on Fig. 3.37 (b). Every dot is a scintillation photon. There is a large variety in intensity and size between the individual photons which causes a growing uncertainty of the integral for images with low photon numbers. Another source of uncertainty is the sensitivity to CCD noise correction. The example image presented on Fig. 3.37 (a) has a count integral before CCD noise correction of $625 \cdot 10^6$ counts and after CCD noise correction of $7.5 \cdot 10^6$ counts, so the noise is 100 times the photon signal. The chip has approximately $1.4 \cdot 10^6$ pixels and the noise correction accuracy is limited to one count value per pixel, which causes a minimum error of the image integral of at least $1.4 \cdot 10^6$ counts, which is already 20% of the isolated photon integral. Yet another source of error is the fact that single photon hits can saturate the CCD at high MCP gain values above 1550 V, also affecting the integral of low yield shots significantly. For those reasons, integrating the SPD image and converting the signal into AMS positrons inferred from the PTFE calibration works well for shots with many photons like the PTFE data but it is increasingly inaccurate for low yield shots like typical Breit-Wheeler data shots. For such low yield shots, the second SPD evaluation method is developed, which is based on photon counting and subsequent cluster identification.

Evaluation Steps and Reliability

The first step of the algorithm is to identify single photons, which is shown on Fig. 3.37 (b) where identified photons are marked with red dots. This is done by searching for local peaks with maximum count values above a threshold based on the global pixel

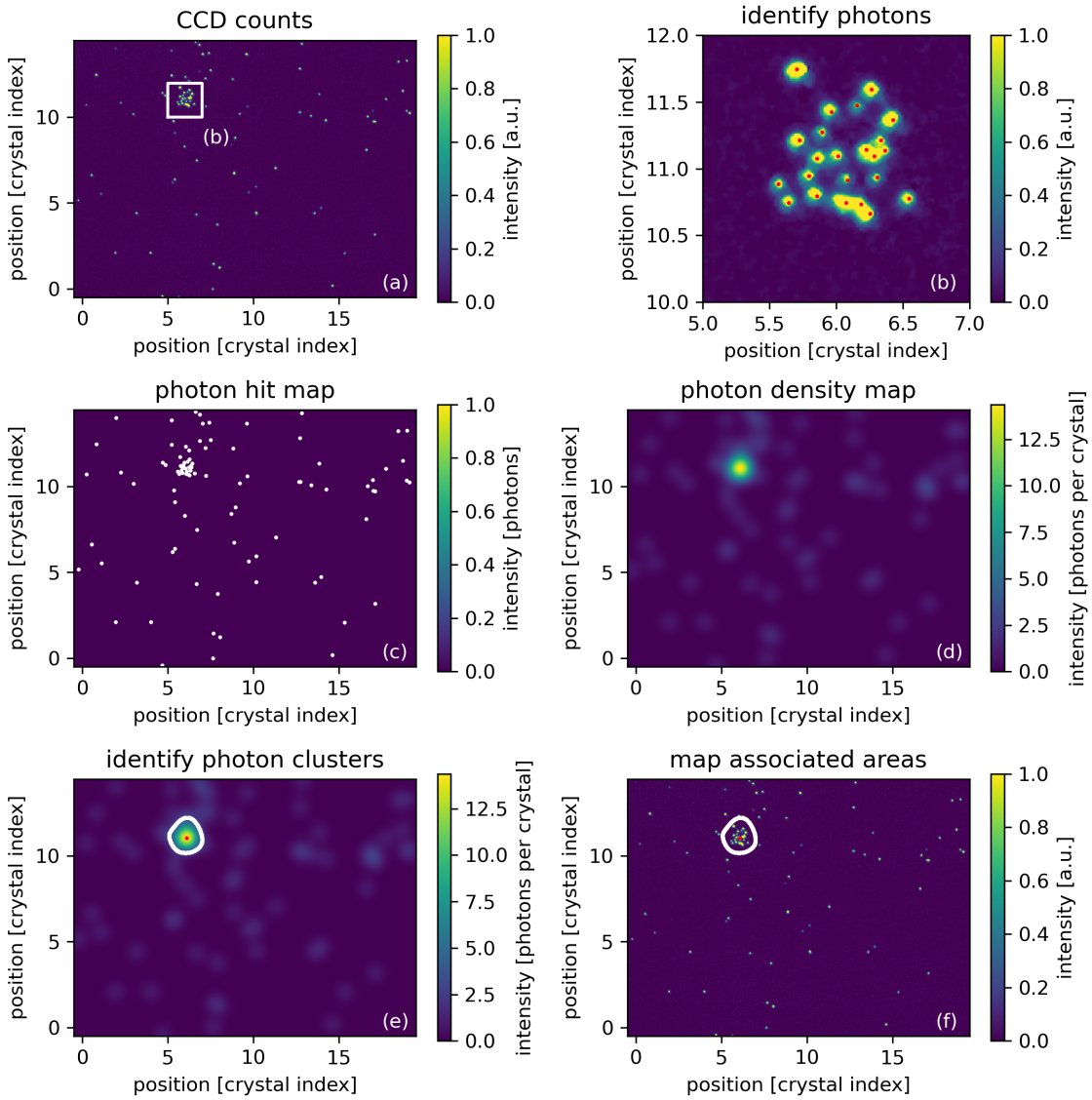

Figure 3.37.: The major steps to find photon clusters on SPD images. This example shot has one distinct photon cluster, also shown on Fig. 3.27. Photons are identified on the processed SPD image (a). (b) shows a zoomed view of the photon cluster with red markers where photons were found. These are used to create a photon hit map (c), which is smoothed to obtain a photon density map (d). There, local maxima are identified (e) and the associated area is mapped back to the original image (f).

distribution to avoid counting CCD noise as photons. The peak locations are used to create a photon hit map, shown on Fig. 3.37 (c). This photon hit map can be understood as the signal from the CsI crystals without ICCD effects, except quantum efficiency, since it only contains the logical information if a photon is there or not. This process is also very resistant to changing MCP gain settings, because photons are identified as photons regardless of their induced count signal. In a next step, the photon hit map is smoothed using a 2D Gaussian filter to create a photon density map, shown on Fig. 3.37 (d). The kernel has a width of one crystal or 5 mm, which is the intrinsic uncertainty of the measured photon source point. The obtained photon density map is then searched for local maxima, highlighted with a red dot on Fig. 3.37 (e). Maxima in the photon density distribution correspond to photon clusters, which are candidates for possible high energy events. The threshold for a classification of local photon density maxima as candidate events is calculated for each SPD image separately. First a constant offset of 2 photons per crystal is set, so that a local maximum needs to have at least 2 photons per crystal to be identified as a candidate event. This is to avoid counting single photons as candidate events on very low yield images with less than one photon per crystal. The threshold is further increased by the median photon density over all crystals to correct for a homogeneous photon background on each shot. The third component of the threshold is the standard deviation of the photon density over all crystals. This ensures that statistical fluctuations of the homogeneous photon background are not counted as candidate events as long as they are smaller that one standard deviation. This is, based on a normal distribution, true for 84% of all maxima. In combination, those three contributions to the threshold ensure that only maxima in excess of the photon background are identified as candidate events over a large range of total photon yields, done automatically for each shot individually.

The final step is the classification of candidate events as actual high energy particle events. This is done based on the individual photon cluster properties. For a classification as high energy particle, a candidate event photon cluster needs to have a spatial extent of at least 25 mm^2 or one crystal and a minimum total photon yield of the median plus one standard deviation over all crystals. This spatial constrain is motivated by the crystal size since a high energy event will never be smaller than one crystal, which sets the spatial resolution limit. The total photon yield limitation complements the minimum spatial extent and ensures that large but weak events are not counted as high energy particles.

The presented algorithm to identify high energy particle events on SPD images was tested on many shots and cross checked by hand. The event identification reliability

is not worse compared to a scientist performing the same task by hand. It was not possible to determine whether the algorithm is more reliable in this respect compared to a scientist due to the unavailability of defined test data. The final output of this evaluation method is a number of positrons for each SPD image, which is then further processed in a statistical analysis over many shots to evaluate collision and background data with respect to statistically significant differences. This second major part of the Breit-Wheeler data evaluation methodology is presented in section 3.7.3.

Limitations

As described in the previous paragraph, the photon cluster identification method is used on low yield shots due to its higher confidence in positron identification. An example for such shots is shown on Fig. 3.38 (a) and the deduced photon clusters are shown on Fig. 3.38 (b), where 3 candidate events were found of which 2 were classified as high energy events. For comparison, the calibration method inferred yield is 2.4 AMS positrons. Vice versa can intense shots like PTFE data only be evaluated with integration and calibration, because single photons spatially overlap and can not be distinguished. An example for such shots is shown on Fig. 3.38 (e) where so many photons hit the MCP that they overlap and a photon cluster identification is not possible, shown on Fig. 3.38 (f). The calibration inferred yield on this shot is 464 AMS positrons. Between these two extreme regimes lies an intermediate range of shots that are composed of separated photons, but the density is too high to identify specific clusters. Unfortunately, the majority of Breit-Wheeler data shots can be categorised in this regime. A typical example for this type of shots is shown on Fig. 3.38 (c). The photon cluster identification result is shown on Fig. 3.38 (d), where 10 candidate events were found of which 5 were classified as high energy events. The calibration inferred yield is 9.2 AMS positrons. For this class of images, it is also difficult for a scientist to determine the exact number of photon clusters or high energy events.

Despite the mentioned increased sensitivity of low yield shots to CCD noise correction for the calibration based method, the agreement between both methods for low yield shots is very good. An explanation for this is that with very few photons, the CCD noise can be determined very accurately, which is done with a 2D linear fit, so that it does not affect the calibration inferred AMS positron yield significantly. On average Breit-Wheeler shots, the photon background is so high that the signal magnitude of high energy events is not significantly above random fluctuations of the photon background so that photon clusters can not be clearly identified.

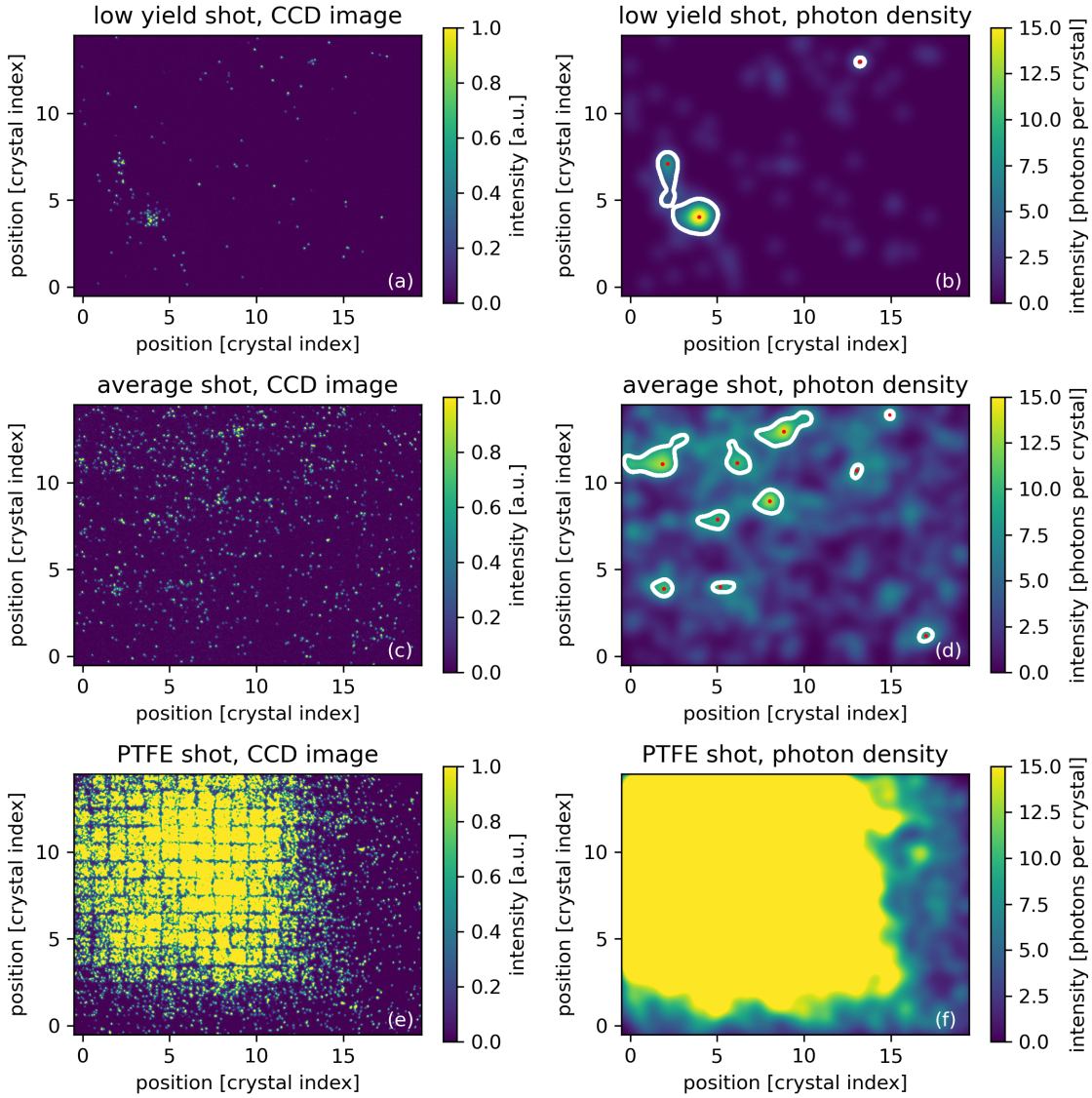

Figure 3.38.: Examples for the three types of SPD images, low yield shots (a), typical Breit-Wheeler shots (c) and high yield shots like PTFE (e). The corresponding photon density maps with identified candidate events are shown on (b), (d) and (f). The photon cluster identification works best for low yield shots. On average Breit-Wheeler shots, the photon background is too high for good cluster identification.

3.7.3. Statistical Positron Yield Analysis

The single particle detector is the primary diagnostic for Breit-Wheeler measurements. In sections 3.7.1 and 3.7.2, two independent methods to determine the positron yield from SPD images on each shot are presented. To measure the Breit-Wheeler effect, a statistical analysis of the obtained positron yield over many shots needs to be performed. A statistical approach is required, because the background is much larger than the Breit-Wheeler signal at an approximate signal-to-noise ratio of 10^{-5}. The basic idea is to take enough data to bring the error below the signal-to-noise ratio. There are many sources of errors on this experiment, that will be summarised in three subgroups. Those are measurement errors, systematic errors and statistical errors. Measurement errors include inaccuracies of the AMS positron yield and reference LWFA charge measurements. Systematic errors include the assumptions under which the measurements were taken, for example that the yield on the γ-ray beam profile diagnostic is linear to reference LWFA charge or that the accelerator has a constant average performance. Systematic errors are not quantified in error margins of the calculated values due to their complexity. Instead they are discussed when results are presented. Statistical errors are intrinsic uncertainties due to stochastic processes like the pair production itself, for example can a mean signal of one positron every 100 shots not be measured accurately by taking only 10 shots even if the measurement itself is 100% accurate.

Calculating mean AMS Positron Rates

The most relevant properties measured on every shot are the total yield on the γ-ray profile diagnostic and the SPD image, which gives the reference LWFA charge and two values for AMS positrons, one for each method mentioned in sections 3.7.1 and 3.7.2. Both AMS positron yields are evaluated independently with equal methods, so this explanation will only consider one. There is a quantity of AMS positrons p_i and a quantity of reference charge q_i on each shot obtained by the processed and calibrated SPD and γ-profile diagnostics. To measure the Breit-Wheeler effect, a difference in the number of AMS positrons per reference charge needs to be observed on shots where the Breit-Wheeler reaction is enabled, called collision shots, compared to shots without the Breit-Wheeler process enabled, called background shots. The mean rate $\frac{p}{q}$ in AMS positrons per reference charge on collision and background sets can be calculated in two different ways. The first is under the assumption that every shot is an independent measurement of the rate $\frac{p_i}{q_i}$ so that the average value is obtained by the arithmetic

mean over all shots like

$$\frac{p}{q} = \frac{1}{N_{shots}} \sum_{i=1}^{N_{shots}} \frac{p_i}{q_i} \tag{3.3}$$

with N_{shots} being the total number of shots. The spread of the data due to shot to shot fluctuations is characterised with the standard deviation and the error of the mean rate is obtained by the standard error of the mean. Measurement errors $\delta p_{i,meas}$ and $\delta q_{i,meas}$ as well as statistical errors $\delta p_{i,stat}$ need to be calculated for each shot and considered additionally to the standard error of the mean by propagation of uncertainty [51]. Measurement errors induced by the uncertainty of both calibration values are 9% from GammaProfile and 1% from SPD, which equates to 10% for the rate. Typical standard errors of the mean rate are approximately 10% but can be as high as 25% for certain data sets. The statistical error depends on the absolute number of AMS positrons, is Poisson limited and varies between 100% and 25% for 1 and 15 AMS positrons respectively, where typical values are 5 AMS positrons or 45% error. Due to this low AMS positron yield per considered measurement, which is one shot with this method, the error of the mean rate is dominated by the statistical error. This is improved by the second way to calculate the mean rate of AMS positrons per reference charge, which is by treating the full dataset as a single measurement so that the total positron yield $P = \sum_i p_i$ can be divided by the total charge $Q = \sum_i q_i$ like

$$\frac{P}{Q} = \frac{\sum_i p_i}{\sum_i q_i} \tag{3.4}$$

to obtain the positron rate. The error of this mean rate is obtained by propagation of uncertainty from the measurement errors $\delta p_{i,meas}$ and $\delta q_{i,meas}$. The individual statistical errors $\delta p_{i,meas}$ can be folded in by propagation of uncertainty too, however, Raikov's theorem [78] allows a major simplification. This law states that the sum of independent Poisson distributed random variables is Poisson distributed. For the measured total AMS positron yield $P = \sum_i p_i$, where $p_i \sim \text{Pois}(\lambda_i)$ is Poisson distributed, this means

$$P = \sum_i p_i \sim \sum_i \text{Pois}(\lambda_i) = \text{Pois}\left(\sum_i \lambda_i\right) \tag{3.5}$$

with λ_i being the mean of the Poisson distribution with which p_i is distributed. This allows an easy estimate of the statistical error δP_{stat} of P based on a Poisson distribution defined by the mean $\lambda = \sum_i \lambda_i$, of which the maximum likelihood estimate $\hat{\lambda}$ is given by the measured AMS positron yield $P = \sum_i p_i$, so $\delta P_{stat} \approx \sqrt{P}$, which is

much smaller than $\delta p_{i,stat} \approx \sqrt{p_i}$. This is described in greater detail in section 2.3.2. The error of P caused by measurement errors as well as random shot to shot fluctuations is determined from the measured data with the bootstrap [79] method. This works by randomly resampling the data, where the number of samples is kept constant, and performing the full analysis on each sample P_j. Properties of the distribution of all P_j like mean and standard deviation can then be used as an estimate for P.

Evaluating the Difference between two Datasets

The Breit-Wheeler effect needs to be measured as an increase of AMS positrons per reference charge on collision shots compared to background shots. A measurement of this difference has two important characteristic parameters, the absolute difference and the confidence in the difference. The absolute difference is obtained by subtraction of the AMS positron rate on background shots from collision shots and the error is composed of the statistical error and the measurement error.

The confidence in the difference characterises the probability that a difference between collision and background shots has been measured and that is is not a random statistical phenomenon of to the underlying stochastic processes. The inverse of this probability is sometimes referred to as false alarm probability. To comprehend this, a coin flip experiment to determine the chance for heads can be imagined. Two identical coins are flipped twice each with 0 and 2 heads for coin A and B respectively. The measurement error is practically zero, because it is obvious if a coin shows heads. The result is a clear greater chance for heads with coin B despite using identical coins. A statistical error margin evaluates the intrinsic stochastic behaviour of the measurement, or more precisely, what can be inferred about the underlying chance to flip heads based on the measurement. In case of a coin flip experiment, the number of heads for a given number of trials follows a binomial distribution, like Breit-Wheeler pairs, and a measurement is used to estimate the probability. The error margin of this estimate can be characterised with many parameters, but for the Breit-Wheeler measurement, the probability that the underlying AMS positron rate on collision shots is larger compared to background shots is used, specified by the largest possible confidence interval around the maximum likelihood estimates of the pair rates on collision and background shots. A detailed description of this calculation is presented in section 2.3.2. The error margin of the confidence in the difference is calculated by bootstrapping. To make the absolute confidence consistent with its own error margin, the lower and upper limits were chosen to be the $\frac{1-p}{2}$th and $\frac{1+p}{2}$th quantiles of the bootstrap population, where p is the absolute confidence. In other words, the confidence p is within $p - a$

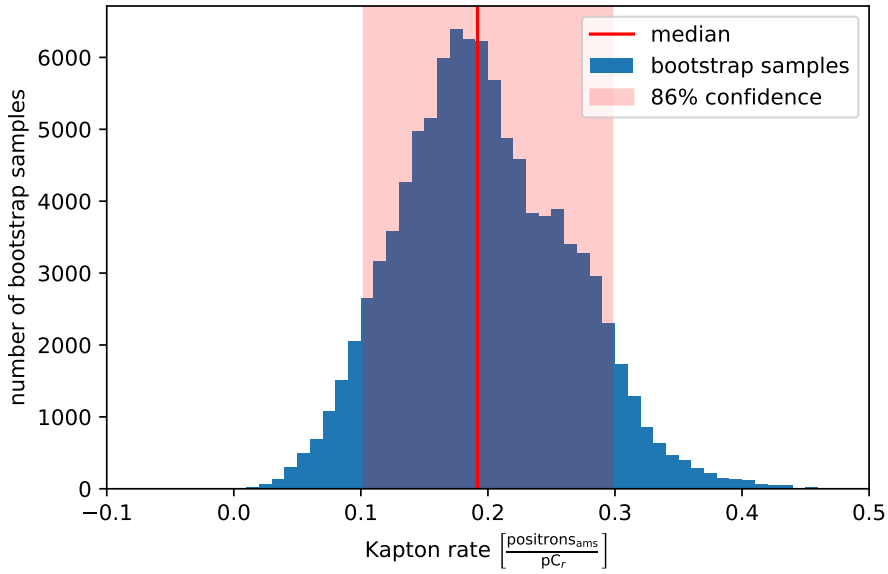

Figure 3.39.: A histogram of the measured rate increase with a 25 µm Kapton target in the beam above background. The full dataset gives one value for the rate. By randomly resampling the data (bootstrap), slightly different values were obtained each time due to fluctuations in the data. This plot is a histogram of the Kapton rate of all 10^5 resampled subsets (bootstrap samples).

and $p + b$ in $(p \cdot 100)\%$ of all cases. It therefore represents a robust overall confidence that includes statistical and measurement errors. An example for such a bootstrap population is presented on Fig. 3.39, which is created based on a dataset with a 25 µm Kapton target in the beam. The dataset was resampled 10^5 times and the evaluation was redone on each sample to obtain 10^5 different values for the AMS positron rate increase with the Kapton target. The resulting distribution of those rates on Fig. 3.39 is characterised by the median with an error margin that covers a certain fraction of the population. This fraction is set to the obtained confidence level from the single particle statistic for this dataset. For this example, the single particle confidence is 86%, to the error margin around the median of the bootstrap population is also set to contain 86% of all samples.

More values for this example evaluation are presented in Table 3.2. The positron rate with and without Kapton is obtained by dividing total positron yield by total charge. The error is the confidence interval for 68% confidence, which is the equivalent to one standard deviation of a normal distribution. The difference between datasets without and with Kapton in Table 3.2 is the net signal produced by the target, also shown on Fig. 3.39. The error of the difference is obtained by propagation of uncertainty and the

Table 3.2.: Example data to show the evaluation. Mean rates w/ and w/o Kapton are obtained by dividing total positron yield by total charge with statistical errors at 68% confidence (1σ). The confidence in the difference is specified in section 2.3.2 as largest possible confidence interval. To fold shot-to-shot fluctuations into the confidence estimate, the boostrap method is used to determine the error margin of the calculated confidence.

		AMS positron rate $\left[\frac{\text{positrons}_{\text{ams}}}{\text{pC}_r}\right]$			
method	property	w/o Kapton	w/ Kapton	difference	bootstrap
integral	mean	0.246	0.433	0.188	0.191
	error	$^{+0.059}_{-0.048}$	$^{+0.088}_{-0.074}$	$^{+0.106}_{-0.088}$	$^{+0.105}_{-0.087}$
	confidence	-	-	85%	86^{+10}_{-28}%
cluster	mean	0.153	0.243	0.090	0.090
	error	$^{+0.049}_{-0.038}$	$^{+0.069}_{-0.055}$	$^{+0.085}_{-0.067}$	$^{+0.059}_{-0.045}$
	confidence	-	-	60%	61^{+23}_{-31}%

confidence in the difference is the probability that a positive difference is not a random statistical phenomenon, calculated as defined in section 2.3.2. The entire analysis is redone 10^5 times with random resampling, called bootstrap shown on Fig. 3.39. This gives 10^5 differences, errors and confidence values that are distributed in a certain way, which is characterised by the median and a dataset specific confidence interval equal to the confidence in the difference. The confidence in the difference, which has a value of 86% for the integral method, is characterised with an error margin that covers 86% of all bootstrap samples. The evaluation is done for AMS positron yields from both methods specified in sections 3.7.1 and 3.7.2.

4. Results

4.1. Radiation Background Characterisation

From combined Geant4 and Radia simulations it is known that positrons through the AMS impact the SPD in the open detector region shown on Fig. 3.35. This is experimentally confirmed by the PTFE data that showed a 44 times higher yield in the open region versus only 4 times more signal in the shielded region compared to background data without any positron source. The measured yields during PTFE and background (BG) shots are shown in Table 4.1 in the first and second row. The factor 4 higher signal in the shielded region on PTFE shots most likely originates from scattered PTFE positrons inside and around the SPD. The SPD signal in the shielded region on background shots is therefore assumed to originate from scattered particles through the γ-ray beam dump in form of diffuse low energy radiation and is equally distributed over the SPD. Analysing the SPD yield in the shielded region spanning 92 crystals gives a signal equivalent to $(0.12 \pm 0.01)\ \frac{\text{positrons}_{\text{ams}}}{\text{pC}_r}$ or $(1.27 \pm 0.11) \cdot 10^{-3}\ \frac{\text{positrons}_{\text{ams}}}{\text{pC}_r \cdot \text{crystal}}$. This signal is calculated in $\frac{\text{positrons}_{\text{ams}}}{\text{pC}_r}$ although it is not composed of AMS positrons. The SPD can not distinguish between photons from positrons and low energy radiation, which is why any signal will be measured in calibration based $\frac{\text{positrons}_{\text{ams}}}{\text{pC}_r}$. In case of low energy radiation, the measured value can be understood as the amount of radiation that induces a signal equivalent to the calculated amount of AMS positrons. The measured low energy signal is assumed to be present in the open region as well, where it induces a signal equivalent to $(0.26 \pm 0.02)\ \frac{\text{positrons}_{\text{ams}}}{\text{pC}_r}$ based on the 208 crystal large area. Subtracting this from the total background signal equivalent of $(0.51 \pm 0.02)\ \frac{\text{positrons}_{\text{ams}}}{\text{pC}_r}$ gives a difference equivalent to $(0.25 \pm 0.02)\ \frac{\text{positrons}_{\text{ams}}}{\text{pC}_r}$. All values are summarised in Table 4.1. The additional background signal is only observed in the open region where signal from the PTFE target was measured, so it is assumed to be high energy positrons propagating through the analyser magnet system. This in return implies that the background radiation on the SPD is composed of at least two different types of radiation, scattered low energy radiation from the γ-ray beam dump and high energy positrons transmitted through the AMS. Those high energy positrons can originate

Table 4.1.: Measured SPD yield during background (BG) and PTFE shots within the open and shielded region as defined on Fig. 3.35 as well as the deduced composition of BG signal.

data type	SPD yield $\left[\frac{\text{positrons}_{\text{ams}}}{\text{pC}_r}\right]$	
	open region	shielded region
PTFE	22.3 ± 0.3	0.45 ± 0.04
BG	0.51 ± 0.02	0.12 ± 0.01
BG (low energy radiation)	0.26 ± 0.02	0.12 ± 0.01
BG (AMS positrons)	0.25 ± 0.02	0.00

from scattering of the γ-ray beam with gas particles in the vacuum chamber induced by the LWFA gas target or solid objects close to the beam axis, for example the lead shielding wall in between the Breit-Wheeler interaction region and the separator magnet shown on Fig. 3.1.

4.2. SPD Sensitivity Validation

The single particle detector was calibrated with a PTFE target in the beam to produce a defined positron signal on SPD. To cross-check this calibration and to validate the single positron detection capability of the system, data sets with the 25 µm thick Kapton tape from the x-ray target in the beam were taken. In a simulation with Geant4 and tracking with Radia, this Kapton target induced 5 positrons on the detector from an LWFA beam containing 9.2 pC_r. At this low rate, the uncertainty of the mean SPD signal is dominated by Poisson statistics. In this case of one simulation yielding 5 positrons, the Kapton rate can be estimated to be within 2.8 and 8.4 positrons per shot at a 68% confidence. The LWFA beam charge in the simulation was 9.2 pC_r, implying the spectral shape measured during the calibration run, so the rate can be estimated to be within 0.31 and 0.91 AMS positrons per pC_r. This is under the assumption that the full γ-ray beam passes through the Kapton target. By moving the target partially out of the beam path, the produced positron signal was varied continuously from the maximum of $0.54^{+0.37}_{-0.24}$ $\frac{\text{positrons}_{\text{ams}}}{\text{pC}_r}$ to zero. Data with the Kapton target at three different positions in the beam was taken and is used as a test of the single particle detector as well as the evaluation methodology and algorithms. The results are summarised in Table 4.2. The first position is at Breit-Wheeler shooting position,

Table 4.2.: Measured and simulated Kapton signal above background to test the SPD sensitivity. The top values are obtained with the calibration and the bottom values with the cluster identification method.

γ-beam coverage	measured $\left[\frac{\text{positrons}_{\text{ams}}}{\text{pC}_r}\right]$	simulated $\left[\frac{\text{positrons}_{\text{ams}}}{\text{pC}_r}\right]$	confidence
20 %	0.093 ± 0.031	$0.11^{+0.07}_{-0.05}$	80^{+13}_{-26} %
50 %	0.191 ± 0.067	$0.27^{+0.18}_{-0.12}$	86^{+10}_{-29} %
80 %	0.193 ± 0.026	$0.43^{+0.30}_{-0.19}$	99^{+1}_{-11} %
20 %	0.054 ± 0.035	$0.11^{+0.07}_{-0.05}$	73^{+22}_{-53} %
50 %	0.090 ± 0.068	$0.27^{+0.18}_{-0.12}$	61^{+22}_{-32} %
80 %	0.093 ± 0.034	$0.43^{+0.30}_{-0.19}$	58^{+26}_{-41} %

where the tape sits 1 mm off axis. At this position, the tape would be shielded by the tungsten block on Breit-Wheeler shots, which was removed for this measurement. 20% of the γ-ray beam hits the tape at this position. The second position is with no distance to the beam axis, so that 50% of the γ-ray beam hits the target. The final position is 1 mm past the axis of the γ-ray beam, covering 80%. The simulated values are also included in Table 4.2. The evaluation of SPD images was done with both the calibration and the photon cluster identification methods described in sections 3.7.1 and 3.7.2. The top three values in Table 4.2 are calculated with the calibration and the last three with the photon cluster identification method.

The calibration inferred results are discussed first, which are the top three rows in Table 4.2. All three configurations show a measured increase of SPD signal due to the Kapton tape on top of background radiation, which was between 0.3 and 0.5 $\frac{\text{positrons}_{\text{ams}}}{\text{pC}_r}$ depending on the dataset. The absolute values for 20% and 50% agree well with the simulation within error margins, shown in Table 4.2. The relative growth in signal magnitude from 20% to 50% coverage agrees with the simulated increase. The confidence in the difference is 80% and 86% for 20% and 50% coverage respectively and is defined by the absolute difference as well as the total amount of charge being sent through the system during the measurement. The smallest dataset is for 50% coverage, where the total charge on background and Kapton shots was 105 pC_r and 78 pC_r respectively. 26 AMS positrons were detected on background and 34 on Kapton shots. The dataset with 20% coverage is composed of 294 pC_r with 93 AMS positrons on background and 315 pC_r with 130 AMS positrons on Kapton shots. Because the 20% coverage dataset has more charge, the confidence is almost as high as for 50%

coverage despite the lower absolute difference. The dataset with 80% γ-ray beam coverage has both high charge and a high absolute difference, which yields a large confidence in the difference of 99%. This is almost the $3\,\sigma$ boundary of a normal distribution. Background shots have $294\,\mathrm{pC}_r$ with 93 AMS positrons and Kapton shots $295\,\mathrm{pC}_r$ with 151 AMS positrons. However, the 80% coverage set does not shown an increase in the absolute rate compared to 50% coverage, which can be seen in the difference between measured and simulated rates for 80% coverage in Table 4.2. It also does not agree with the simulation as good as the other datasets. A reason for this discrepancy can be a systematic error, for example a systematic LWFA beam pointing offset. This would cause the γ-ray beam to miss part of the Kapton target and reduce the coverage percentage. Another error can always be a systematic change in the LWFA beam spectrum so that the assumption of a constant average spectral shape is not valid.

The results obtained with the photon cluster identification method, which are the lower three rows in Table 4.2, generally have lower absolute values and lower confidences. This is caused by the high background that causes the number of identified clusters to saturate because they spatially overlap. Further is the contrast of clusters worse, which makes the identification harder. This data shows that the background level is too high for the photon cluster identification method to work efficiently, however the increase in signal from the Kapton target is still measurable, confirming that the method works in principle.

Overall, the Kapton datasets demonstrate the detection capability of a low AMS positron rate on top of a more intense background radiation with the developed hardware and software, proving that the system is sensitive to signals composed of single positrons per shot. The obtained absolute rates are close to the simulation which shows that additionally to a pure difference, the absolute AMS positron rate can be determined. The signal-to-noise ratio for this measurement was, depending on γ-ray coverage and background level for the individual measurements, between 0.4 and 0.6. The calculations for the required sample sizes to achieve a certain statistical significance presented in section 2.3.2 for the signal-to-noise ratios achieved in this measurement also agree very well with the measurements. According to section 2.3.2, the required sample size to achieve a statistical significance, or confidence in the difference, of 99% for a Poisson distributed signal at a signal-to-noise ratio of 0.6 is predicted to be 98 positrons on background and 157 on Kapton shots. The measured AMS positron numbers are 93 and 151, showing very good agreement.

4.3. Detected Breit-Wheeler Signal

The overall aim of the experiment was to measure the linear Breit-Wheeler pair creation process. To put the measured rate into perspective, it is mandatory to compare it to a theoretical prediction to explain the outcome. An important step to complement the campaign is therefore an estimate of the expected magnitude of the Breit-Wheeler signal on SPD. For this, a calculation of the expected pair rate by simulating the collision process as described in section 2.2.2 with the measured γ-ray and x-ray beam properties was done for the two main datasets, which is presented in this section. This is followed by the evaluation of the measured Breit-Wheeler data.

4.3.1. Predicted Pair Rate

It was intended to measure the γ-ray spectrum with the dedicated diagnostic on a single shot basis, however the evaluation of this data revealed that the spectral resolution of the unfolded γ-ray spectrum was very poor. It was in fact more inaccurate than the assumption of a constant average LWFA beam, so that the calculated γ-ray spectrum is used to simulate the expected Breit-Wheeler pair yield. The electron spectrum was measured in advance of every Breit-Wheeler dataset and the spectral shape can be seen on Fig. 4.1(a). This electron spectrum was propagated in Geant4 through the converter target, collimator and magnet to get the γ-ray spectrum at the Breit-Wheeler interaction point, shown on Fig. 4.1(b). The spatial distribution of the resulting γ-ray beam at the interaction plane was modelled as a 2D Gaussian distribution with 1.8 mm standard deviation. The 1.8 mm is estimated through a 400 mm electron beam propagation at 1 mrad measured divergence with a subsequent 1100 mm propagation of the scattered γ-ray beam at a divergence of 2 mrad, which comes from the additional scattering angle through the Bremsstrahlung process that approximately scales with $\frac{1}{\gamma} \approx 1$mrad for 500 MeV γ-ray photons. The x-ray spectrum was measured on the experiment with a crystal spectrometer on a single shot basis and the average spectral shape is shown on Fig. 4.2.

The measured x-ray and γ-ray spectra were integrated into the algorithm presented in section 2.2.2 and the expected pair rate λ was calculated, which is approximately equal to the probability P of producing at least one pair. The result is $P \approx \lambda = 7.0 \cdot 10^{-5}$ pairs per shot or around one pair in 14.300 shots. These pairs propagate through the analyser magnet system to the single particle detectors, where due to the limited transport efficiency around 14% of all produced pairs impact the SPD. The simulation was done with 9.2 pC_r, so the AMS positron rate on detector is $1.7 \cdot 10^{-6}$ $\frac{\mathrm{positrons_{ams}}}{\mathrm{pC}_r}$.

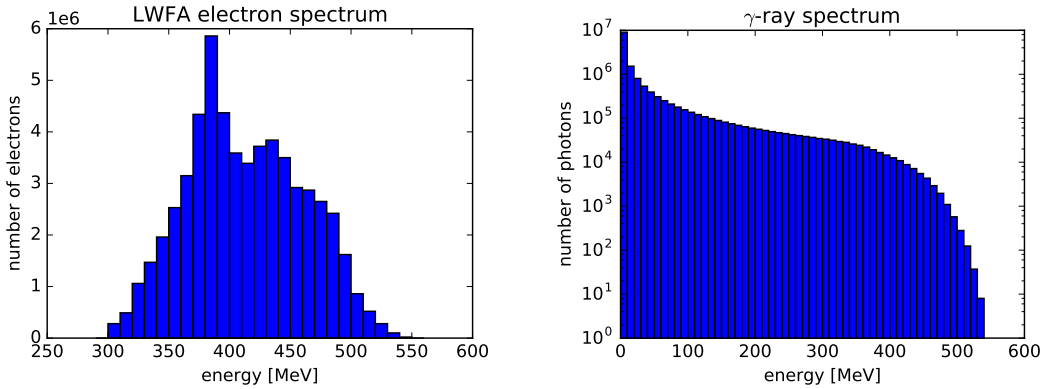

Figure 4.1.: The measured LWFA electron spectrum in advance of the Breit-Wheeler measurement and the simulated γ-ray spectrum created through Bremsstrahlung inside the converter target.

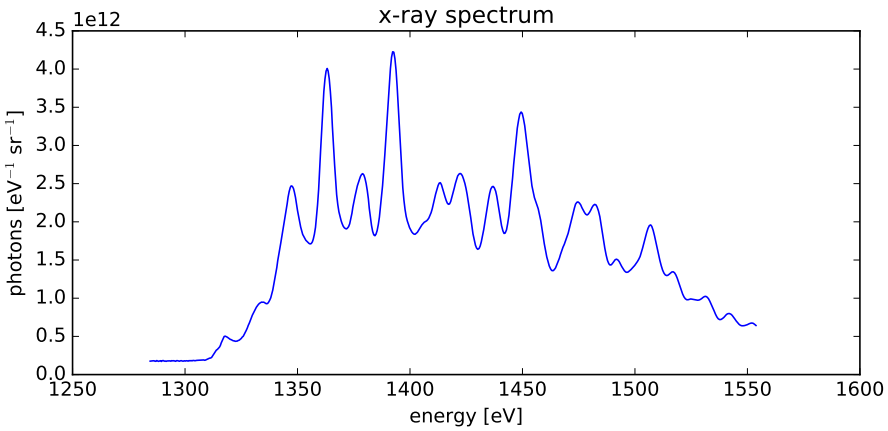

Figure 4.2.: The average x-ray spectrum measured with a crystal spectrometer during Breit-Wheeler shots.

On other datasets, the LWFA and x-ray beam properties were slightly different and the pair rate changes accordingly. The simulated rates for the two datasets are summarised in Table 4.3.

4.3.2. Measured Pair Rate

The major aim of the campaign presented in this work was to obtain experimental evidence of the Breit-Wheeler process. Data on this was taken in two major sets A and B. As described in section 2.3, the Breit-Wheeler effect needs to be measured on top of background radiation. This was done by taking two types of data shots, one with full pair creation enabled, called collision shots (COL), and another one

Table 4.3.: Simulated pair rates for different datasets.

dataset	$\lambda \left[\frac{\text{positrons}_{\text{ams}}}{\text{pC}_r}\right]$ produced	$\lambda \left[\frac{\text{positrons}_{\text{ams}}}{\text{pC}_r}\right]$ on SPD
A	$1.5 \cdot 10^{-5}$	$2.1 \cdot 10^{-6}$
B	$1.2 \cdot 10^{-5}$	$1.7 \cdot 10^{-6}$

without pair creation to measure the background (BG). The difference is that on background shots only the LWFA driver beam was fired, so no x-rays were produced and the Breit-Wheeler process is suppressed. To determine if a signal increase on collision shots is due to any effects of the x-ray driver beam besides Breit-Wheeler pair creation, a second type of background shots was taken with both lasers firing but offset timings. This way any signal on SPD caused by the x-ray driver is included but the Breit-Wheeler reaction is strongly suppressed. This type of shots is called hot background shots (HBG). When specifically referring to the difference between hot and 'normal' background shots, the latter will be called cold background shots. If not otherwise stated, background shots will automatically refer to cold background shots. The reason why not all background shots on the experiment were taken as hot background shots is the experimental effort to align each x-ray target, which would have decreased the amount of data that could be taken. All data shots were processed as described in section 3.7.3. An overview of all data shots to get a general impression for the fluctuations, absolute values and differences between different sets as well as long term drift effects is given in form of a timeline on Fig. 4.3. The x-axis on this plot is the Gemini shot number (gsn), which is a number that progressively counts the shots at Gemini since the laser started operation and is therefore a unique identifier for each shot. The gsn itself has no physical meaning, it is only used to put the shots in order. All data shots shown on Fig. 4.3 were taken over the course of three days.

General Properties of Breit-Wheeler Datasets

The measured Breit-Wheeler data is obtained in two major sets A and B with each set being composed of background (BG) and collision (COL) shots. Between the sets A and B, the LWFA properties were different to a degree that the expected Breit-Wheeler pair rate would be different as presented in Table 4.3. Dataset B is additionally subdivided into 3 subsets B1 to B3. This subdivision is due to experimental circumstances under which the data was taken that may affect the background rate and need to be addressed before considering all subsets B1 to B3 as a single measurement as described in section 3.7.3. General properties of all 4 datasets are presented in Table 4.4. The

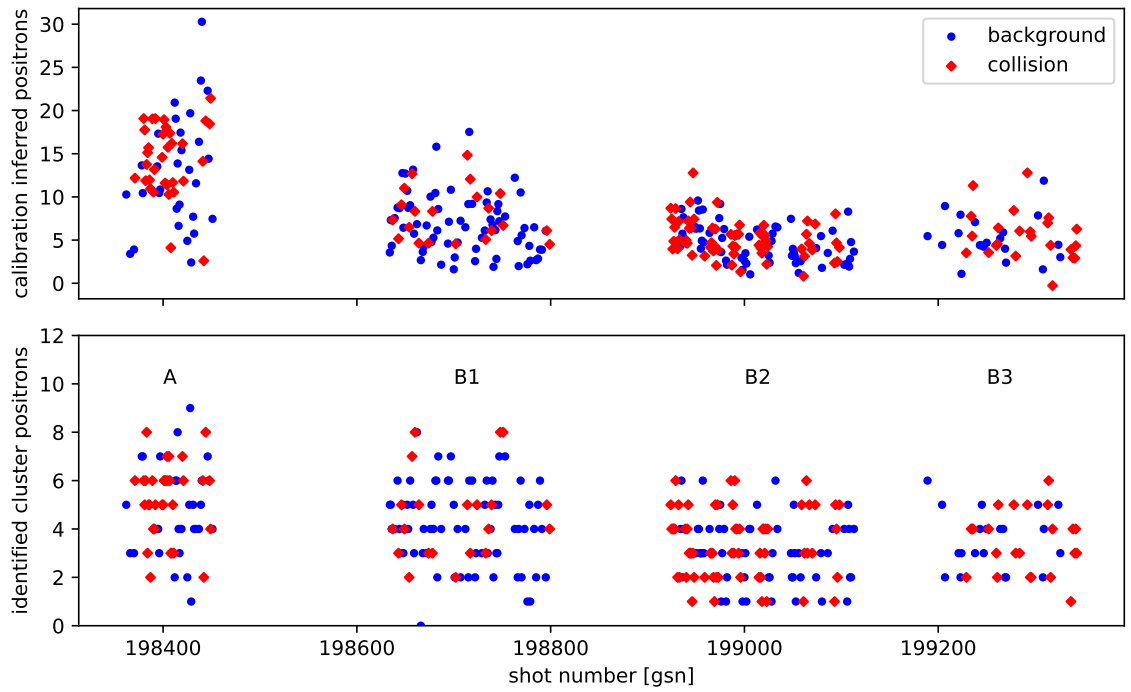

Figure 4.3.: A timeline over all Breit-Wheeler shots to get a general impression of shot-to-shot variations, measured yields and long term drift effects. Shown is the calibration inferred AMS positron yield on the top and identified photon cluster positrons on the bottom. Yields are plotted against the Gemini shot number (gsn). The labels A and B1 to B3 denote different datasets.

datasets are composed of 43 to 117 shots and contain between 490 pC_r and 1.6 nC_r reference charge. The errors of reference charge and calibration inferred AMS positron yield measurements are based on the calibration uncertainty presented in Table 3.1. The values obtained by the photon cluster identification method are given without error margins due to the lack of a measurement error. Table 4.4 does only include 'good' shots as specified in section 3.7.1.

Differences between Background and Collision Sets

The Breit-Wheeler effect is measurable as an AMS positron rate increase on collision shots over background shots. This difference in rate is obtained with two different methods that are presented in section 3.7.3, which are averaging over shots and averaging over total charge. Together with the two methods of determining the positron yield on SPD presented in sections 3.7.1 and 3.7.2, which were calibration inferred and photon cluster search, 4 AMS positron rates per reference charge are

Table 4.4.: General properties of the Breit-Wheeler data sets.

dataset	shot type	shots	charge [pC$_r$]	AMS positrons	
				integral	cluster
A	background	29	504 ± 45	377 ± 5	138
	collision	33	603 ± 54	471 ± 7	172
B1	background	69	1159 ± 104	469 ± 7	288
	collision	21	434 ± 39	167 ± 2	96
B2	background	55	757 ± 68	257 ± 4	169
	collision	62	846 ± 76	321 ± 4	210
B3	background	20	226 ± 20	105 ± 1	71
	collision	23	264 ± 24	128 ± 2	80

obtained for each dataset. All values are presented in Table 4.5. For each dataset and method, there are 2 values given. The first value is the absolute AMS positron rate difference between background and collision shots with an error margin defined by the standard deviation of the bootstrap population. The second value is the fraction of bootstrap samples that have a rate increase larger than zero.

The rate differences in Table 4.5 have a large spread between -0.044 and 0.065 AMS positrons per reference charge with error margins that are often larger than the absolute values, indicating that there is no clear systematic difference between background and collision shots. The fraction of bootstrap samples with a positive difference varies between 8% and 96%, where values below 50% actually indicate a rate decrease on collision shots.

Dataset A shows the strongest increase if the data is evaluated with the calibration method and averaged per shot, but features a much lower difference when evaluated with the photon cluster method. This strong difference between the methods is due to the overall higher background rate for dataset A, which can be seen on Fig. 4.3. This high background between 10 and 20 calibration inferred positrons per shot causes the photon cluster identification method to saturate because individual photon clusters are too close together and multi-positron events are counted as single events. This can be seen in Table 4.4, which exhibits a systematically lower ratio of cluster positrons to integral positrons for dataset A compared to dataset B. The discrepancy of positron rate differences in Table 4.5 between averaging over shots versus averaging over charge

Table 4.5.: Measured rate differences between background and collision shots.

dataset	measured AMS positron rate $\left[\frac{\text{positrons}_{\text{ams}}}{\text{pC}_r}\right]$			
	calibration		photon clusters	
	per shot	per charge	per shot	per charge
A	0.065 ± 0.051	0.034 ± 0.047	-0.004 ± 0.035	0.011 ± 0.030
	90%	77%	46%	64%
B1	-0.020 ± 0.031	-0.019 ± 0.027	-0.044 ± 0.030	-0.028 ± 0.025
	25%	23%	8%	14%
B2	0.039 ± 0.025	0.040 ± 0.022	0.019 ± 0.023	0.025 ± 0.019
	93%	96%	80%	90%
B3	0.011 ± 0.056	0.021 ± 0.051	-0.020 ± 0.045	-0.012 ± 0.049
	58%	66%	33%	40%

for dataset A indicates a large fluctuation in charge per shot so that averaging over shots induces additional errors. The combination of too much signal per shot for the photon cluster method and too strong shot-to-shot fluctuations for averaging over shots causes the large differences between the various methods for dataset A, which is further represented by the large uncertainties.

Dataset B with the subsets B1 to B3 features generally lower positron yields per shot as seen on Fig. 4.3. B1 and B3 feature larger shot-to-shot fluctuations compared to B2, which is visible in form of generally larger error margins, especially for B3, which has the largest errors of all datasets in Table 4.5. The set B1 is interesting because it shows a systematic positron rate decrease on collision shots for all 4 evaluation methods. A rate decrease is not expected from the Breit-Wheeler reaction, but since the measurement is a statistical process, negative values are generally possible. The dataset with the highest rate difference over all methods is B2, which also features the most similar results within all 4 methods. This set also features the lowest error margins over all methods, which is again due to lower shot-to-shot fluctuations shown on Fig. 4.3. B2 is therefore the statistically most significant dataset.

Statistical Significance of the Differences

The data in Table 4.5 presents the measured values with error margins obtained by bootstrapping. This allows to estimate the confidence in the results based on

Table 4.6.: Calculated statistical significances of the measurements.

dataset	calibration based method		photon cluster method	
	rate $\left[\frac{\text{positrons}_{\text{ams}}}{\text{pC}_r}\right]$	confidence	rate $\left[\frac{\text{positrons}_{\text{ams}}}{\text{pC}_r}\right]$	confidence
A	0.034 ± 0.047	$32^{+18}_{-20}\,\%$	0.011 ± 0.030	$16^{+10}_{-10}\,\%$
B1	-0.019 ± 0.027	$-35^{-16}_{+19}\,\%$	-0.028 ± 0.025	$-56^{-24}_{+35}\,\%$
B2	0.040 ± 0.022	$63^{+20}_{-29}\,\%$	0.025 ± 0.019	$51^{+21}_{-28}\,\%$
B3	0.021 ± 0.051	$15^{+9}_{-9}\,\%$	-0.012 ± 0.049	$-18^{-11}_{+11}\,\%$

measured shot-to-shot variations, for example is the fraction of bootstrap samples that show a signal increase on collision shots as high as 96%, so the data shows an increase with 96% confidence based on measurement accuracy. However, as described in section 2.3.2, there are statistical uncertainties that can not be deduced solely from the obtained data. To quantify these statistical limitations, an underlying distribution of the measured quantity needs to be assumed and the data analysed accordingly. In case of the Breit-Wheeler effect the assumption is that produced pairs follow a Poisson distribution. A measurement of a certain amount of pairs or positrons per input quantity, which is reference charge within this analysis, is then used to estimate the properties of the underlying distribution. The estimation of those properties has an additional error that is based on the overall amount of data that was recorded and not on the measurement error. As an example, two measurements X and Y can be imagined, both showing an increase of 1 positron per pC, but measurement X was done with 10 pC and Y with 1 nC. The significance of the result is greater for Y, because the underlying rate of the Breit-Wheeler process can be determined more accurately despite the measurement accuracy being the same. The calculation of such a statistical significance is essential for any measurement of statistical quantities and is done as described in section 2.3.2 by calculating the largest confidence interval for background and collision data that do not yet overlap. The result is expressed in terms of the probability that the measured effect is not a random phenomenon based on a Poisson distribution. Because the assumption of an underlying Poisson distribution is violated if the data is averaged over shots, the statistical significance is only calculated for the method of averaging over total charge. The results are presented in Table 4.6.

Dataset A shows a confidence of 32% and 16% for the calibration and photon cluster methods. The value obtained with the photon cluster method is again lower. Dataset B has a large variety of confidences, with B3 being the lowest and B1 showing negative

values. A negative confidence means that it shows the probability of a rate decrease on collision shots. Dataset B2 has the highest confidence of 63% for the calibration and 51% for the cluster method. Overall, most confidence values except B2 are below 50%, which means that the probability that the measured increase is a statistical phenomenon is larger than the probability that the result is a real signal. For B2 with the calibration method, the probability that the result is random fluctuations is 37%. None of these measurements is considered to be a significant result. This agrees well with the theoretically predicted signal, which is based on the measured LWFA and x-ray performance including the AMS transport efficiency. The predicted signal for dataset B is $1.7 \cdot 10^{-6} \frac{\text{positrons}_{\text{ams}}}{\text{pC}_r}$, so it is 4 orders of magnitude below the achieved measurement accuracy and is therefore not measurable with this setup.

The measurement accuracy can be raised by increasing the size of the dataset, which is done by unifying the subsets B1 to B3 into B. To obtain the largest possible dataset from this experiment and by extension the most precise result, datasets A and B are also unified and presented in Table 4.7. The result for the unified set B shows a smaller absolute rate compared to the subsets in Table 4.6 for both evaluation methods, which is expected when averaging over all subsets. The error margin is smaller too, because the dataset is larger overall. The same is true for the confidence. The error margin of the confidence, which indicates how reliable the confidence estimate is based on measured fluctuations, is also decreased. All these changes after unifying B1 to B3 into B are expected. However, a very interesting behaviour is observed after unifying A and B. The measured rate difference is 0.05 AMS positrons per pC_r for the calibration based method, which is larger than any of the subset values from Table 4.5. The question is, how can an average value be larger than any of the values that are averaged. The answer is a systematic error and that the basic assumption of this averaging method is violated, which is that all shots are assumed to be taken under equal conditions. Dataset A features a larger background rate than B, seen on Fig. 4.3, so background and collision shots will have a systematically higher yield. This is fine as long as background and collision shots at the same average background level are compared, however, if background shots during periods of low average background are compared with collision shots taken over periods with high average background, the higher background component on collision shots will be measured as an increase in signal. Dataset A, where the background is high, contains more charge on collision shots. Vice versa contains dataset B, where the background is low, more charge on background shots. This causes an overall larger amount of charge on collision shots with high background. In return contain background shots more charge during periods

Table 4.7.: Measured positron rate differences and statistical significances of the unified datasets.

dataset	calibration based method		photon cluster method	
	rate $\left[\frac{\text{positrons}_{\text{ams}}}{\text{pC}_r}\right]$	confidence	rate $\left[\frac{\text{positrons}_{\text{ams}}}{\text{pC}_r}\right]$	confidence
B	0.011 ± 0.018	$27^{+15}_{-15}\,\%$	0.004 ± 0.015	$11^{+7}_{-7}\,\%$
A + B	0.050 ± 0.027	$92^{+8}_{-82}\,\%$	0.008 ± 0.013	$28^{+17}_{-18}\,\%$

of low background. When A and B are unified, the additional background per charge on collision shots is identified as a false net signal increase on collision shots, which explains the sudden high signal in Table 4.7. This effect is further not recognised by the confidence either, which is as high as 92%, because it only contains measurement and statistical, but no systematic errors. A hint towards a false measurement is the very large error margin of the confidence, which varies between 100% and 10%. If data taken at different background rates shall be unified, the varying background needs to be corrected, which is presented in the next paragraph.

Long Term Drift Compensation

The high confidence in the difference of the unified dataset A + B is 92%, which is caused by a systematically higher background and therefore higher positron rate per charge on collision shots. In order to unify datasets A and B, the long term drift of the background rate needs to be corrected. If it would be possible to determine the source of this higher rate, whether it is caused by a false charge or positron yield measurement, the corresponding quantity could be scaled accordingly, but this is not possible with the obtained data due to the limited number of experimental parameters that were measured on a single shot basis. One possible reason for the observed mean rate drift is a significantly and systematically changing LWFA spectrum, which is measured in advance of every dataset and a higher energy on dataset A was found compared to dataset B. This causes the higher predicted Breit-Wheeler rate in Table 4.3 and is the reason why sets A and B are evaluated separately. A solution to this would have been the γ-ray spectrometer additionally to the total γ-ray yield measured on the γ-ray profile diagnostic to normalise the data, but this measurement was too inaccurate to reconstruct the spectrum. The approach taken here is to calculate the rolling average over Breit-Wheeler data shots presented on Fig. 4.4, which shows the change in the background rate between the datasets. The average is calculated based on background

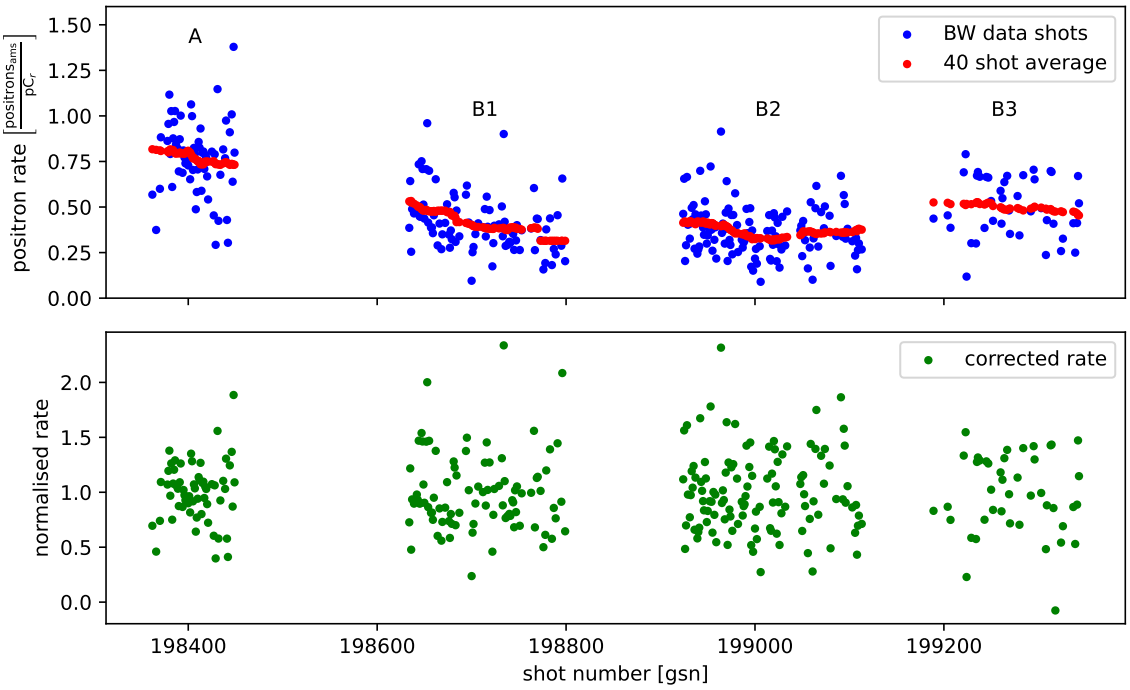

Figure 4.4.: A timeline over all Breit-Wheeler data shots. The average over 40 shots is calculated for each shot and shows the long term drift of the mean background rate. Each shot is corrected with this average to obtain the normalised rate, shown on the lower plot.

and collision shots, because all shots are background dominated. A potential signal on collision shots is further not affected by this because background and collision shots were taken in groups of 10 so that the 40 shot average always contains a similar amount of both shot types. Each shot is then normalised with its 40 shot average to obtain the normalised rate, which gives the relative difference to the 40 shot average. Since the normalised rate is not a measurement in positrons per charge any more, the charge based method of averaging can not be applied, leaving the method of averaging over shots as only option left. The results of the drift compensated datasets are presented in Table 4.8. The values show the relative difference to the rolling average and the error margins are standard errors of the mean. The overall properties are similar compared to the values before averaging, B2 shows the largest difference, B1 shows negative values and all sets have errors in the range of their absolute values. The important result in Table 4.8 is for the unified set A + B, which no longer shows an irregular high difference. On average, the measured AMS positron rate per reference charge is $(4.0 \pm 3.8)\%$ higher on collision shots compared to background shots.

Table 4.8.: Results of the drift compensated Breit-Wheeler datasets. The values show the relative difference to the 40 shot average.

dataset	background	collision	difference
A	0.973 ± 0.048	1.028 ± 0.047	0.055 ± 0.067
B1	1.007 ± 0.044	0.948 ± 0.066	-0.060 ± 0.079
B2	0.948 ± 0.051	1.039 ± 0.043	0.091 ± 0.066
B3	0.957 ± 0.076	1.008 ± 0.078	0.051 ± 0.109
B	0.978 ± 0.031	1.014 ± 0.033	0.036 ± 0.045
A + B	0.977 ± 0.026	1.018 ± 0.028	0.040 ± 0.038

Cross Check with Hot Background Shots

Despite the low confidence of all the measurements, a general tendency within the data towards an increased rate on collision shots is observed and needs to be explained. A potential origin for such an observation besides the Breit-Wheeler effect is a systematic error due to the x-ray driver beam, which is only fired on collision shots and has been investigated by taking hot background shots. Due to the increased experimental effort of taking hot background shots compared to cold background shots, only 30 good hot background shots are available for data evaluation. The shots cover a total charge of $474\,\mathrm{pC}_r$ and were taken equally distributed over datasets A, B1, B2 and B3. Due to the mentioned systematic drift of the background rate, a reasonable evaluation can only be done by averaging hot background shots the same way as cold shots with the long term average before calculating a difference. The result is an average increase of $(0.0 \pm 6.1)\%$ on collision shots compared to hot background shots. This remarkable similarity between hot background and collision shots is a strong argument for the hypothesis that the measured surplus on collision shots is caused by the x-ray driver beam. Potential mechanisms how the x-ray driver can induce a signal on SPD other than Breit-Wheeler pair production are scattered laser light, scattered x-rays or pairs from x-ray target debris that is hit by the γ-ray beam. Due to the shielding that should block laser and x-ray photons, the most likely cause for the increased signal on hot background and collision shots is x-ray target debris. It can potentially reach beyond the γ-ray shadow of the tungsten block and create pairs via the Bethe-Heitler or Trident process. The x-ray driver has a full width half maximum duration of 40 ps and is timed for peak overlap with the γ-ray beam, so half of the peak intensity is

Table 4.9.: Final results based on all data over the entire campaign. Shown is the measured relative difference of the AMS positron rate per reference charge on collision shots compared to cold and hot background shots.

compared shot types	measured relative difference
collision vs cold background	$(4.0 \pm 3.8)\%$
collision vs hot background	$(0.0 \pm 6.1)\%$

incident on the target 20 ps prior to the γ-ray pulse. The clearance between γ-ray beam and x-ray target is 1 mm, which can be surpassed by fast particles like electrons at velocities above 20% speed of light in 20 ps. The γ-ray beam does further not have a clear shadow due to its comparably large source size on the converter target of around 0.4 mm determined by the electron beam divergence. It is also possible that the x-ray target may move closer to γ-ray axis over multiple refresh cycles with target alignment by hand on every shot, increasing the likelihood of x-ray target particles reaching into the γ-ray beam path.

In the end, the uncertainty of the hot background measurement is very high and encloses the cold background measurement within error margins, so there is a significant chance that the similarity between collision and hot background shots is a statistical phenomenon within the obtained data. However, even if the measured increase on collision shots is a real signal, it is highly unlikely that it is due to the two-photon Breit-Wheeler process. The main reason for this is the low predicted pair rate around $1.7 \cdot 10^{-3}$ pairs per nC_r, which is 4 orders of magnitude below the achieved measurement accuracy of 22 pairs per nC_r within subset B2. To put this low predicted rate into perspective, all collision shots on this experiment have a combined total charge of 2.1 nC_r. This equates to a total probability of producing at least one Breit-Wheeler pair over all collision shots on this experiment of 3%. The probability to detect at least one pair is lowered by the AMS transport efficiency to 0.5%.

5. Conclusion

The work in hand presents an experimental campaign to test a setup capable of detecting the Breit-Wheeler process at the dual beam high power laser system Astra Gemini in England. The Breit-Wheeler process is the reaction of two photons to form an electron positron pair from quantum vacuum, essentially producing matter from nothing but light. This effect was first described by Breit and Wheeler [1] in 1934 but was never confirmed experimentally. The major aim of this campaign was to test a setup and develop methods and hardware to progress towards a successful validation of the Breit-Wheeler process in future experiments. The achieved performance and obtained results are summarised in the following section 5.1. Based on these, improvements for future experiments are discussed in section 5.2.

5.1. Summary of Results

Achieved Breit-Wheeler Pair Rate

A major result of the campaign is the overall demonstration and validation of the experimental setup. The Breit-Wheeler effect requires two high energy photon fields, which were produced and overlapped to enable the Breit-Wheeler process. The two colliding photon energies chosen for this experiment were 1-2 keV x-rays and 200-500 MeV γ-rays. The x-ray field was produced by heating a solid state germanium target with one of Geminis beams to generate M-L shell transmission radiation around 1-2 keV. The achieved x-ray yield per shot was up to $5.5 \cdot 10^{15}$ x-ray photons with a total energy of 1.25 J assuming an emission in 4π, which corresponds to a laser to x-ray energy conversion efficiency of up to 8%. More realistic models of the angular distribution suggest energy conversion efficiencies closer to 2%. The second photon field was produced by accelerating electrons via LWFA with Geminis second beam up to 700 MeV (typically 500 MeV) and subsequently generating bremsstrahlung in a solid state bismuth target. The multi 100 MeV γ-ray beam contained up to $9 \cdot 10^8$ photons above 10 MeV per nC LWFA beam charge. Since the γ-photon yield does not only depend on the electron beam charge but also on the energy, the average spectral shape

achieved on this experiment, shown on Fig. 4.1(a), is used as a reference, indicated by the usage of reference charge (nC_r). To calculate the expected Breit-Wheeler pair rate with the measured spatial, temporal and spectral properties of both photon fields, an algorithm was developed specifically for the collision geometry on this experiment. The experimentally achieved Breit-Wheeler pair rate was up to $1.5 \cdot 10^{-2}$ pairs per nC_r.

Analyser Magnet System

Detecting single Breit-Wheeler pairs at Astra Gemini is challenging due to the low amount of produced signal compared to background radiation. To improve the signal to noise ratio, a permanent magnet system was developed that guides produced pairs to shielded single particle detectors. The design of such a system is particularly challenging for Astra Gemini due to the spatial constrains in the laboratory, which prevents the installation of a sufficiently large radiation shield with the associated long beam paths. The solution developed for Gemini, called analyser magnet system (AMS), is composed of three permanent dipole magnets. These work in conjunction with caesium iodide scintillator based single particle detectors (SPD) and radiation shielding to measure single Breit-Wheeler pairs while suppressing background radiation. This system was tested for the first time and the principle of operation was validated. The trajectories of electrons through the AMS were verified by tracking the LWFA beam along the electron beam path with scintillation screens. The positron arm was verified by inserting a 1 mm thick PTFE target into the beam to produce a strong positron signal similar to Breit-Wheeler pairs, which was measured on the SPD. A critical performance parameter to characterise the AMS is the transport efficiency for Breit-Wheeler pairs, which was determined by calculating the trajectories of positrons over a range of phase space coordinates. The result was weighted with the simulated phase space distribution of created pairs considering the achieved x-ray and γ-ray properties. Averaged over all possible Breit-Wheeler pair source points, momenta and energies, the transport efficiency is 14%.

Single Particle Detectors

The Breit-Wheeler process is measured by detecting electrons and positrons from the collision of two photon fields. Because the cross section is low compared to technologically achievable photon densities at the energies required, an experiment will always have to measure single particles. For the photon fields produced at Gemini,

these have energies of a few 100 MeV. Such particles are not particularly difficult to detect in general with up to date technology, however the special challenge is to develop a system that fits into the constraints at Astra Gemini and can detect multi 100 MeV electrons and positrons with high confidence. The solution used on this experiment is a stack of caesium iodide scintillators coupled to a 4Picos ICCD from Stanford Computer Optics. This unit is called single particle detector (SPD) and can measure Breit-Wheeler class particles with practically 100% confidence as long as the background radiation level is sufficiently low. To quantify the amount of positrons on an image, two independent evaluation methods were developed. The first is based on a calibration of the integrated detector signal against Breit-Wheeler class particles. This was done by inserting a 1 mm thick PTFE calibration target into the beam to produce a defined amount of positrons on the SPD, which was directly correlated to the absolute integrated signal. The second method to quantify the positron yield on SPD is by searching for photon clusters that are produced by the cascades of high energy particles inside the scintillator crystals. Both methods complement each other depending on the yield on SPD and associated amount of background radiation. The calibration based method works well for strong signals where individual events cannot be distinguished whereas the photon cluster identification method gives more reliable results on low background shots.

Background and Signal-to-Noise Ratio

There are several requirements for a successful measurement of the Breit-Wheeler process. Firstly, the reaction needs to be enabled by providing the required photon fields in sufficient quantities to produce a measurable pair rate within the constrains of an experimental campaign. The achieved pair rate is $1.5 \cdot 10^{-2}$ pairs per nC_r, so on average a pair every 67 nC_r is expected to be produced. Combined with the 14% AMS transport efficiency to the SPD, a pair every 476 nC_r can be measured, which is very challenging but not generally impossible. The second essential parameter for a successful Breit-Wheeler measurement is the signal-to-noise ratio, which is determined by the measured background radiation and the predicted pair rate. The signal-to-noise ratio needs to be specified on two different levels that are based on the particles of which the background radiation is composed. Those are high energy particles that are similar to Breit-Wheeler pairs and low energy diffuse radiation. If the low energy diffuse radiation on SPD per shot is sufficiently low, high energy events can be identified with almost 100% reliability, what effectively results in a infinite signal-to-noise ratio for diffuse low energy background. If single events cannot be identified on a single shot

basis with high confidence, the diffuse low energy background adds to the total signal-to-noise ratio. The second type of background radiation is any particle that produces a signature similar to Breit-Wheeler pairs and is therefore measured as false positive. Such particles can for example be pairs that are created by the γ-ray beam colliding with beam line apertures and have similar properties to Breit-Wheeler pairs. This type of high energy particle background needs to be identified by comparing collision with background shots and looking for a systematic change of events per incident photon fields. The signal-to-noise ratio for this high energy particle background determines the required sample size that needs to be collected to make a statistically significant observation.

With the setup used at Gemini, high energy events could not be identified with high confidence due to the high diffuse background radiation level on average Breit-Wheeler shots, so that it adds together with high energy events to the total background against which the Breit-Wheeler signal needs to be measured. The ratio of high energy to low energy background was measured to be around unity by analysing a from AMS positrons shielded fraction of the SPD and comparing it with the region that was open for AMS positrons. The total background level on the SPD was equivalent to at least 277 AMS positrons per nC_r with typical values being around 400 AMS positrons per nC_r. Combined with the predicted Breit-Wheeler pair rate of $1.5 \cdot 10^{-2}$ pairs per nC_r and the 14% AMS transport efficiency, the effective signal-to-noise ratio on SPD was around $6 \cdot 10^{-6}$.

Test of the Overall Setup

To test the overall system with regards to the detection capability of an AMS positron signal on top of background radiation at a signal-to-noise ratio below unity, a 25 µm thick Kapton target was inserted into the beam to produce an AMS positron signal on SPD of up to $0.54^{+0.37}_{-0.24}\ \frac{\mathrm{positrons_{ams}}}{\mathrm{pC}_r}$. The Kapton produces Bethe-Heitler pairs when the γ-ray passes through it with similar properties compared to Breit-Wheeler pairs. By reducing the fraction of γ-ray beam covered by the Kapton target, the induced rate was controlled and corresponding signal-to-noise ratios were between 0.4 and 0.6. The measured signal on SPD showed an increase in AMS positrons per reference charge with up to 99% confidence when the Kapton target was inserted and the absolute value agreed with the predicted rate within error margins when evaluating the data with the calibration based method. The photon cluster identification method showed an increase of signal due to the Kapton target as well but was below the predicted value. This can be explained with the diffuse low energy background, which was too

intense to identify single high energy events reliably. This test measurement proves the detection capability of an AMS positron signal at signal-to-noise ratios below unity with the overall experimental setup, hardware and software. Measuring the Breit-Wheeler process at a signal-to-noise ratio of $6 \cdot 10^{-6}$ is therefore only a matter of taking enough data to obtain a statistically significant result.

Measured Breit-Wheeler Data

The Breit-Wheeler effect is measurable as an AMS positron rate increase per incident photon quantity on collision shots compared to background shots. The obtained dataset with the full Breit-Wheeler setup comprises 312 good laser shots, of which 139 were collision and 173 were background shots. The effective charge, which is the amount of reference LWFA beam that produces γ-rays for the reaction, was $(2.1 \pm 0.2)\,\mathrm{nC}_r$ on collision and $(2.6 \pm 0.2)\,\mathrm{nC}_r$ on background shots. The positron yield was evaluated with both the calibration and photon cluster identification method, however the cluster identification did not work with high confidence and gave less significant results. Due to changes in the background rate between different subsets and shot days, the absolute AMS positron rate was only obtained for specific subsets. The most significant increase during collision shots was measured to be $(40 \pm 22)\,\frac{\mathrm{positrons_{ams}}}{\mathrm{nC}_r}$ with a confidence of 63%. After correcting for long term drift effects and unifying all recorded data into one set, the average increase of the AMS positron rate per reference charge on collision shots compared to background was found to be $(4.0 \pm 3.8)\%$.

The background shots were so called cold background shots where the x-ray driver beam was not fired. To test if any effect caused by the x-ray driver beam would induce a false signal on collision shots, a small number of hot background shots were taken, where both laser beams fired but the timing between both beams was changed, so that the Breit-Wheeler effect would be strongly suppressed. On average, the relative difference between collision and hot background shots was $(0.0 \pm 6.1)\%$. This leads to the assumption that the measured signal increase on collision shots, if it is not a random statistical effect, is likely caused by the x-ray driver beam. A potential explanation for this is debris from the x-ray target that is scattered into the γ-ray beam path. It is highly unlikely that the measured signal is due to the two-photon Breit-Wheeler process since the predicted pair rate is 4 orders of magnitude below the achieved measurement accuracy. Based on the total charge on all collision shots, the total probability to measure at least one Breit-Wheeler pair over the entire experimental campaign was 0.5%.

5.2. Improvements for Future Experiments

Optimise LWFA Performance

The experiment at Astra Gemini was indented to be performed with optimal LWFA performance, which is far better than what has been achieved on this campaign. The main reason for this is the required change of the F/40 focal spot position, which could due to spatial constrains only be achieved by inserting a set of turning mirrors between the focussing optic and the focal spot. This limited the pule energy to around 8 J, which compared to the nominal 15 J resulted in a much worse LWFA performance. With optimal laser settings as described in [52], LWFA electron beams with energies up to 2.5 GeV and 374 pC above 200 MeV can be produced. This has two major effects on a Breit-Wheeler measurement, a higher pair rate per charge and a higher amount of charge per shot. The higher pair rate per charge, which can be up to 0.2 $\frac{\text{positrons}_{\text{ams}}}{\text{nC}_r}$ at source with the beam from [52], increases the signal-to-noise ratio from $6 \cdot 10^{-6}$ to around 10^{-4} assuming that the background is still proportional to LWFA charge and is not affected by the higher photon energy. This lowers the total amount of pairs that need to be produced for a statistical significant observation. For example requires 68% confidence or $1\,\sigma$ of a normal distribution $4 \cdot 10^4$ pairs with the beam from [52] instead of $4 \cdot 10^5$ with the achieved beam. Based on the pair rate, the required amount of reference charge to produce these pairs decreases from $2.7 \cdot 10^7\,\text{nC}_\text{r}$ to $2 \cdot 10^5\,\text{nC}_\text{r}$. Due to the higher charge per shot with the beam from [52], the required number of shots decreases even further, from $1.4 \cdot 10^9$ to $1.0 \cdot 10^6$ shots. At the repetition rate of Gemini, which is one shot every 20 seconds, and assuming the LWFA beam from [52] on every shot, the measurement would take 231 days instead of almost 1000 years. For a significance of 99.994% or $4\,\sigma$, these durations are 10 years for the beam from [52] and 10^5 years for the achieved performance.

Better Background Shielding

The best way to increase the signal-to-noise ratio and thereby decrease the overall requirements to reach a certain statistical significance is by lowering the background on detector. A 10 times lower background would increase the signal-to-nose ratio by a factor 10 and lower the required number of pairs by a factor 10. Assuming the pair rate and LWFA charge per shot are unchanged, 10 times less shots are required for the same statistical significance. In the theoretical limit of no measurable background, which would be an infinite signal-to-noise ratio, the experimental time is defined by the time until the first Breit-Wheeler pair is detected. For the achieved electron beam

this is every $2.4 \cdot 10^5$ shots and for the beam from [52] every 200 shots.

Energy Conversion Efficiency Limited Consideration

The knowledge gained from the Gemini campaign allows an estimate of the requirements for a successful follow up experiment in the future. The essential parameter is the signal-to-noise ratio, because it determines the amount of data that needs to be taken. The rate at which data can be recorded determines the overall experimental time and in the limit of no measurable background, the time until the first pair is produced is essential. The probably most straight forward method to increase the number of pairs per shot is more laser energy. State of the art laser systems at CALA in Munich or BELLA in Berkeley feature a repetition rate of 1 Hz and pule energies of several 10 J. The energy conversion efficiency from laser to electron beam can reach values between 2% to 3% as demonstrated at Gemini [52], which in principle enables electron beams with 50 pC at 500 MeV per joule pulse energy on target. The x-ray generation reaches similar efficiencies of a few percent as measured on this experiment, which allows around 10^{14} photons at 1.5 keV per joule pulse energy on target. With the bremsstrahlung target and overlap geometry on this experiment, approximately $2 \cdot 10^{-5}$ pairs per joule in each pulse on target can be produced. For Gemini with energies around two times 10 joule on target this means $2 \cdot 10^{-3}$ pairs per shot or one pair every 500 shots. This upper, energy conversion efficiency limited estimate is similar for CALA, BELLA and comparable systems in the multi 10 J class. A higher pair yield can be achieved with more energy, especially in the x-ray driver, because this increases the pair yield but not the background on single particle detectors. Another laser system at the CLF located right next to Gemini is Vulcan, who delivers several 100 J on target [80]. A hypothetical combined Gemini Vulcan setup, assuming 10 J and 500 J pulse energies, can potentially generate pair rates of 0.1 per shot or one every 10 shots if Vulcan generates x-rays and Gemini accelerates electrons. Pumping even more energy into the x-ray field requires a target geometry change to increase the laser heated surface area, for example a cylinder, called hohlraum. Such a setup was proposed by Pike [8] and requires laser energies in the megajoule [29] range. He calculated rates between 100 and 10.000 pairs per shot depending on the heating efficiency of the hohlraum. The algorithm developed for the collision geometry at Gemini with the LWFA beam from [52] and scaling the x-ray yield to one megajoule of incident laser energy predicts around 200 pairs per shot with 10 J and 1 MJ pulse energies. This energy conversion efficiency limited consideration for different classes of lasers shows that more energy can lead to measurable pair rates at existing facilities.

To do this on multi 10 J systems, additional optimisation of the collision geometry is needed.

Optimising the Collision Geometry

With the Gemini setup, an energy conversion efficiency limited rate of one pair every 500 shots can be achieved with 10 J in each beam. In order to enable a Breit-Wheeler process measurement on multi 10 J systems like Astra Gemini or at CALA, the pair yield needs to be increased without changing laser energy and by extent total numbers of photons. The only way to do so is by confining the produced photons into a smaller interaction volume to increase the spatial photon density. In case of the γ-ray beam the duration is a few femtoseconds, which cannot be reduced further, but the radius is 1.8 mm (Gaussian standard deviation) and has optimisation potential. It can be decreased by reducing the distance between Breit-Wheeler interaction region and LWFA source point, because the electron and by extension γ-ray beam size is defined by the divergence and therefore drift length. The distance from LWFA source point to Breit-Wheeler interaction point at Gemini is 1500 mm to accommodate the LWFA target, laser beam block, converter target stage, collimator, tungsten block, spectrometer magnet and drift space in between. Those components can be compacted to a large degree, for example can the tungsten block and collimator be unified into a single D-shaped collimator. The converter target can be attached to the front surface of this new collimator. The magnet needs to deviate charged particles away from the interaction region, for which it needs an integrated field strength around 0.3 Tm. The solution at Gemini was a 400 mm long and around 1 T strong permanent dipole magnet. This can be replaced with a more compact design utilising iron pole shoes to increase the field strength to 2 T over 150 mm. A gap of 5 mm would be sufficient, which can be filled with the D-shaped collimator. This unit that unifies magnet, collimator, tungsten block and converter would be 150 mm long. Together with some space for LWFA target exit, laser beam block and drift space towards the interaction region, the distance from LWFA source to Breit-Wheeler interaction region can be decreased from 1500 mm to 200 mm. This allows a significant reduction of γ-ray beam size from 1.8 mm to 0.3 mm, potentially even further to 0.1 mm depending on converter target thickness and electron beam properties like energy and divergence. Even a moderate reduction to 0.5 mm increases the pair yield by a factor 3 because a larger fraction of γ-rays is closer to the x-ray source and therefore in regions with high spatial x-ray density. If the distance of the x-ray target to the γ-ray axis can be controlled more precisely and scattered debris is not an issue, the x-ray target can potentially be moved

closer to the axis to increase the x-ray density, which in case of a reduction from 1 mm to 0.5 mm would double the pair yield. The combination of a reduced γ-ray beam size to 0.5 mm (Gauss standard deviation) and x-ray source distance of 0.5 mm increases the pair yield by a factor 6, so that on average one pair is expected around every 100 shots.

Final Thoughts

The experiment at Astra Gemini demonstrated a possible setup to measure the Breit-Wheeler process. The achieved performance was $1.5 \cdot 10^{-2}$ pairs per nC_r or one pair every $2.4 \cdot 10^5$ laser shots. The detection system composed of analyser magnet system and single particle detectors was tested successfully and a signal-to-noise ratio of $6 \cdot 10^{-6}$ was achieved. A statistical measurement with 99.994% (4σ) confidence would need 10^{11} laser shots taken over 10^5 years.

The LWFA performance on this experiment was low due to limited laser energy. By improving the LWFA performance, the required number of laser shots can be decreased significantly. This is ultimately limited by the energy conversion efficiency from laser light into Breit-Wheeler capable photon fields, which entails a maximum pair rate around $2 \cdot 10^{-5}$ per joule in each laser beam. By optimising the collision geometry, the pair yield can be increased further by a factor 6. At Gemini or other comparable multi 10 J systems, an experimental setup like the presented one with energy conversion efficiency limited performance and optimised collision geometry will require many 10 to a few 100 laser shots to produce a single pair. A statistical measurement with a signal-to-noise ratio of 1 therefore requires 100's to 1000's of laser shots to achieve a statistical significance of 99.994% or 4σ. When pairing a kilojoule class x-ray driver with a Gemini class LWFA source and being conversion efficiency limited as well as using the optimised geometry, pair rates around one every 2 shots can be achieved. This requires 200 shots at a signal-to-noise ratio of 1 and over 1000 shots with a SNR of 0.1 to achieve 99.994% (4σ) confidence. The most energetic laser system available worldwide, the NIF laser array, paired with a state-of-the-art LWFA source can achieve pair rates between 100 and 10.000 [8] per shot. This would allow a measurement with 99.994% (4σ) confidence within a single background and collision shot for signal-to-noise ratios above 0.1 whereas SNRs around 0.01 would require multiple shots.

In the end, the achievable Breit-Wheeler pair rate with the combination of multi 100 MeV γ-rays from LWFA electron bremsstrahlung and 1-2 keV x-rays from germanium M-L shell transition radiation is too low due to the poor energy conversion

efficiency and the intrinsic spatial and temporal extent of the photon fields to perform a statistically significant measurement at Gemini class laser facilities. To make this possible, optimum LWFA and x-ray performance as well as the refined overlap geometry are mandatory while suppressing the background to reach a signal-to-noise ratio of not less than unity. In this case, a measurement with 99.994% (4σ) confidence can be done within several 1000 good laser shots. The spatial density of γ-rays scales with the inverse square of the distance from electron source to interaction point, resulting in a 13 times higher value for the realistic reduction from 1.8 mm to 0.5 mm. Considering the macroscopic x-ray field, most of the γ-ray density increase is wasted. This potential can be used more efficiently by confining the x-rays too, for example by using an FEL or by colliding γ-rays with a focussed laser beam in the first place to measure non-linear Breit-Wheeler pair production [7].

In their publication from 1934 [1], Breit and Wheeler wrote that an experimental observation of the Breit-Wheeler process is „ hopeless “ due to the unavailability of intense photon fields with the required energies. Within the almost 100 years since they made that statement, staggering progress in experimental physics, particle accelerators and high-power lasers made the production of the required photon fields possible, but the unification into one experimental setup to perform a statistically significant measurement remains a task for next generation FEL and laser facilities with many 10 J to 100 J pulse energies. Those experiments are being planned already [81, 48, 82, 83].

Bibliography

[1] G. Breit and J. A. Wheeler, "Collision of two light quanta," *Phys. Rev.*, vol. 46, pp. 1087–1091, Dec 1934.

[2] D. L. Burke, R. C. Field, G. Horton-Smith, J. E. Spencer, D. Walz, S. C. Berridge, W. M. Bugg, K. Shmakov, A. W. Weidemann, C. Bula, K. T. McDonald, E. J. Prebys, C. Bamber, S. J. Boege, T. Koffas, T. Kotseroglou, A. C. Melissinos, D. D. Meyerhofer, D. A. Reis, and W. Ragg, "Positron production in multiphoton light-by-light scattering," *Phys. Rev. Lett.*, vol. 79, pp. 1626–1629, Sep 1997.

[3] S. P. Mangles, C. Murphy, Z. Najmudin, A. G. R. Thomas, J. Collier, A. E. Dangor, E. Divall, P. Foster, J. Gallacher, C. Hooker, *et al.*, "Monoenergetic beams of relativistic electrons from intense laser–plasma interactions," *Nature*, vol. 431, no. 7008, pp. 535–538, 2004.

[4] J. Faure, Y. Glinec, A. Pukhov, S. Kiselev, S. Gordienko, E. Lefebvre, J.-P. Rousseau, F. Burgy, and V. Malka, "A laser–plasma accelerator producing monoenergetic electron beams," *Nature*, vol. 431, no. 7008, pp. 541–544, 2004.

[5] C. Geddes, C. Toth, J. Van Tilborg, E. Esarey, C. Schroeder, D. Bruhwiler, C. Nieter, J. Cary, and W. Leemans, "High-quality electron beams from a laser wakefield accelerator using plasma-channel guiding," *Nature*, vol. 431, no. 7008, pp. 538–541, 2004.

[6] A. J. Gonsalves, K. Nakamura, J. Daniels, C. Benedetti, C. Pieronek, T. C. H. de Raadt, S. Steinke, J. H. Bin, S. S. Bulanov, J. van Tilborg, C. G. R. Geddes, C. B. Schroeder, C. Tóth, E. Esarey, K. Swanson, L. Fan-Chiang, G. Bagdasarov, N. Bobrova, V. Gasilov, G. Korn, P. Sasorov, and W. P. Leemans, "Petawatt laser guiding and electron beam acceleration to 8 gev in a laser-heated capillary discharge waveguide," *Phys. Rev. Lett.*, vol. 122, p. 084801, Feb 2019.

[7] C. Keitel, A. D. Piazza, G. Paulus, T. Stoehlker, E. Clark, S. Mangles, Z. Najmudin, K. Krushelnick, J. Schreiber, M. Borghesi, B. Dromey, M. Geissler,

D. Riley, G. Sarri, and M. Zepf, "Photo-induced pair production and strong field qed on gemini," 2021.

[8] O. J. Pike, F. Mackenroth, E. G. Hill, and S. J. Rose, "A photon-photon collider in a vacuum hohlraum," *Nature Photonics*, vol. 8, pp. 434–436, June 2014.

[9] H. Hu, C. Müller, and C. H. Keitel, "Complete qed theory of multiphoton trident pair production in strong laser fields," *Phys. Rev. Lett.*, vol. 105, p. 080401, Aug 2010.

[10] I. Newton, Sir, "Philosophiæ naturalis principia mathematica," *Jussu Societatis Regiæ ac Typis Josephi Streater*, 1687.

[11] J. C. Maxwell, "On physical lines of force," *Philosophical Magazine*, vol. 90, pp. 11–23, Feb. 2010.

[12] H. Hertz, "Ueber einen einfluss des ultravioletten lichtes auf die electrische entladung," *Annalen der Physik*, vol. 267, no. 8, pp. 983–1000, 1887.

[13] H. Hertz, "Ueber sehr schnelle electrische schwingungen," *Annalen der Physik*, vol. 267, no. 7, pp. 421–448, 1887.

[14] J. J. Thomson, "Discovery of the electron," *Philosophical Magazine*, vol. 44, p. 93, 1897.

[15] P. Lenard, "Ueber die lichtelektrische wirkung," *Annalen der Physik*, vol. 313, no. 5, pp. 149–198, 1902.

[16] A. Einstein, "Über einen die Erzeugung und Verwandlung des Lichtes betreffenden heuristischen Gesichtspunkt," *Annalen der Physik*, vol. 322, pp. 132–148, Jan. 1905.

[17] M. Planck, "Ueber das gesetz der energieverteilung im normalspectrum," *Annalen der Physik*, vol. 309, no. 3, pp. 553–563, 1901.

[18] P. A. M. Dirac, "The Quantum Theory of the Electron," *Proceedings of the Royal Society of London Series A*, vol. 117, pp. 610–624, Feb. 1928.

[19] P. A. M. Dirac, "A Theory of Electrons and Protons," *Proceedings of the Royal Society of London Series A*, vol. 126, pp. 360–365, Jan. 1930.

[20] W. Pauli, "Über den zusammenhang des abschlusses der elektronengruppen im atom mit der komplexstruktur der spektren," *Zeitschrift für Physik*, vol. 31, no. 1, pp. 765–783, 1925.

[21] P. A. M. Dirac, "Quantised singularities in the electromagnetic field," *Proceedings of the Royal Society of London Series A*, vol. 133, pp. 60–72, Sept. 1931.

[22] C. D. Anderson, "The positive electron," *Phys. Rev.*, vol. 43, pp. 491–494, Mar 1933.

[23] W. H. H. Bethe, "On the stopping of fast particles and on the creation of positive electrons," *Proc. R. Soc.*, vol. 146, pp. 83–112, Aug 1934.

[24] J. Cockcroft and E. Walton, "Experiments with high velocity positive ions," *Proceedings of the Royal Society of London Series A*, vol. 129, pp. 477–489, Nov. 1930.

[25] A. Grudiev, S. Calatroni, and W. Wuensch, "New local field quantity describing the high gradient limit of accelerating structures," *Phys. Rev. ST Accel. Beams*, vol. 12, p. 102001, Oct 2009.

[26] CERN, "The lep story." `https://home.cern/news/press-release/cern/lep-story`. Accessed: 04th Mar 2021.

[27] CERN, "The large hadron collider." `https://home.cern/science/accelerators/large-hadron-collider`. Accessed: 04th Mar 2021.

[28] W. P. Leemans, B. Nagler, A. J. Gonsalves, C. Tóth, K. Nakamura, C. G. Geddes, E. Esarey, C. Schroeder, and S. Hooker, "Gev electron beams from a centimetre-scale accelerator," *Nature physics*, vol. 2, no. 10, pp. 696–699, 2006.

[29] S. Glenzer, B. MacGowan, N. Meezan, P. Adams, J. Alfonso, E. Alger, Z. Alherz, L. Alvarez, S. Alvarez, P. Amick, *et al.*, "Demonstration of ignition radiation temperatures in indirect-drive inertial confinement fusion hohlraums," *Physical review letters*, vol. 106, no. 8, p. 085004, 2011.

[30] P. A. M. Dirac, "The quantum theory of the emission and absorption of radiation," *Proceedings of the Royal Society of London. Series A, Containing Papers of a Mathematical and Physical Character*, vol. 114, no. 767, pp. 243–265, 1927.

[31] E. Schrödinger, "An undulatory theory of the mechanics of atoms and molecules," *Phys. Rev.*, vol. 28, pp. 1049–1070, Dec 1926.

[32] J. J. Sakurai, *Advanced quantum mechanics*. Addison-Wesley Publishing Company, Inc., 1967.

[33] O. Klein, "Quantentheorie und fünfdimensionale relativitätstheorie," *Zeitschrift für Physik*, vol. 37, no. 12, pp. 895–906, 1926.

[34] W. Pauli, "Die allgemeinen prinzipien der wellenmechanik," in *Quantentheorie*, pp. 83–272, Springer, 1933.

[35] W. Heisenberg, "Über den anschaulichen Inhalt der quantentheoretischen Kinematik und Mechanik," *Zeitschrift fur Physik*, vol. 43, pp. 172–198, Mar. 1927.

[36] F. Sauter, "Über das verhalten eines elektrons im homogenen elektrischen feld nach der relativistischen theorie diracs," *Zeitschrift für Physik*, vol. 69, no. 11, pp. 742–764, 1931.

[37] J. Schwinger, "On gauge invariance and vacuum polarization," *Physical Review*, vol. 82, no. 5, p. 664, 1951.

[38] H. Bethe and W. Heitler, "On the stopping of fast particles and on the creation of positive electrons," *Proceedings of the Royal Society of London Series A*, vol. 146, pp. 83–112, Aug. 1934.

[39] D. Seipt, *Strong-Field QED Processes in Short Laser Pulses*. PhD thesis, Technische Universität Dresden, 2012.

[40] A. Blinne, *Electron Positron Pair Production in Strong Electric Fields*. PhD thesis, Friedrich-Schiller-Universität Jena, 2016.

[41] V. Ritus, "Quantum effects of the interaction of elementary particles with an intense electromagnetic field," *J. Sov. Laser Res.;(United States)*, vol. 6, no. 5, 1985.

[42] A. Nikishov, "Problems of intense external-field intensity in quantum electrodynamics," *Journal of Soviet Laser Research*, vol. 6, no. 6, pp. 619–717, 1985.

[43] K. Poder, M. Tamburini, G. Sarri, A. Di Piazza, S. Kuschel, C. Baird, K. Behm, S. Bohlen, J. Cole, D. Corvan, *et al.*, "Experimental signatures of the quantum nature of radiation reaction in the field of an ultraintense laser," *Physical Review X*, vol. 8, no. 3, p. 031004, 2018.

[44] J. Cole, K. Behm, E. Gerstmayr, T. Blackburn, J. Wood, C. Baird, M. J. Duff, C. Harvey, A. Ilderton, A. Joglekar, *et al.*, "Experimental evidence of radiation reaction in the collision of a high-intensity laser pulse with a laser-wakefield accelerated electron beam," *Physical Review X*, vol. 8, no. 1, p. 011020, 2018.

[45] A. Nikishov, "Absorption of high energy photons in the universe," *Zhur. Eksptl'. i Teoret. Fiz.*, vol. 41, 1961.

[46] R. J. Gould and G. P. Schréder, "Pair production in photon-photon collisions," *Phys. Rev.*, vol. 155, pp. 1404–1407, Mar 1967.

[47] X. Ribeyre, E. d'Humières, O. Jansen, S. Jequier, V. Tikhonchuk, and M. Lobet, "Pair creation in collision of γ-ray beams produced with high-intensity lasers," *Physical Review E*, vol. 93, no. 1, p. 013201, 2016.

[48] A. Golub, S. Villalba-Chávez, H. Ruhl, and C. Müller, "Linear breit-wheeler pair production by high-energy bremsstrahlung photons colliding with an intense x-ray laser pulse," *Physical Review D*, vol. 103, no. 1, p. 016009, 2021.

[49] Python Software Foundation, "Python." `https://www.python.org/`. Accessed: 11th June 2021.

[50] R. J. Rossi, *Mathematical Statistics: An Introduction to Likelihood Based Inference*. John Wiley & Sons, 2018.

[51] H. H. Ku *et al.*, "Notes on the use of propagation of error formulas," *Journal of Research of the National Bureau of Standards*, vol. 70, no. 4, pp. 263–273, 1966.

[52] K. Poder, *Characterisation of self–guided laser wakefield accelerators to multi-GeV energies*. PhD thesis, Imperial College London, Sep 2018.

[53] J. Peacock, A. Taylor, and A. Lawrence, "Astronomical statistics," 2003.

[54] P. Saha, "Principles of data analysis," 2003.

[55] W. Feller, *An introduction to probability theory and its applications, vol 2*. John Wiley & Sons, 2008.

[56] F. Garwood, "Fiducial limits for the poisson distribution," *Biometrika*, vol. 28, no. 3/4, pp. 437–442, 1936.

[57] N. Johnson, A. Kemp, and S. Kotz, *Univariate Discrete Distributions, Chapter 4: Poisson Distribution*, pp. 156–207. John Wiley & Sons, 2005.

[58] SciPy developers, "Scipy." `https://www.scipy.org/about.html`. Accessed: 11th June 2021.

[59] B. Kettle, D. Hollatz, E. Gerstmayr, G. M. Samarin, A. Alejo, S. Astbury, C. Baird, S. Bohlen, M. Campbell, C. Colgan, D. Dannheim, C. Gregory, H. Harsh, P. Hatfield, J. Hinojosa, Y. Katzir, J. Morton, C. D. Murphy, A. Nurnberg, J. Osterhoff, G. Pérez-Callejo, K. Poder, P. P. Rajeev, C. Roedel, F. Roeder, F. C. Salgado, G. Sarri, A. Seidel, S. Spannagel, C. Spindloe, S. Steinke, M. J. V. Streeter, A. G. R. Thomas, C. Underwood, R. Watt, M. Zepf, S. J. Rose, and S. P. D. Mangles, "A laser-plasma platform for photon-photon physics," 2021.

[60] R. Pattathil, "Laser system - gemini." `https://www.clf.stfc.ac.uk/Pages/Laser-system-Gemini.aspx`. Accessed: 07th Dec 2020.

[61] C. Hooker, J. Collier, O. Chekhlov, R. Clarke, E. Divall, K. Ertel, B. Fell, P. Foster, S. Hancock, A. Langley, D. Neely, J. Smith, and B. Wyborn, "The astra gemini project - a dual-beam petawatt ti : Sapphire laser system," *Journal de Physique IV (Proceedings)*, vol. 133, 06 2006.

[62] R. Pattathil, "Laser system - gemini front end." `https://www.clf.stfc.ac.uk/Pages/Laser-system-Astra.aspx`. Accessed: 07th Dec 2020.

[63] R. Pattathil, "Amplifier one." `https://www.clf.stfc.ac.uk/Pages/Amplifier-One.aspx`. Accessed: 07th Dec 2020.

[64] R. Pattathil, "Amplifier two." `https://www.clf.stfc.ac.uk/Pages/Amplifier-Two.aspx`. Accessed: 07th Dec 2020.

[65] R. Pattathil, "Amplifier three." `https://www.clf.stfc.ac.uk/Pages/Amplifier-Three.aspx`. Accessed: 07th Dec 2020.

[66] C. Hooker, S. Blake, O. Chekhlov, R. Clarke, J. Collier, E. Divall, K. Ertel, P. Foster, S. Hawkes, P. Holligan, B. Landowski, W. Lester, D. Neely, B. Parry, R. Pattathil, M. Streeter, and B. Wyborn, "Commissioning the astra gemini petawatt ti:sapphire laser system," pp. 1 – 2, 06 2008.

[67] R. Pattathil, "Gemini." `https://www.clf.stfc.ac.uk/Pages/The-Astra-Gemini-Facility.aspx`. Accessed: 07th Dec 2020.

[68] S. Kuschel, *Erzeugung dichter Elektronenpulse mit Laser-Plasma-Beschleunigern für QED Experimente in hohen Feldern*. PhD thesis, Friedrich-Schiller-Universität Jena, 2018.

[69] K. Behm, J. Cole, A. Joglekar, E. Gerstmayr, J. Wood, C. Baird, T. Blackburn, M. Duff, C. Harvey, A. Ilderton, *et al.*, "A spectrometer for ultrashort gamma-ray pulses with photon energies greater than 10 mev," *Review of Scientific Instruments*, vol. 89, no. 11, p. 113303, 2018.

[70] E. Gerstmayr, *Energetic Radiation from Wakefield Acceleration and its Applications*. PhD thesis, Imperial College London, 2020.

[71] D. Corvan, T. Dzelzainis, C. Hyland, G. Nersisyan, M. Yeung, M. Zepf, and G. Sarri, "Optical measurement of the temporal delay between two ultra-short and focussed laser pluses," *Optics express*, vol. 24, no. 3, pp. 3127–3136, 2016.

[72] P. Elleaume, O. Chubar, and J. Chavanne, "Computing 3d magnetic fields from insertion devices," in *Proceedings of the 1997 Particle Accelerator Conference (Cat. No. 97CH36167)*, vol. 3, pp. 3509–3511, IEEE, 1997.

[73] O. Chubar, P. Elleaume, and J. Chavanne, "A three-dimensional magnetostatics computer code for insertion devices," *Journal of synchrotron radiation*, vol. 5, no. 3, pp. 481–484, 1998.

[74] CERN, "Geant4." `https://geant4.web.cern.ch/`. Accessed: 10th May 2021.

[75] S. Agostinelli, J. Allison, K. a. Amako, J. Apostolakis, H. Araujo, P. Arce, M. Asai, D. Axen, S. Banerjee, G. Barrand, *et al.*, "Geant4—a simulation toolkit," *Nuclear instruments and methods in physics research section A: Accelerators, Spectrometers, Detectors and Associated Equipment*, vol. 506, no. 3, pp. 250–303, 2003.

[76] J. Allison, K. Amako, J. Apostolakis, H. Araujo, P. A. Dubois, M. Asai, G. Barrand, R. Capra, S. Chauvie, R. Chytracek, *et al.*, "Geant4 developments and applications," *IEEE Transactions on nuclear science*, vol. 53, no. 1, pp. 270–278, 2006.

[77] J. Allison, K. Amako, J. Apostolakis, P. Arce, M. Asai, T. Aso, E. Bagli, A. Bagulya, S. Banerjee, G. Barrand, *et al.*, "Recent developments in geant4," *Nuclear Instruments and Methods in Physics Research Section A: Accelerators, Spectrometers, Detectors and Associated Equipment*, vol. 835, pp. 186–225, 2016.

[78] D. Raikov, "On the decomposition of poisson laws," in *Dokl. Akad. Nauk SSSR*, vol. 14, pp. 9–12, 1937.

[79] B. Efron and R. J. Tibshirani, "An introduction to the bootstrap," *Chapman & Hall*, vol. 436, 1993.

[80] CLF, "Vulcan." `https://www.clf.stfc.ac.uk/Pages/Vulcan-laser.aspx`. Accessed: 03rd June 2021.

[81] H. Abramowicz, M. Altarelli, R. Aßmann, T. Behnke, Y. Benhammou, O. Borysov, M. Borysova, R. Brinkmann, F. Burkart, K. Büßer, O. Davidi, W. Decking, N. Elkina, H. Harsh, A. Hartin, I. Hartl, B. Heinemann, T. Heinzl, N. TalHod, M. Hoffmann, A. Ilderton, B. King, A. Levy, J. List, A. R. Maier, E. Negodin, G. Perez, I. Pomerantz, A. Ringwald, C. Rödel, M. Saimpert, F. Salgado, G. Sarri, I. Savoray, T. Teter, M. Wing, and M. Zepf, "Letter of intent for the luxe experiment," 2019.

[82] F. Salgado, N. Cavanagh, M. Tamburini, D. Storey, R. Beyer, P. Bucksbaum, Z. Chen, A. Di Piazza, E. Gerstmayr, E. Isele, *et al.*, "Single particle detection system for strong-field qed experiments," *arXiv preprint arXiv:2107.03697*, 2021.

[83] F. C. Salgado, K. Grafenstein, A. Golub, A. Döpp, A. Eckey, D. Hollatz, C. Müller, A. Seidel, D. Seipt, S. Karsch, and M. Zepf, "Towards pair production in the non-perturbative regime," *submitted to New Journal of Physics, NJP-113829*, 2021.

A. Danksagung

Eine Dissertation bringt sich bekanntlich nicht allein zu Papier, was jeder Leser, der in seinem Leben bereits eine Abschlussarbeit angefertigt hat, sicherlich bestätigen kann. Sie enthält neben der wissenschaftlichen Tätigkeit auch unweigerlich eine persönliche Note des Verfassers, geprägt durch Erfahrungen während der Zeit als Doktorand. Für mich waren das neben Experimenten und Konferenzen vorrangig die Personen aus meinem privaten und beruflichen Umfeld, von denen viele zu Freunden geworden sind. Einige dieser Personen möchte ich hervorheben und für ihre Unterstützung danken.

Die Person, die mir die Promotion ermöglicht hat, ist mein Betreuer *Matt*. Er war auch der Betreuer meiner Masterarbeit und hat damit praktisch meine gesamte wissenschaftliche Laufbahn geleitet und in die richtigen Bahnen gelenkt, sodass ich nun tatsächlich eine Dissertation vorweisen kann.

Meine Kollegen, die zu Freunden geworden sind, haben mich in schwierigen Zeiten immer unterstützt. Besonders danke ich *Stephan* für die moralische Unterstützung in der Anfangszeit der Promotion. Für die schöne Zeit in D215 danke ich *Andreas*, *Alex* und *Stefan*. Ich werde mich immer an Welle:Erdball und die vielen Raketenstarts erinnern. Ich danke *Carola* für viele Abende bei Wein und schönen Gesprächen. *Peter*, *Daniel* und *Daniel*, vielen Dank für die Stammtische und Rippchen. *Felipe* and *Harsh* joined me on experiments at Gemini as well as Atomic Burger, thank you for the good times. Außerdem danke ich *Alex* für die Unterstützung in den letzten Monaten meiner Promotionszeit und freue mich auf die Zusammenarbeit am JETI.

A major experience during my PhD were the experiments at Gemini, over which I accumulated more than half a year in England. I would like to thank all the people I got to know at Gemini, especially *Guillermo*, who was very supportive during the experiments on both a scientific and personal level. I am also grateful for the numerous discussions of the results with *Brendan* and *Stuart*, thank you. I will never forget Gemini, the English breakfast and all the pints of cider at The Rose & Crown.

Ich möchte mich auch bei meinen Freunden und den Queregängern für viele schöne Abende bedanken. Besonders haben mich *Luise*, *Peter*, *Michel* und *Christian* unterstützt. Vielen Dank für viele Wanderungen, Lagerfeuer und Zockerabende.

B. Ehrenwörtliche Erklärung

Ich erkläre hiermit ehrenwörtlich, dass ich die vorliegende Arbeit selbständig, ohne unzulässige Hilfe Dritter und ohne Benutzung anderer als der angegebenen Hilfsmittel und Literatur angefertigt habe. Die aus anderen Quellen direkt oder indirekt übernommenen Daten und Konzepte sind unter Angabe der Quelle gekennzeichnet.

Weitere Personen waren an der inhaltlich-materiellen Erstellung der vorliegenden Arbeit nicht beteiligt. Insbesondere habe ich hierfür nicht die entgeltliche Hilfe von Vermittlungs- bzw. Beratungsdiensten (Promotionsberater oder andere Personen) in Anspruch genommen. Niemand hat von mir unmittelbar oder mittelbar geldwerte Leistungen für Arbeiten erhalten, die im Zusammenhang mit dem Inhalt der vorgelegten Dissertation stehen.

Die Arbeit wurde bisher weder im In- noch im Ausland in gleicher oder ähnlicher Form einer anderen Prüfungsbehörde vorgelegt.

Die geltende Promotionsordnung der Physikalisch-Astronomischen Fakultät ist mir bekannt.

Ich versichere ehrenwörtlich, dass ich nach bestem Wissen die reine Wahrheit gesagt und nichts verschwiegen habe.

Ort, Datum Dominik Hollatz